Data-driven projected WIMP sensitivity of XENONnT Experiment with neutron Veto

水越，彗太

(Degree)
博士（理学）

(Date of Degree)
2022-03-25

(Date of Publication)
2024-03-25

(Resource Type)
doctoral thesis

(Report Number)
甲第8286号

(URL)
https://hdl.handle.net/20.500.14094/D1008286

博士論文

Data-driven projected WIMP sensitivity of XENONnT Experiment with neutron Veto

中性子反同時計測検出器を含めた XENONnT 実験のデータを用いた WIMP 感度評価

令和 4 年 1 月

神戸大学大学院 理学研究科

水越彗太

Data-driven projected WIMP sensitivity of XENONnT Experiment with neutron Veto

KEITA MIZUKOSHI

PhD (Science)

Supervisor: Prof. Kentaro Miuchi
Co-referee: Prof. Hisaya Kurashige
Co-referee: Prof. Hideki Tou

A thesis submitted in fulfilment of
the requirements for the degree of
PhD (Science)

Department of Physics
Faculty of Science
Kobe University
Japan

12 January 2022

Abstract

Cosmology and observations of the universe strongly suggest the existence of dark matter, especially Weakly Interacting Massive Particle (WIMP), direct scattering has not yet been detected. One of the world-leading direct WIMP searches, the XENONnT experiment completed the commissioning and is almost ready to release its first science run results. The XENONnT detector is able to discriminate most of the electron recoil background events with light and charge signals. A neutron background is one of the most serious of the rest background sources. We introduced a new water Cherenkov detector to veto the neutrons as an upgrade from the XENON1T experiment. With the commissioning data, data-driven simulation is constructed. The simulation physics on the Geant4 framework is tuned up with an independent beam experiment. The optical behavior in the detector is calibrated with the optical calibrations as reflective material reflectivity including effects of water absorption and reflection at PMT surface. The unknown PMT collection efficiencies and other effects to drop the photons are also calibrated with source calibration. Finally, the simulation framework constructs waveforms with the format of the observed data, which is able to apply the real analysis chain. Appling a tagging algorithm, the neutron tagging efficiency is evaluated to 84.8% quantitatively while TPC livetime of 98.9%. In addition, systematic uncertainty for tagging efficiency is conservatively estimated.

With the simulation, we evaluated the amounts of the backgrounds and obtained WIMP sensitivity for the XENONnT experiment. The sensitivity of the XENONnT experiment to the Spin independent (dependent) WIMP, including the nVeto detector, is evaluated to be 1.4×10^{-48} cm^2 (2.2×10^{-43} cm^2 for neutron) for 50 GeV/c^2 mass at 90% confidence level. The XENONnT experiment with the new nVeto detector is ready to release its results.

Contents

CHAPTER 1

Introduction

The existence of dark matter has been suggested by observations of the universe, and it is thought to be an undiscovered particle. In particular, Weakly Interacting Massive Particles (WIMPs) are considered to be one of the promising candidates in the view of cosmology. The properties of this dark matter will be reviewed in Chapter 2.

In order to detect WIMPs, searches for WIMP-nucleus scattering events using large detectors have been carried out in underground laboratories all over the world. However, no agreement on the detection has been reached yet, and only upper limits of scattering cross sections have been reported. In the direct dark matter search experiments, the sensitivity is limited by their exposures and background event rates. Nowadays, the world-leading limits have been reported by the experiments with noble gas dual-phase Time Projection Chambers (TPCs). The TPC technique has been successfully enlarged the detector, thus large exposures were achieved. Moreover, the dual-phase TPC can detect both light and charge signals by using scintillation light and electroluminescence light for scattering events. Using these signals, we can distinguish between electron recoil events, which are considered to be derived from most background events, and nuclear recoil events, which are considered to be derived from WIMPs. In addition, since three-dimensional position reconstruction can be performed, external background events can be reduced by defining the fiducial volume using the self-shielding ability of xenon.

The XENON1T experiment is the world's leading experiment with a xenon dual-phase TPC, and we have set a limit for the cross section, $4.1 \times 10^{-47}\mathrm{cm}^2$ for 30 GeV/c^2 [1]. In the XENONnT experiment, which is the upgrade of the XENON1T experiment, the amount of xenon is increased by a factor of approximately five to further improve the sensitivity. The construction and detector commissioning of the XENONnT experiment have been completed, and we are preparing to report the first results. The overview of the XENONnT experiment is reviewed in Chapter 3.

Upgrades in the XENONnT experiment are not only the detector size but also additional outer water Cherenkov detector to veto neutron backgrounds, which cannot be discriminated with the TPC alone. An outer detector, called the nVeto detector, was installed to surround the TPC. Gadolinium, which has a high neutron capture cross section, is solved in the water at a mass ratio of 0.2%. Neutrons are captured by the hydrogen and gadolinium, and the emitted γ-ray-derived Cherenkov radiation is detected by 120 photomultiplier tubes (PMTs). The

use of a water Cherenkov detector with gadolinium to direct dark matter search experiments is a new technology that can be applied to further increase the size and sensitivity of future experiments. The nVeto detector is described in detail in Chapter 4.

In general, the Cherenkov detector detects Cherenkov rings and identifies particles. For example, in the Super-Kamiokande experiment, electrons and muons are identified by the shape of the detected ring. For the Cherenkov ring reconstruction, a high PMT coverage is essential. The Super-Kamiokande detector has a PMT coverage of about 40% [2]. On the other hand, for the neutron detection with the nVeto detector, the particle identification capability is not necessary and too many PMTs will be another background source. The PMT coverage is about 10% in the nVeto detector. The nVeto detector of the XENONnT experiment is covered with a reflective material, expanded PolyTetraFluoroEthylene (ePTFE) except for the PMT surface in order to keep photons as much as possible. This device has not been used in the past, and it is necessary to demonstrate the performance of the nVeto detector. Furthermore, the optical properties of the ePTFE in water, such as reflectivity, have not been evaluated. In this study, we designed, implemented, and operated optical devices to calibrate the optical properties of ePTFE. In particular, we proposed a system to measure the properties of the ePTFE by the time difference between the emission of laser light into the nVeto detector and the detection of photons. We designed and fabricated a water-resistant laser system and installed it in the nVeto detector. The system has been operated regularly and an analytical framework was constructed, and together with simulations, the evaluation of optical properties was realized in a data-driven method. This optical calibration system is described in Section 4.4.

We constructed a simulation that reproduces the real data including waveforms using the data during the detector commissioning. We developed an application based on the Geant4 framework. In the standard physical model of Geant4, the post-neutron capture decay of gadolinium is replaced by a model tuned by comparing the data with beam experiments. The optical model is well understood by the optical calibration described above. In addition, the unknown collection efficiency of the PMT was calibrated using an americium-beryllium source and matched with the data. The simulation reproduces the observed waveforms. The simulation details are described in Chapter 5.

In Chapter 6, we evaluate the number of background events and the neutron tagging efficiency of the nVeto detector using the simulation. The event selection conditions for the nVeto detector were determined to achieve high neutron tagging efficiency while keeping the TPC livetime as much as possible. The simulations are in the same format as the real data, and it means that the analysis method of the nVeto has been established in this study. The nVeto performance is shown in Section 6.1. The obtained neutron tagging efficiency was used to evaluate the sensitivity of the XENONnT experiment to search for the WIMP. The sensitiviety for spin-independent WIMPs is evaluated to be 1.4×10^{-48} cm^2 for 50 GeV/c^2 WIMPs at a 90% confidence level.

In this study, we focused on the tagging efficiency of the nVeto detector, but further tuning is expected to lead to the development of methods e.g., using machine learning. Further development items are discussed in Chapter 7. Finally, we conclude this work in Chapter 8.

CHAPTER 2

Dark matter

Dark matter is the undiscovered origin of gravity in the galaxy. The dark matter evidence and searches are reviewed in this chapter.

2.1 Existence of dark matter

The existence of dark matter is very strongly indicated by observations of the universe. Assuming the theory of relativity, the identity of dark matter is considered to be a particle with at least zero or small charge and sufficiently slow velocity (non-relativistic) to form the structure of the universe. This dark matter is called Cold Dark Matter (CDM), and the cosmological model called ΛCDM has been proposed as a benchmark, which states that the universe is filled with cold dark matter and further contributes to dark energy.

One of the strongest pieces of evidence for the existence of CDM has been obtained by observing the Cosmic Microwave Background (CMB). The CMB is an isotropic microwave background observed over the entire celestial sphere and is an observational fact that is regarded as evidence for the big bang theory. Figure 2.1 shows a heat map of the temperature fluctuations of the CMB observed by Plank [3]. If we assume that there is no other matter fluid, i.e., dark matter, when the CMB decoupling occurs, the anisotropy is predicted as follows

$$\frac{\delta\rho_b}{\rho_b} \sim 10^{-2}, \tag{2.1}$$

where ρ_b is a balyon density. However, this is inconsistent with the observed structure of the universe, 10^{-5}, which indicates the existence of a CDM detached from the heat bath before decoupling. As a quantitative analysis, a power spectrum with respect to the angle of fluctuation is obtained from the heat map (Figure 2.2). This power spectrum corresponds to the slight anisotropy present in the CMB. The ΛCDM cosmological model has 6 parameters, which explain the experimental data well. The densities of baryon and the dark matter, $\Omega_{\rm b}h^2$ and $\Omega_{\rm DM}h^2$ are fitted as

$$\Omega_{\rm b}h^2 = 0.0224 \pm 0.0001 \tag{2.2}$$

$$\Omega_{\rm DM}h^2 = 0.120 \pm 0.001. \tag{2.3}$$

It means that the universe contains about five times as much dark matter as normal baryons.

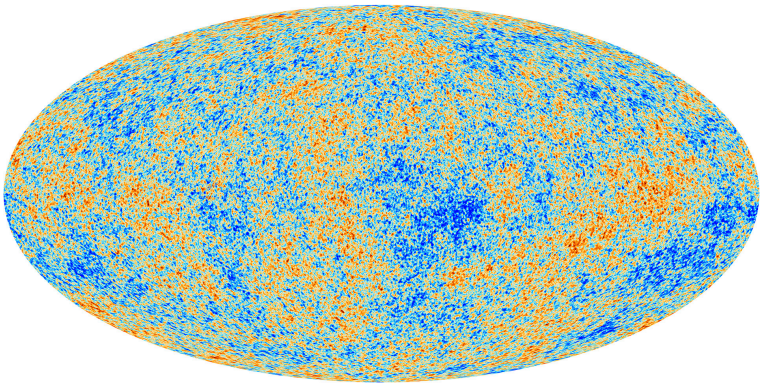

FIGURE 2.1. The anisotropies of the Cosmic microwave background (CMB) as observed by Planck [3]. Although globally isotropic, there is anisotropy on small scales, suggesting the existence of dark matter in the ΛCDM model.

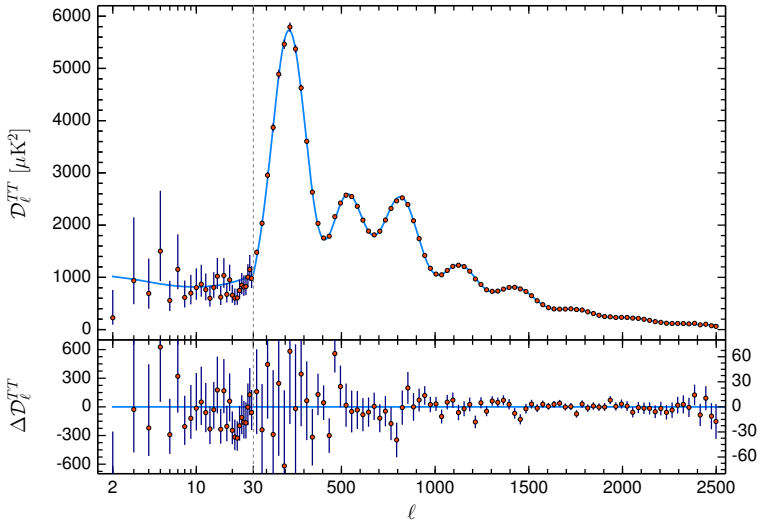

FIGURE 2.2. Planck foreground-subtracted temperature power spectrum (blue). The red plot shows the best fit with ΛCDM model [4].

On the other hand, the existence of dark matter has been observed on the scale of galaxies as well. Dark matter exists at various scales, from the Milky Way to smaller galaxies [5]. The most obvious example is a cluster 1E 0657-56 (or 1E 0657-558) called the bullet cluster as a visual evidence of the dark matter [6]. The bullet cluster is a collision of the two clusters. The cluster has been observed with gravity lensing effect and X-ray (Figure 2.3). Gravity lensing is a phenomenon in which light from a distant celestial object is bent by the distribution of gravitational potential between the object and the observer. This results in a visual distortion of the object. When the gravitational potential is not large, the images of multiple galaxies are not visible, and the distortions can be statistically confirmed, which is called weak gravity lensing. With the weak gravity lensing, the shape and the amount of the gravitational potential can be evaluated by statistically analyzing the distortions of the galaxies. In this example,

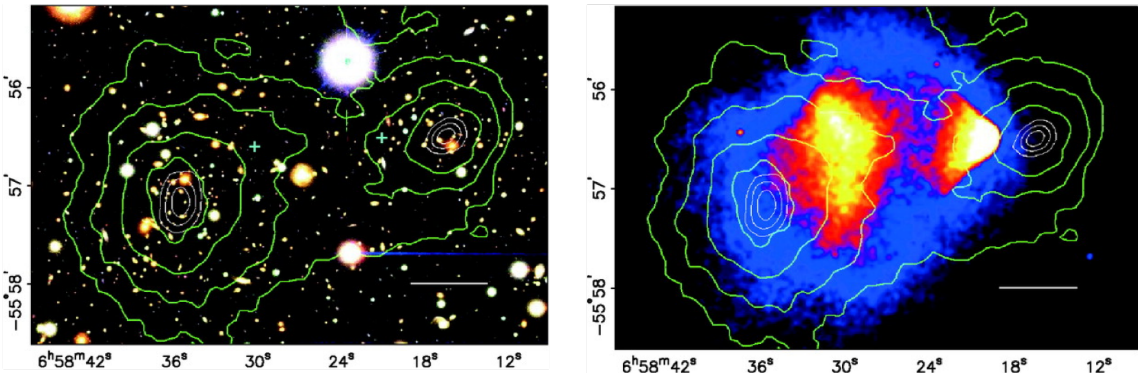

FIGURE 2.3. Color image from the Magellan images of the merging cluster 1E 0657-558 [6]. (Left) Mass distribution observed with gravity lensing. (Right) Hot gas distribution observed with X-ray.

after the collision of the two clusters, the hot gas is left behind near the center due to the interaction, while the gravitational source, which is thought to be dark matter, is moving away due to a smaller cross section.

The historical trigger of the discussion is an observation of the rotation curve of galaxies by Zvicky [7]. If the galaxy consists only of optically observable particles, the rotation velocity v would decrease in proportion to $\frac{1}{\sqrt{r}}$ where r is a distance to the center of the galaxy, according to Kepler's law since the objects observed to date are concentrated in the center of the galaxy. However, the observed rotation velocity is almost constant even in the outer regions of the galaxy where the number of objects is very small (Figure 2.4). This result implies that the mass distribution $M(r)$ in the galaxy is proportional to r. By the virial theorem, they evaluated the existence of an invisible mass 160 times larger than the optical mass.

Both large-scale cosmological probes and analyses of galaxy-scale mass structures suggest the existence of dark matter. The modified Newtonian dynamics (MOND) has been proposed as a position that does not assume dark matter [9]. However, MOND has not yet succeeded in explaining the observed results of the CMB or the bullet cluster [10].

2.2 Candidates of dark matter

From the observation of dark matter in the universe, dark matter is required to have zero or very small electric charge and to be very stable. If the dark matter particle has a charge, it will affect the baryon-photon-plasmas during decoupling period. Even if the coupling to the visible light field is suppressed for some reason, the charge can be at most on the mill-scale of the elementary charge, limited to $3.5 \times 10^{-7}(m_{\mathrm{DM}}/1\mathrm{GeV})^{0.58}$ and $4.0 \times 10^{-7}(m_{\mathrm{DM}}/1\mathrm{GeV})^{0.35}$ for DMs whose masses (m_{DM}) are less and more than 1 GeV, respectively [11].

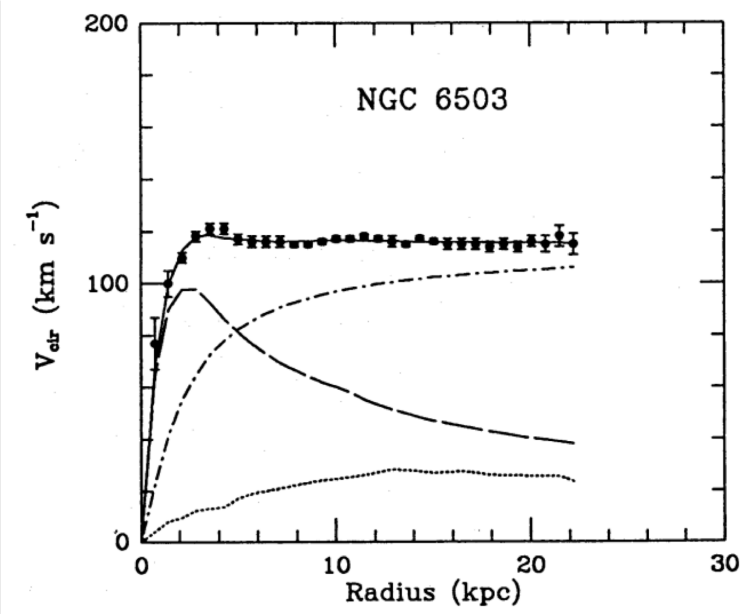

FIGURE 2.4. Rotational curve of the spiral galaxy NGC 6503. The dashed curves are for the visible components, the dotted curves for the gas, and the dash-dot curves for the dark halo [8].

The lower limit of mass is given by quantum effects. In the assumption of fermionic dark matter, $m_F > 70$ eV is given by the observed velocity dispersion and density of galaxies (Tremaine-Gunn limit) [12]. The upper mass limit is also limited by the structure in the dark matter halo and the stability of the galaxy [13]. The observations require the mass to be lighter than about $5M_\odot$ [14, 15]. This means that the mass of dark matter is almost unbounded without assuming a model.

The local density distribution of dark matter has been estimated from the vertical motion of massive tracer stars in the vicinity of the Sun. It has also been estimated by extrapolating the shape of the global galactic halo [16].

From the Gaia satellite observations, the local density distribution is given as (0.3–1.5) GeV/cm^3. This main uncertainty comes from the indefiniteness of the local baryon mass distribution. As the result of introducing the latest halo model, it is updated to (0.55 ± 0.17) GeV/cm^3 by Gaia. The measured value of the global extrapolation is (0.2 – 0.6) GeV/cm^3. For the results of the search experiment, 0.3 GeV/cm^3 is conventionally used for comparison with other experiments. The local velocity distribution of dark matter has been estimated by simulation. In the Standard Halo model (SHM), the density is inversely proportional to the square of r, and the velocity distribution is assumed to be the Maxwell-Boltzmann distribution.

We review dark matter production models and candidates in the following sections.

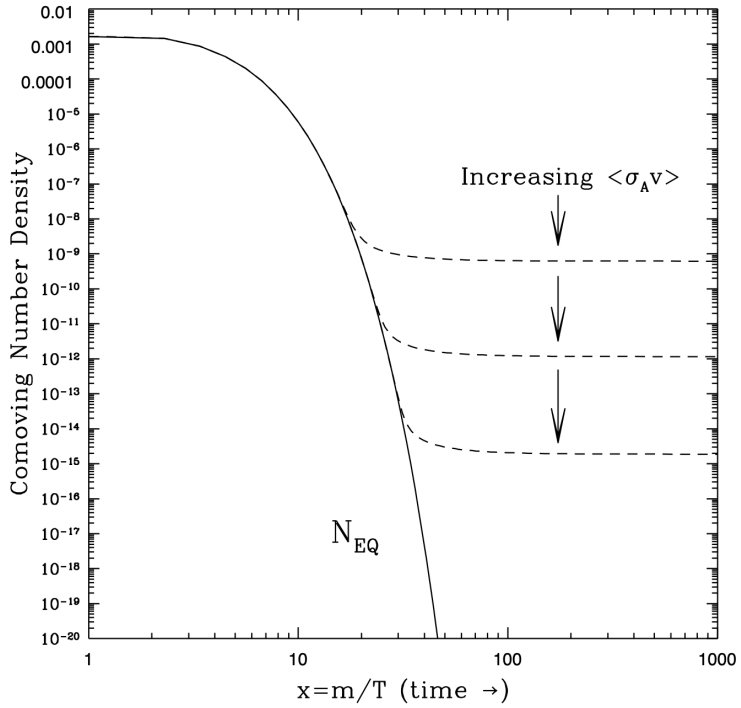

FIGURE 2.5. Schematic plot of dark matter density of a stable through the process of thermal freeze-out [17].

2.2.1 WIMP

Thermal production is considered to be the origin of dark matter production. The early universe is thought to have been hot and dense. In this model, dark matter is first produced thermally, then ceases to be produced as it cools, and remains with little interaction with other particles (Freeze-Out). This thermal relic abundance, Ωh^2, is approximated by the following equation,

$$\Omega h^2 \sim 0.1 \left(\frac{m_{\rm DM}/T}{20} \right) \left(\frac{10^{-8}\ {\rm GeV}^{-2}}{\sigma_{\rm DM+DM}} \right), \tag{2.4}$$

where T is a freeze-out (i.e. 'decoupling') temperature and $\sigma_{\rm DM+DM}$ is a dark matter-dark matter pair-annihilation cross section. The values of 0.1, 20, and 10^{-8} are arranged to simplify this discussion and they don't have special meanings on the physics contexts. Figure 2.5 illustrates the freeze-out. The freeze-out temperature is approximated with the given equation,

$$\sqrt{m_{\rm DM}/T} \cdot e^{-m_{\rm DM}/T} \sim (m_{\rm DM} \cdot M_p \cdot \sigma_{\rm DM+DM})^{-1}, \tag{2.5}$$

where M_p is a reduced planck mass, $\sim 2.435 \times 10^{18}$ GeV. Here, assuming WIMPs, $m_{\rm DM}/T$ is apporoximetly 10-50 and $\sigma_{\rm DM+DM}$ is $\sim 10^{-8}$ GeV^{-2}. It is consistent with the current observation. This simple mechanism is known as the 'WIMP miracle'.

WIMPs are also motivated as supersymmetric particles derived from supersymmetry theory for the Higgs hierarchy problem. Supersymmetry theory predicts the existence of supersymmetric particles that differ from the Standard Model particles by half a spin and have equal charge.

The WIMP is one of the most attractive candidates for dark matter because it is naturally derived from thermal production and is included in the framework for solving unsolved physical problems. In this work, we focus on the WIMP search.

2.2.2 Other candidates

There are other important dark matter candidates, axion, and Primordial Black Hole (PBH).

Axion is a particle introduced to solve a strong CP (Charge-Parity) problem [18]. The strong CP problem is the unnaturalness of CP symmetry in strong interactions. There are two-phase parameters in the Standard Model that break the CP symmetry. One is the phase of quantum chromodynamics, $\bar{\theta}$, and the other is the phase of the CKM matrix, $\theta_{\rm EM}$. The effective Lagrangian $\mathcal{L}_{\rm eff}$ of QCD is described as follows,

$$\mathcal{L}_{\rm eff} = \mathcal{L} + \frac{\bar{\theta} + \theta_{\rm EM}}{16\pi^2} g_s^2 {\rm Tr}[G_{\mu\nu}\tilde{G}_{\mu\nu}]. \tag{2.6}$$

The second term breaks the CP symmetry, but experiments on electric dipole moments do not confirm that the CP is broken, and a strong limit of $|\bar{\theta} + \theta_{\rm EM}| < 10^{-9}$ is given. There is no reason why this $|\bar{\theta} + \theta_{\rm EM}|$ should be much small.

As a solution to this problem, global U(1) symmetry called PQ symmetry is added to the SU(3)×SU(2)×U(1) symmetry of the Standard Model. The particle produced by the breaking of this PQ symmetry along with the weak symmetry is the axion.

This axion is a possible candidate for dark matter. However, the original axion for the strong CP problem has been rejected, and nowadays the search for the axion-like particles (ALPS) is being conducted only for the solution of the dark matter problem. The axion oscillates coherently, but its contribution can be neglected because it oscillates very fast with respect to the age of the universe. In other words, axion behaves as a dark matter on the cosmological scale. The mass of the axion is limited to μeV/c^2 to eV/c^2 by observations of supernova neutrinos and cosmology. Axions have been widely searched for by detecting photons produced by the Primakov effect, in which axions are converted to photons in a strong magnetic field. However, no signal of the axion has been reported.

The PBH is a dark matter candidate with completely different properties from the above, not particle. PBHs are produced by the gravitational collapse of the large density fluctuations in the early universe. The production process depends on the model. Due to the recent progress of the detection of gravitational waves, the PBH can be observed complementary to the traditional one of electromagnetic waves. The PBH has not been observed and limited the PBH ratio in the dark matter by the observations of microlensing, gravitational lensing,

dynamics of the galaxy, etc. In almost all masses of the PBH, the hypothesis that all dark matter is the PBH is rejected. The gravitational-wave astronomy is improving nowadays, novel methods are proposed [19].

2.3 Experiments to search for WIMPs

2.3.1 Direct search experiment

A number of experiments have been proposed and performed for detecting the scattering signal of dark matter on the ground, but no consensus has yet been reached that evidence of scattering has been detected. A rate R depending on nuclear recoil energy E_R of the dark matter are described with the following equation,

$$\frac{dR(E_R,t)}{dE_R} = N_T \frac{\rho_0}{m_{\rm DM}} \int_{v>v_{\rm min}} v f(\vec{v}+\vec{v_E}(t)) \frac{d\sigma(E_R,v)}{dE_R} d^3v, \tag{2.7}$$

where N_T is a number of target nuclei, ρ_0 is a local DM dencity, f is a function of a velocity distribution on the Earth's frame, and $\sigma(E_R,v)$ is a cross section. The $v_{\rm min}$ is a miminum velocity to recoil. For the elastic and inelastic scattering, the $v_{\rm min}$ is given as,

$$v_{\rm min} = \sqrt{m_N E_R/2m_r^2} \text{ and} \tag{2.8}$$

$$v_{\rm min} = \sqrt{m_N E_R/2m_r^2} + E^*/\sqrt{2m_N+E_R}, \tag{2.9}$$

respectively. The m_r is a reduced mass of the nucleus-dark matter system and E^* is nuclear excitation energy. Spin-independent (SI) and Spin-dependent (SD) interactions are assumed, which are coupled to the charge and spin of the nucleus, respectively. The SI and SD interaction contribute the time-integrated cross section as,

$$\frac{d\sigma(E_r,v)}{dE_R} = \frac{m_N}{2m_r^2 v^2} \left(\sigma_0^{\rm SI} F_{\rm SI}^2(E_r) + (\sigma_0^{\rm SD} F_{\rm SD}^2(E_r)\right), \tag{2.10}$$

where the σ_0 is a cross section in zero momentum transfer and $F^2(E_r)$ is nucleus form factor for each SI and SD interaction. The total cross section of the dark matter is sum of the SI and SD interaction. The cross section of the SI interaction to nucleus, $\sigma^{\rm SI}_{{\rm DM}-N}$ is written with a cross section of dark matter-neutron and proton, $\sigma^{\rm SI}_{{\rm DM}-n}$ and $\sigma^{\rm SI}_{{\rm DM}-p}$, as,

$$\sigma^{\rm SI}_{{\rm DM}-N} \sim A^2 \frac{\mu^2_{{\rm DM}-N}}{\mu^2_{{\rm DM}-p}} \sigma^{\rm SI}_{{\rm DM}-n}, \tag{2.11}$$

where the μ is a reduced mass. For the search of SI interactions, targets with large Z, i.e., atomic number, are advantageous. For the SD interaction search, the cross section is given as,

$$\sigma^{\rm SD}_{{\rm DM}-N} = \frac{\lambda^2 J(J+1)}{0.75} \frac{\mu^2_{{\rm DM}-N}}{\mu^2_{{\rm DM}-p}} \sigma^{\rm SD}_{{\rm DM}-p}. \tag{2.12}$$

The λ is a Lande factor, the J is a total spin of the nucleus. The widely-used SD dark matter targets are summarized in Table 2.1.

SD dark matter target	unpaired nucleon	natural abundance [%]	$\lambda^2 J(J+1)$
^{1}H	proton	100	0.750
^{7}Li	proton	92.5	0.411
^{19}F	proton	100	0.467
^{23}Na	proton	100	0.041
^{73}Ge	neutron	7.8	0.065
^{127}I	proton	100	0.023
^{129}Xe	neutron	26.4	0.124
^{131}Xe	neutron	21.2	0.055

TABLE 2.1. Widely-used targets for SD dark matter search.

In recent experiments, the volume of the target has been increased and the background level has been reduced in order to achieve ultimate sensitivity. Experiments that effectively utilize two or more types of signals (light, charge, and heat) to discriminate backgrounds have succeeded in setting an upper limit on the scattering cross section of dark matter. The experiments with the lowest limits are shown in Table 2.2.

Experiment	Target	Detector	Signals	Fiducial mass [kg]	Cross section [cm^2]	dark matter mass [GeV/c^2]	Ref.
Spin independent high mass (>5 GeV/c^2)							
PandaX-4T	Xe	Dual-phase TPC	light + charge	3700	3.3×10^{-47}	30	[20]
XENON1T	Xe	Dual-phase TPC	light + charge	1042	4.1×10^{-47}	30	[1]
LUX	Xe	Dual-phase TPC	light + charge	118	1.1×10^{-46}	50	[21]
DEAP-3600	Ar	Single-phase scintilator	light	2000	3.9×10^{-45}	100	[22]
DarkSide-50	Ar	Dual-phase TPC	light + charge	46	1.14×10^{-44}	100	[23]
SuperCDMS	Ge	Solid-state cryogenic	charge + heat	12	1.0×10^{-44}	46	[24]
Spin independent low mass (<5 GeV/c^2)							
LUX (Migdal)	Xe	Dual-phase TPC	charge	118	6.9×10^{-38}	2	[25]
XENON1T (Migdal)	Xe	Dual-phase TPC	charge	1042	3×10^{-40}	2	[26]
XENON1T (ionisation only)	Xe	Dual-phase TPC	charge	1042	3.6×10^{-41}	3	[27]
DarkSide-50 (ionisation only)	Ar	Dual-phase TPC	charge	20	1×10^{-41}	2	[28]
CDMSLite	Ge	Solid-state cryogenic	charge	0.6	2×10^{-40}	2	[29]
CRESST	O	Solid-state cryogenic	light + heat	0.024	1×10^{-39}	2	[30]
NEWS-G	Ne	Proportional Counter	charge	0.3	1×10^{-38}	2	[31]
DAMIC	Si	CCD	charge	0.3	1×10^{-41}	7	[32]
Spin dependent proton							
PICO-60	F	Bubble Chamber	heat	49	3.2×10^{-41}	25	[33]
Spin dependent neutron							
XENON1T	Xe	Dual-phase TPC	light + charge	1042	6.3×10^{-42}	30	[34]
LUX	Xe	Dual-phase TPC	light + charge	118	1.6×10^{-41}	40	[35]
PandaX-II	Xe	Dual-phase TPC	light + charge	364	1.6×10^{-41}	35	[36]

TABLE 2.2. Typical dark matter search experiments and their upper limits for the cross section.

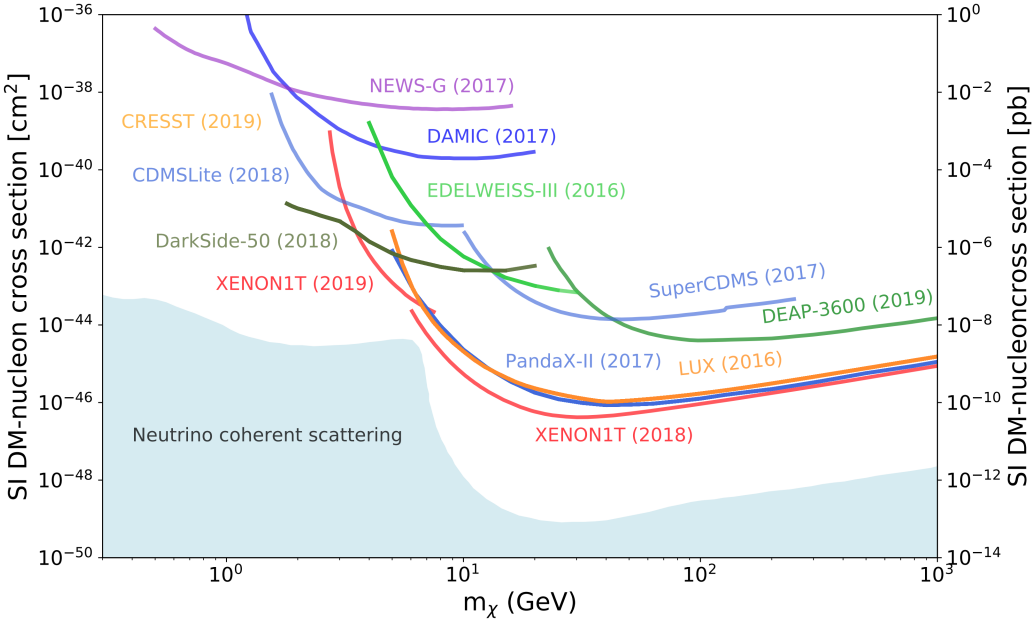

FIGURE 2.6. Current status of the sensitivity for WIMP with direct detection experiments. The space above the lines is excluded at a 90% confidence level [37].

Figure 2.6 shows the current limits for SI searches.

XENON1T experiment is one of the world-leading experiments with xenon dual-phase TPC performed at the Gran Sasso National Laboratory (LNGS) in Italy. The detector achieved to strongly discriminate electron recoil backgrounds with light and charge signals and set the limits for the SI scattering cross section of WIMP-nucleons. The XENON1T experiment acheived the limit $4.1 \times 10^{-47}\mathrm{cm}^2$ for 30 GeV/c^2 WIMPs [1]. The same technique is used by the LUX and PandaX Experiment. Large Underground Xenon Experiment (LUX) is located in Sanford Underground Laboratory (SURF, formerly the Deep Underground Science and Engineering Laboratory, or DUSEL) in the Homestake Mine in Lead, South Dakota. The LUX reported the final limit as $1.1 \times 10^{-46}\mathrm{cm}^2$ for 30 GeV/c^2 WIMPs [21]. Particle AND Astrophysical Xenon (PandaX) experiment is located in China Jinping Underground Laboratory. Recently, the PandaX experiment is upgrading their detector for 4 tons fiducial mass of xenon. They reported the lowest result, $3.3 \times 10^{-47}\mathrm{cm}^2$ for 30 GeV/c^2 WIMPs with their commissioing run [20]. The next-generation experiment, XENONnT and LZ which use more Xenon target, total 5.9 t and 7.0 t respectively, is under commissioning or taking data. The XENONnT Experiment is an upgrade of the XENON1T Experiment, which is described in this paper. The LZ experiment is constructed with the LUX and ZEPLIN collaboration. DARWIN as a future experiment with the Xenon dual-phase TPC is planned by many XENONnT and LZ collaborators. The DARWIN is the ultimate dark matter search experiment and will involve 40 tons of xenon [38].

Another noble gas target, argon is also used for the SI dark matter search. The strong pulse shape descrimination (PSD) technique is available for liquid argon. DEAP-3600 experiment uses a scintillation detector filled with 3.6 tons of liquid argon at SNOLab. The DEAP-3600 experiment reported their limit, $3.9 \times 10^{-45}\mathrm{cm}^2$ for 100 GeV/^{2} WIMPs[22]. Darkside-50 experiment uses Argon as a target, and their detector is dual-phase TPC at LNGS. The limit of the Darkside-50 is $1.14 \times 10^{-44}\mathrm{cm}^2$ for 100 GeV/c^2 WIMPs [23]. As a scale-up experiment of the Darkside-50, Darkside-20k Experiment is under construction and a larger experiment with Argon called ARGO is planned for the future.

In the XENON1T and Darkside-50 experiments, the threshold is lowered by using only the charge-derived signal with high luminosity, which is a good limitation for dark matter in lower mass regions [27, 28]. In addition, in experiments on liquid noble gas targets, we are searching for low-mass regions using inelastic electron scattering and ionization signals following nuclear recoil. The XENON1T and LUX experiments search for dark matter in the Sub-GeV region by observing bremsstrahlung photons and Migdal effect [39], which is believed to exist. The verification of the Migdal effect itself is also planned [40].

NEWS-G is an experiment performed at Laboratoire Souterrain de Modane (LSM). The detector is a neon gas proportional counter. In particular, the detector is operated with a light noble gas and the energy threshold is 10 keV with electron equivalent, thus the experiment is sensitive for light dark matter. The upper limit is reported as 1×10^{-38} cm^2 for 2 GeV/c^2 WIMPs[31].

SuperCDMS and CDMSLite at Soudan [29, 24], CRESST at LNGS [30], EDELWEISS at LSM [41] are experiments with solid-state cryogenic detectors. The solid-state cryogenic detectors are characterized by high energy resolution and low energy threshold, while it is difficult to make them large. They are also sensitive to a single elementary charge and can detect dark matter electron scattering. Especially, they are sensitive to low mass dark matter.

The DAMIC experiment aims to detect the nuclear and electronic recoil caused by dark matter particles in the bulk silicon of a charge-coupled device (CCD) at SNOLab [32]. The CCD can reconstruct the position in three dimensions and can reconstruct the particle species using tracks.

PICO-60 is an experiment for SD dark matter detection with a superheated bubble chamber. The target is ^{19}F, which is one of the most enhanced nuclei for the SD dark matter cross section (Table 2.1). The chamber is a threshold-type detector and insensitive for electron backgrounds. The PICO-60 experiment set the upper limit of the SD dark matter cross section, $3.2 \times 10^{-41}\mathrm{cm}^2$ for 25 GeV/c^2 [33].

Historically, DAMA/LIBRA experiment had reported that results from nearly 20 year show annual modulations in signal rates that meet the requirements of the standard WIMP model [42] due to the Earth's orbit in the galaxy. The detector is installed at LNGS and consists of pure NaI:Tl scintillators with a total mass of about 250 kg [43]. The statistical significance

of the annual modulation reaches 12σ in the 2-6 keV energy range but has not been reproduced in other experiments. However, the cross section of the dark matter evaluated by the DAMA/LIBRA is not consistent with the other experiments.

COSINE is an experiment in which one of the main objectives is to cross-check the results of annual modulation with the statistical superiority of DAMA/LIBLA. As in DAMA/LIBLA, NaI:Tl solid scintillators were used as targets. In the latest results [44], although the COSINE-100 results strongly constrain the results of the DAMA/LIBLA annual modulation, several possibilities have been proposed to keep the results of the two experiments consistent (e.g. [45]).

As a different approach from the observation of the annual modulation of the rate, an experiment using a directionally sensitive detector is planned. Cygnus is a proto collaboration to develop a gas TPC for dark matter search. Signals originating from the direction of dark matter arrival (the galactic plane, in the direction of Cygnus as seen from the Earth) will provide definitive evidence of dark matter. The directional detectors may be able to search beyond the neutrino floor, the ultimate background event. On the other hand, a technique to enlarge the gas TPCs for several tons scale has not been established.

2.3.2 Backgrounds in direct experiments

In dark matter direct search experiments, (i) ambient/intrinsic radiation, (ii) cosmic rays, and (iii) neutrinos are the main background events.

The (i) ambient and intrinsic radiation is a α, β, and γ rays. Radioactive materials including detector materials and laboratory material produce the radiation. The typical radioactive nuclei are ones in Uranium and Thorium chains described in Appendix B, ^{40}K, ^{60}Co, and others. These radiations can produce signals like dark matter. The approach to discriminate these background events is reducing these contaminations in the detector material. The component materials are cared with composed by lower radioactivities and measured these radio activities with a germanium detector or an Inductively Coupled Plasma Mass Spectrometry (ICP-MS). These experiments prepare a veto detector or shield of water, lead, or copper to reduce external γ-rays. If the detector is large, massive, and able to reconstruct the interaction vertex, self-shielding is available. In addition, detectors with high energy resolution can characterize these background events with the measured energy spectrum. Another approach is particle identification. Detectors in particular measuring two or more different types of signals, e.g., charge and light, is possible to evaluate the original interactions. For example, a dual-phase time projection chamber is able to discriminate the signals of nuclear recoils and electron recoils. In the case that the Uranium and Thorim series nuclei are serious backgrounds, the delayed coincidence method is used. For example, to remove the α decay of the ^{214}Po, the parent nucleus, ^{241}Bi is useful to tag the decay. After the ^{241}Bi β decay, the ^{214}Po immidiately decays with half-life, 160 μs.

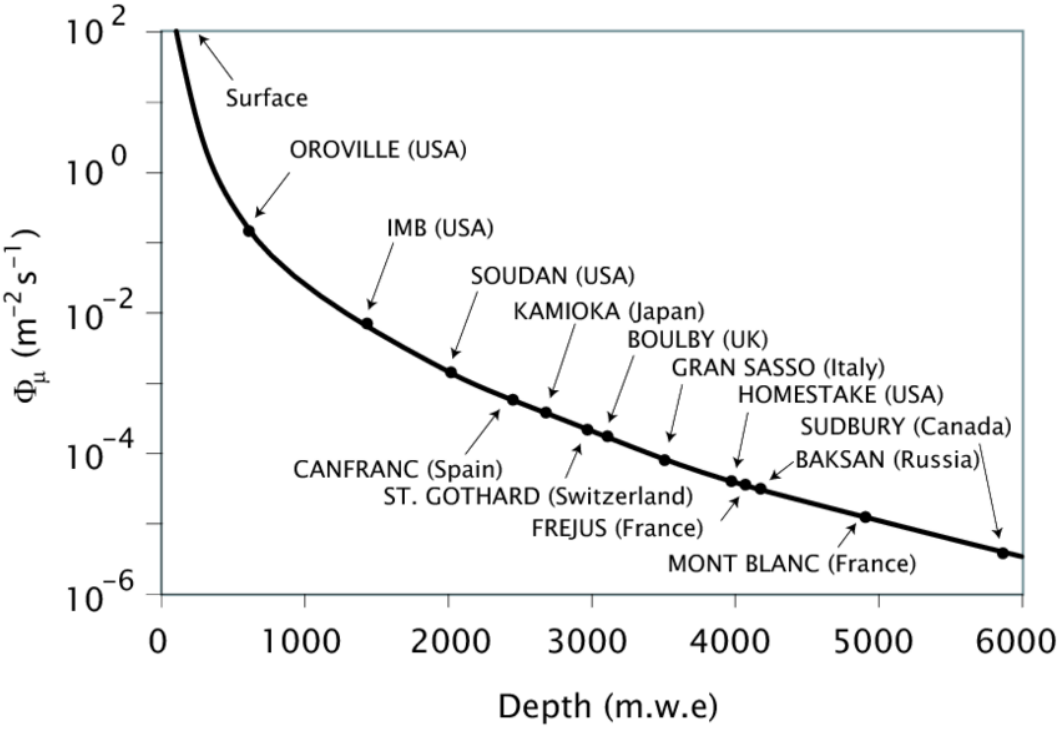

FIGURE 2.7. Depthes and cosmic muon fluxes in underground laboratories around the world [46]. The depthes are shown in water equivalent meter (m. w. e.) for muon shielding.

The (ii) cosmic rays, mainly cosmic muon will be also background events. In order to reduce the amount of the muon, experiments are performed in underground laboratories. Figure 2.7 shows the underground laboratories around the world. The impact of the cosmic muon can be reduced by some orders of magnitude. Except for the direct muon signal, the muon activates the nucleus in the detector material. These nuclei rerely produce high energy γ-ray, thus it will be backgrounds for such low-background experiments. Recently, a water Cherenkov detector or a liquid scintillator as an outer detector is used to veto the muons.

The (iii) neutrino is the ultimate background for direct dark matter searches to detect their scattering. Solar neutrino, atmospheric neutrino, and diffuse supernova neutrino scatter target nuclei like WIMP dark matter. In the case of the solar neutrino with p-p chain, the backgrounds are observed into approximately 10-25 events/(t y) below 100 keV with electron recoil, thus it is not serious backgrounds for WIMPs. On the other hand, ^{8}B neutrino produces nuclear recoil backgrounds events into 10^3 events/(t y) below several keV for a high atomic mass target at maximum. The neutrino background events are unavoidable with the current major techniques. The limitation to search the WIMP cross section is known as ‘neutrino floor’. Directional search experiments only have a chance to explore the dark matter beyond the neutrino floor.

The current experiments are designed to discriminate these backgrounds with a combination of these techniques. In particular, detectors that have the ability to discriminate the incident particles are leading the WIMP searches.

2.4 Other dark matter searches

In addition to the direct searches for dark matter, there are also indirect searches to detect signals from the decay or annihilation of dark matter, and collider searches to produce dark matter using accelerators and colliders.

2.4.1 Indirect searches

Due to gravitational interaction, the number density of dark matter increases in massive regions such as the galactic halo and the solar core. A typical method of an indirect search is detection through the products of annihilation or decay of dark matter particles. These indirect searches aim to find products, γ-ray, neutrino, and anti-particle, of the annihilation or the decay of the dark matter. No experiment has been reported significant evidence of the products and experiments have upper limits for annihilation (decay) rate for the dark matter.

Assuming the process to produce γ-rays from dark matter, the most popular target is nearby dwarf spheroidal galaxies because they don't have a significant background to observe γ-ray and X-ray. In addition, the inner region of the Milky Way is a major target. The region has much dark matter, on the other hand, many backgrounds because of the brightness. The observed energy spectrum of these γ-rays may contain unique information of dark matter. When the dark matter is annihilated into two γ-rays or two neutrinos, it is almost monoenergetic and has the energy of the mass of dark matter. There is no known source of monoenergetic γ-rays in the energy region above GeV. Many telescopes, Fermi Large Area Telescope (Fermi-LAT), HESS, VERITAS, MAGIC, and HAWC have provided an unprecedented sky map of the γ-ray. Fermi-LAT reported the excess of γ-rays that is explained with the dark matter anihilations [47], but the signal is under discussion [48].

Neutrino is another candidate as a product of dark matter. The dark matter is assumed to be captured in celestial bodies. For dark matter masses at around the GeV/c^2 region, evaporation from the celestial bodies is important [49]. The captured dark matter lost energy in the celestial bodies then evaporate, the bodies are heated up. The properties of dark matter are limited by the warming of cold planets like Uranus [50], changes in stellar structure and seismic activity on the sun [51], and the unusual heat flow of the earth [52]. Within the Standard Model, an annihilation to neutrinos is considered as an example of evaporation. The energy of a typical neutrino exceeds that of a solar neutrino, allowing background-free searches. Searches of IceCube [53] and ANTARES [54] experiments have not reported any significant signal.

Stable anti-particles generated from dark matter are also searched. These charged particles are in the cosmic rays. Generally, dark matter is assumed to produce the same numbers of particles and anti-particles. A target is a positron, which is created from dark matter. AMS-02 Experiment [55] reported the excess of the positron beyond general production from inelastic scattering of cosmic rays. However, the excess has not to be observed in other corresponding channels, γ-ray, and anti-proton. Another target is anti-nucleus such as anti-deuteron and anti-Helium. The anti-nucleus is produced with lower energy than ones created with inelastic scattering of cosmic rays. GAPS Experiment is searching for the lower energy anti-nucleus less than 0.25 GeV.

2.4.2 Colider and accelarator searches

Collider searches try to produce dark matter using collider. In particular, the ATLAS and CMS experiments are searching for dark matter using the proton-proton Large Hadron Collider (LHC) at CERN [56, 57, 58, 59, 60]. The basic strategy of the collider search is to reconstruct the events to search for "missing" energy and momentum that the supposedly produced dark matter carries away without interacting with the detector. In general, it is assumed that the model interacts in some interactions with the particles of the Standard Model. For example, they assume models interacting via Higgs or Z-boson exchange, effective field theories with heavy mediators, supersymmetric models, and others. The signal of dark matter can be considered depending on these models. Concrete examples are the detection of the transverse momentum and the change of an invariant mass distribution or an angular distribution of di-jet and di-lepton when the Standard Model particles and dark matter are produced simultaneously. No dark matter signal has been observed in the LHC searches so far, and limits have been reported for the couplings and the cross sections. While these results can be compared with the results of direct search experiments, they are often model-dependent because of the model-specific cuts to optimize the ratio of signal/background. Collider searches do not provide conclusive evidence for the non-existence of dark matter and are complementary to direct search experiments.

In the accelerator searches, various approaches have been investigated mainly for the purpose of light dark matter. For light dark matter χ and mediator A', following approaches, (1) Missing mass of $e^+e^- \to \gamma(A'\chi\bar{\chi})$ or $e^-p \to e^-p(A'\chi\bar{\chi})$, (2) missing momentum and energy of $eZ \to eZ(A'\chi\bar{\chi})$, (3) scattering at the beam dump of electron and proton, and (4) direct detection of dark photon are considered [61].

CHAPTER 3

XENONnT Experiment

This chapter explains XENONnT Experiment and its subsystems.

3.1 Overview

XENONnT is a grade-up experiment of XENON1T, which set the world limit for WIMPs dark matter. The XENONnT detector is placed an underground (∼3,600 m water equivalent) of Istituto Nazionale di Fisica Nucleare (INFN) LNGS, Italy to avoid the effect of cosmic rays. The XENONnT experiment has four major improvements from the XENON1T experiment, larger TPC, liquid xenon purification, radon distillation, and neutron veto system. In this chapter, an overview of the XENONnT experiment and the first three improvements are described. The neutron veto system is explained in Chapter 4.

3.2 XENON dual-phase time projection chamber

Xenon is one of the most suitable targets for the search of elastic scattering of WIMPs because of its large atomic mass (A∼131). Table 3.1 shows the natural composition of xenon. Most of the xenon isotopes are stable and the only two isotopes, ^{124}Xe and ^{136}Xe have long half-lives. In addition, xenon is a noble gas, and purification of radioactive impurities is relatively easy. Moreover, the dual-phase TPC makes it possible to reconstruct the three-dimensional event positions and to discriminate nuclear recoil (NR) against electron recoil (ER) backgrounds.

Xenon isotope	Natural abundance (%)	Half-life	Decay mode
^{124}Xe	0.095	1.8×10^{22} y	Double EC
^{126}Xe	0.089	Stable	
$^{128-132}$Xe	80.3	Stable	
^{134}Xe	10.43	Stable	
^{136}Xe	8.8	2.2×10^{21} y	Double β

TABLE 3.1. Natural composition of xenon.

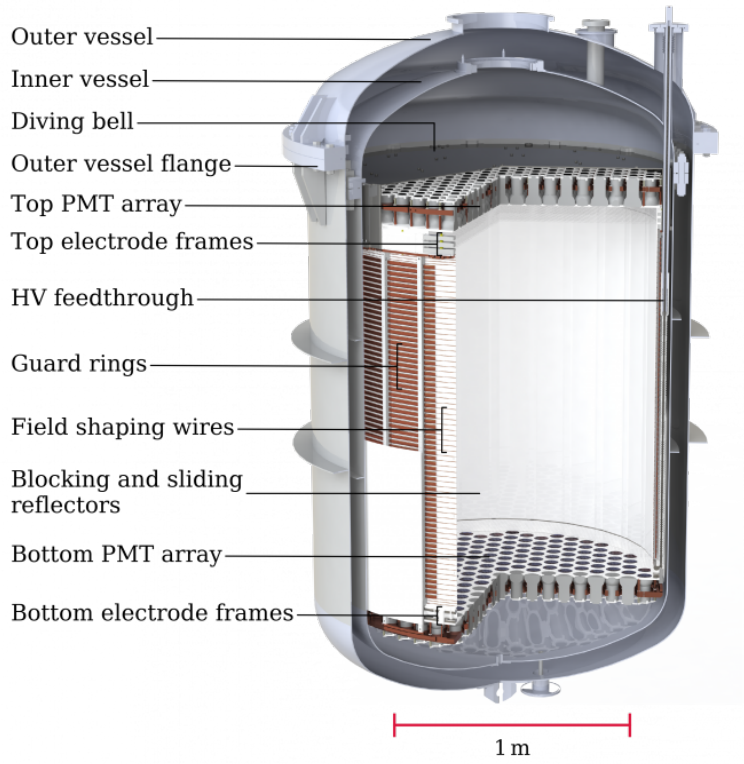

FIGURE 3.1. Components of TPC of XENONnT Experiment. The TPC is filled with xenon.

The main detector of the XENONnT experiment is a xenon dual-phase TPC. Figure 3.1 shows a schematic diagram of the TPC of the XENON detector. The core of the XENONnT TPC is a liquid and gas phase by approximately 8.2 tons of xenon. Xenon is enclosed in a cryostat (1.3 m in diameter and 1.5 m in height) with a double structure of the outer and inner vessels to prevent heat inflow from the outside, and the inner pressure is adjusted to keep the gas-liquid dual-phase.

A total of 494 PMT, 253 and 241, are installed top and bottom of the cryostat, respectively. They are 3 inch PMTs, R11410-21 supplied by Hamamatsu Photonics K.K. [62]. It is a special model for the underground experiment, which can operate at low temperatures down to -110°C and consists of lower radioactive materials to reduce the background events. The PMT type is box and line and its dynode has 8 stages. The average Quantum Efficiency (Q.E.) of the top array PMT is 31.9% and that of the bottom array PMT is 36.4%. Figure 3.2 shows the Q.E. measured by Hamamatsu Photonics K.K for a photon which wavelength of xenon scintillation light (175 nm). PMTs with higher Q.E. are used for the center of the array.

Three electrodes, called the anode, gate, and cathode, are placed in the TPC to create an electric field. The electrodes are 216 μm thick stainless steel wires stretched parallel to the stainless steel ring. (304 μm thick for cathode). The pitch of the upper electrodes (anode and

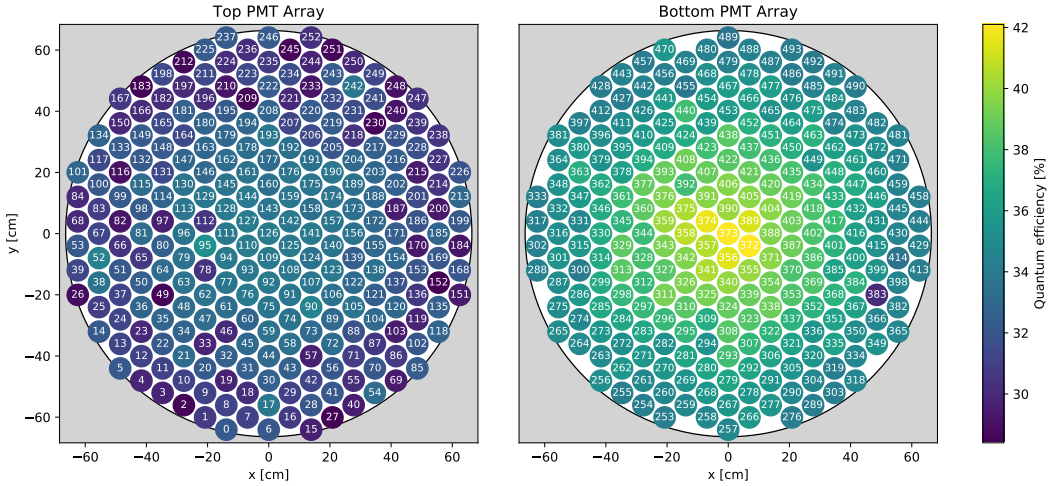

FIGURE 3.2. Map of the PMT Q.E. provided by Hamamatsu Photonics K.K. for 175 nm photon. The numbers show the PMT ID.

gate) is 5 mm, and the pitch of the lower electrodes (cathode) is 7.5 mm. For the gate and anode, two and four wires, respectively, 304 μm thick, are added perpendicular to all other wires. This is to suppress the deformation of the electrode surface. In addition, two screening electrodes (top screen, bottom screen) are placed just below (directly above) the top (bottom) PMT array to shield the PMT from the electric field generated by the anode (cathode). In addition, copper guard rings are placed on the sides to align the electrodes. The inner side of the TPC is surrounded by a reflective material, PolyTetraFluoroEthylene (PTFE) to increase the light collection efficiency. Each part of the TPC was cleaned in a clean room on the ground laboratory to prevent the pollution of radioactive materials. The TPC was assembled in the cleanroom, packed with plastic wrap, and brought to the underground laboratory.

Figure 3.3 shows the principle of particle detection with a dual-phase xenon TPC. Incident particles (WIMPs, background events such as neutrons, and environmental γ-rays) scatter xenon nuclei in a liquid part of the TPC. The xenon nucleus excited by the scattering scintillates upon de-excitation and emits a scintillation light. The light yield is 42,000 photons per 1 MeV electron. In the case of the directly excited state, there is a process involving recombination, and each of these processes can be described in Equations 3.1 and 3.2,

$$\begin{aligned} \mathrm{Xe}^* + \mathrm{Xe} &\rightarrow \mathrm{Xe}_2^* \\ \mathrm{Xe}_2^* &\rightarrow 2\mathrm{Xe} + h\nu \text{ and} \end{aligned} \tag{3.1}$$

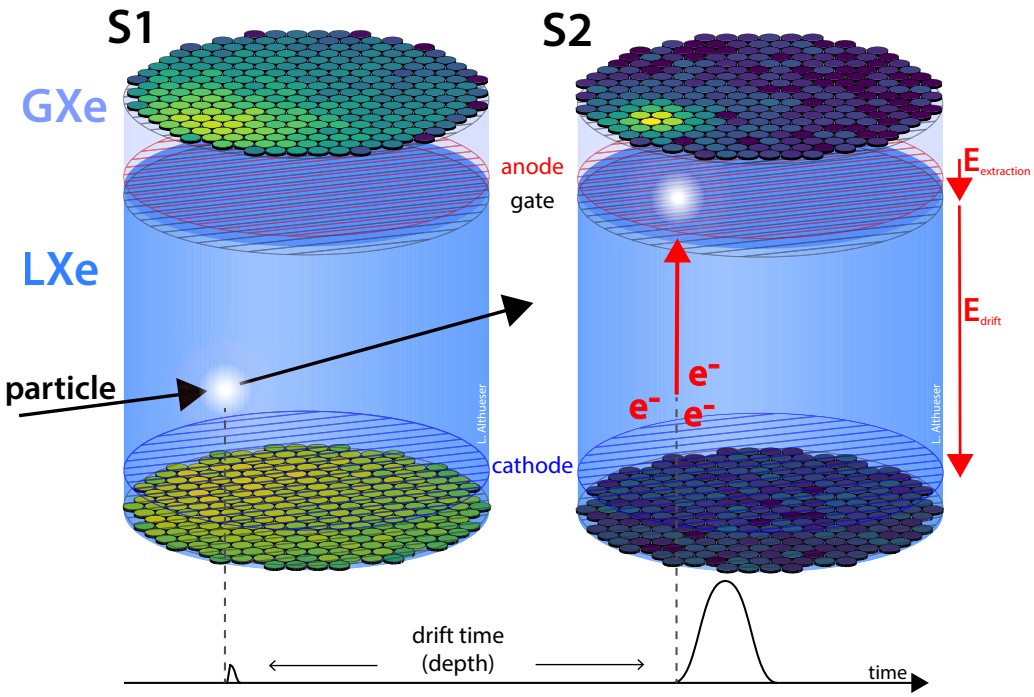

FIGURE 3.3. Dual phase TPC working principle

$$
\begin{aligned}
\mathrm{Xe}^{+} + \mathrm{Xe} &\rightarrow \mathrm{Xe}_2^{+} \\
\mathrm{Xe}_2^{+} + e^{-} &\rightarrow \mathrm{Xe}^{**} + \mathrm{Xe} \\
\mathrm{Xe}^{**} &\rightarrow \mathrm{Xe}^{*} + \mathrm{heat} \\
\mathrm{Xe}^{*} + \mathrm{Xe} &\rightarrow \mathrm{Xe}_2^{*} \\
\mathrm{Xe}_2^{*} &\rightarrow 2\mathrm{Xe} + h\nu,
\end{aligned}
\tag{3.2}
$$

where Xe* is an excited state of xenon. By both processes, xenon emits scintillation light. This signal of scintillation called S1 is detected by the upper and lower PMT arrays. The emission wavelength is 178 nm, which enables detection by the PMTs without a wavelength shifter.

A drift electric field of 200 V/cm is formed vertically downward in the liquid xenon phase. The electrons ionized by xenon nuclei are drifted to a liquid phase region at the upper part of the detector by the electric field. A stronger electric field is applied at the interface between the gas and the liquid to extract the reached electron. Then the electron emits electroluminescence light in the gas phase. This emission signal (S2) is also detected by the top PMT array. It is known that the total deposit energy E is expressed in Equation 3.3.

$$
E = (n_\gamma + n_e)W = \left(\frac{\mathrm{S1}}{g_1} + \frac{\mathrm{S2}}{g_2}\right) W, \tag{3.3}
$$

where n_γ and n_e are the total numbers of the scintillation photons and the excited electrons, respectivery [63]. The W is an average energy to make one quantum (photon or electron), 13.7 ± 0.2 eV evaluated in [64]. These parameters do not depend on the detecor conditions for example the magnitude of the electric field. S1, S2 in the equation 3.3 are proportional to n_γ and n_e. The g_1 and g_2 are the parameters depending on the detector, obtained with source calibrations.

Using the time difference (drift time) of the two signals, S1 and S2, the depth of the particle reaction vertex can be reconstructed, and by combining it with the hit pattern of the PMT array, the three-dimensional position can be reconstructed. The cross section for the photoelectric effect is 4-5 power of the atomic number, and the cross section for Compton scattering is proportional to the atomic number for γ-rays. The cross section of xenon for γ-rays is large since the atomic number is relatively large ($Z = 54$), Most of the background γ-rays from the detector material and from outside are shielded by the outer part of the TPC itself (self-shielding). Using the positional reconstruction, the external backgrounds events are observed at the outer side of the detector. The backgrounds are reduced by defining the core part of the detector as a fiducial volume, $\sim$ 4 tons of the total 8.2 tons.

The ratio of S1 to S2 also enables us to reduce the background events by discrimination of the incident particles. The WIMPs are considered to cause NR of xenon nuclei, while γ-rays and electrons from radioactive material included in the detector components are considered to cause ER. A detailed description of the discrimination can be found in Section 3.5.4.

3.3 Neutron Veto System

Neutron background events are difficult to identify because they produce NR events similar to WIMP events in the XENONnT TPC. The single-scattering events cannot be discriminated with TPC only. Neutrons are emitted from the components of the TPC and a small number of radioactive impurities in the PMTs, thus they cannot be shielded with outer detectors. In order to identify and veto these neutron events, the neutron Veto (nVeto) detector was newly installed in the XENONnT experiment as an upgrade from the XENON1T experiment. Figure 3.4 shows the entire system of the XENONnT detector. The nVeto detector is an octagonal water Cherenkov detector of about 4 m in size installed around the TPC. The nVeto detector is filled with pure water at the beginning of the experiment and then with 0.2% $\mathrm{Gd_2(SO_4)_3 \cdot 8H_2O}$ aqueous solution. WIMPs pass through the detector due to their very small reaction cross section, but the scattered neutrons are captured by the hydrogen or gadolinium in the nVeto detector and emit γ-rays. The γ-rays emit electrons with photoelectric effect or Compton scattering. These electrons emit the Cherenkov light. The nVeto detector detects the light with 120 8-inch PMTs. Since WIMPs do not emit such light, neutron background events can be eliminated. To improve the collection efficiency of the Cherenkov light, the inside of the nVeto detector is covered with a 1 mm thick ePTFE, a reflective material. The principle, detector, simulation, and analysis of nVeto will be described in detail in Chapter 4.

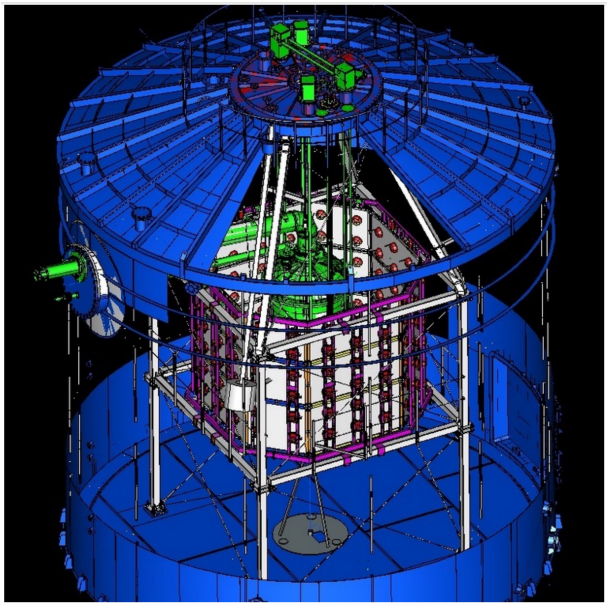

FIGURE 3.4. XENONnT detector. The inner cryostat (green) placed in the nVeto detector (white). These systems are in a water tank used as the μVeto detector (blue).

3.4 Muon Veto System

The nVeto detector and the entire TPC are placed in a cylindrical water tank with a diameter of 10 m and a height of 10 m (Figure 3.4). The outermost part is called the muon Veto (μVeto) detector, which mainly vetoes cosmic muons by detecting their Cherenkov light. Such high-energy cosmic rays rarely cause hadronic interactions in the detector, surrounding materials, and wall rock, then produce γ-rays and neutrons with relatively higher energies than other natural backgrounds. By placing water around the detector, it becomes a shield against these background events. This technique was first introduced in the XMASS experiment then widely used nowadays. The μVeto detector is equipped with 84 8-inch PMTs (Hamamatsu, R5912). This PMT also satisfies particularly high Q.E. ($\sim$30%) and low background of the material. This μVeto detector was used in the XENON1T experiment in anticipation of its use in the XENONnT experiment.

3.5 Calibration schemes

In this section, typical calibrations are described.

Figure 3.5 shows XENONnT calibration instruments. External calibration sources can be transferred close to the TPC using one of the two supporting structures, I-Belt and U-Tubes, without opening the water tank.

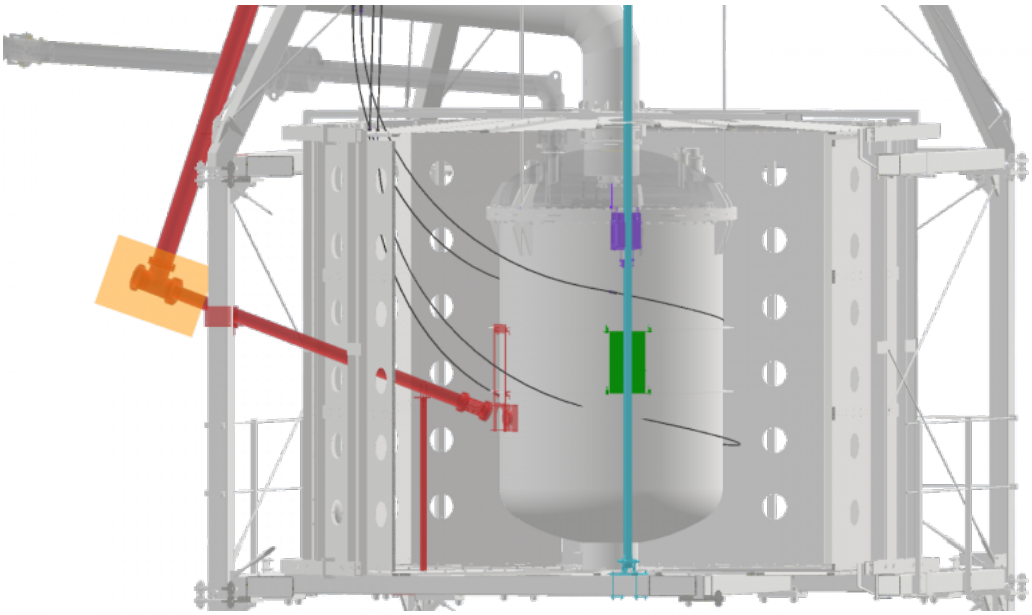

FIGURE 3.5. XENONnT external calibration instruments. The cyan belt and grey tubes are called I-belt and U-tubes to transfer external sources to their positions. The purple and green boxes are collimators for Yttrium–Belyrium source and boxes filled with air not to capture neutrons from the source in the nVeto system. The red pipe is a neutron beam pipe. A turning point of the pipe is covered with a boron shield to shield neutrons.

3.5.1 Americium-Belyrium calibration

For NR events calibration, Ameritium-Belyrium (AmBe) source is used. AmBe source is composed of americium and belyrium, and emits neutron with the following processes in Equations 3.4 and 3.5.

$$\begin{aligned} {}^{241}\mathrm{Am} &\rightarrow {}^{237}\mathrm{Np} + \alpha\ (5.5\ \mathrm{MeV}) + \gamma\ (59.5\ \mathrm{keV}) \\ \alpha + {}^{9}\mathrm{Be} &\rightarrow {}^{12}\mathrm{C}^{*} + \mathrm{n} \\ {}^{12}\mathrm{C}^{*} &\rightarrow {}^{12}\mathrm{C} + \gamma \end{aligned} \tag{3.4}$$

$^{12}\mathrm{C}^{*}$ represents the first excited state of the carbon. In the minor branch, there is a direct path to the ground state of carbon.

$$\alpha + {}^{9}\mathrm{Be} \rightarrow {}^{12}\mathrm{C} + \mathrm{n} \tag{3.5}$$

In both cases, neutrons are emitted with (α, n) reactions. The energy of the emitted γ-rays is typically 4.4 MeV. This prompt γ-rays penetrate materials, thus they are used to tag the neutron emission. In addition, γ-rays are also used to evaluate the total emission yield of the neutron with a well-known ratio of the γ particles and neutrons [65].

3.5.2 Krypton calibration

Due to the high self-shielding capability of the liquid xenon TPCs, electron and γ particle calibration by an external source are not effective. In the XENONnT experiment, one of the ER event calibrations is carried out by introducing ^{83m}Kr inside the TPC. ^{83m}Kr is produced by the electron capture decay of ^{83}Rb.

$$^{83}\mathrm{Rb} \rightarrow {}^{83m}\mathrm{Kr}\ (\text{Electron Capture, halflife 86.2 days}) \tag{3.6}$$

$$^{83m}\mathrm{Kr} \rightarrow {}^{83}\mathrm{Kr} + e\ (32\ \mathrm{keV}) + e\ (9.4\ \mathrm{keV})\ (\text{halflife 1.8 hours}) \tag{3.7}$$

^{83}Rb is exposed to the xenon circulation line, and the produced ^{83m}Kr is introduced into the TPC. This makes it possible to calibrate the TPC with electrons of monochromatic energies. Due to the short half-life of ^{83m}Kr, the effect of the source can be neglected in a few days. In addition, a distillation column is used to remove krypton from the xenon.

3.5.3 Radon calibration

In addition to the krypton calibration, radon is also used for the ER calibration. ^{228}Th undergoes a series of α and β decays, one after the other nucleus. This is known as the thorium series decay chain. The full decay chain is shown in Appendix B. ^{220}Rn, which is in the decay chain, is a noble gas and can be introduced into the detector. The decay chain emits α, β, and γ radiations for calibrations. The half-lives of the nuclei in the decay chain range from several hundred nanoseconds to several tens of minutes, except for ^{212}Pb, where the longest half-life nucleus, is 11 hours. Another advantage is that the radioactivity becomes negligible in a few days. Since ^{212}Pb emits electrons with a Q-value of 560 keV by beta decay, it can be used to calibrate low-energy electron recoil events, which are background in dark matter searches.

3.5.4 NR and ER bands

These calibrations are also used to define NR and ER bands in S1-S2 signal space. Figure 3.6 shows the magnitudes of S1 and S2 for each event using the calibration data obtained in the XENON1T experiment. The Rn calibration gives signals for ER events (a), and the ^{241}AmBe calibration gives signals for NR events caused by neutrons (b). In the XENON1T experiment, by selecting the events below the median of the NR events, the background electron events are discriminated by 99.6% for WIMP search (c). For the XENONnT experiment, these calibrations are also performed.

3.6 Data acquisition system

Figure 3.7 shows the Data acquisition system (DAQ). For TPC PMTs, the waveforms are

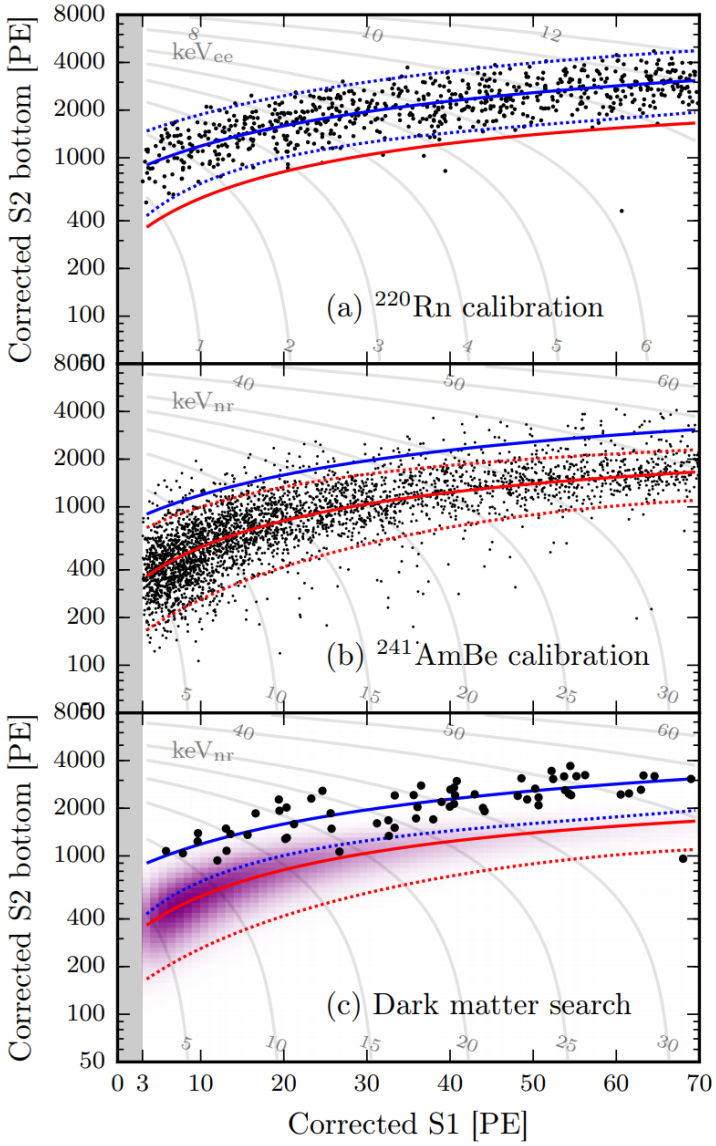

FIGURE 3.6. Demonstration of the NR and ER discrimination in the XENON1T experiment [66]. The top figure (a) and middle figure (b) show the ER and NR calibration results with ^{220}Rn and ^{241}AmBe, respectively. The X-axis and Y-axis show S1 and S2 signals. The grey dotted line is calibrated energy with Formula 3.3 in the unit of keV. The NR and ER events are well separated with their bands (red and blue) with 2σ quantiles. The bottom plot (c) shows the Dark matter search result in the XENON1T experiment. The purple distribution indicates the signal model of a 50 GeV/c^2 WIMP. No signal has been observed in the NR region.

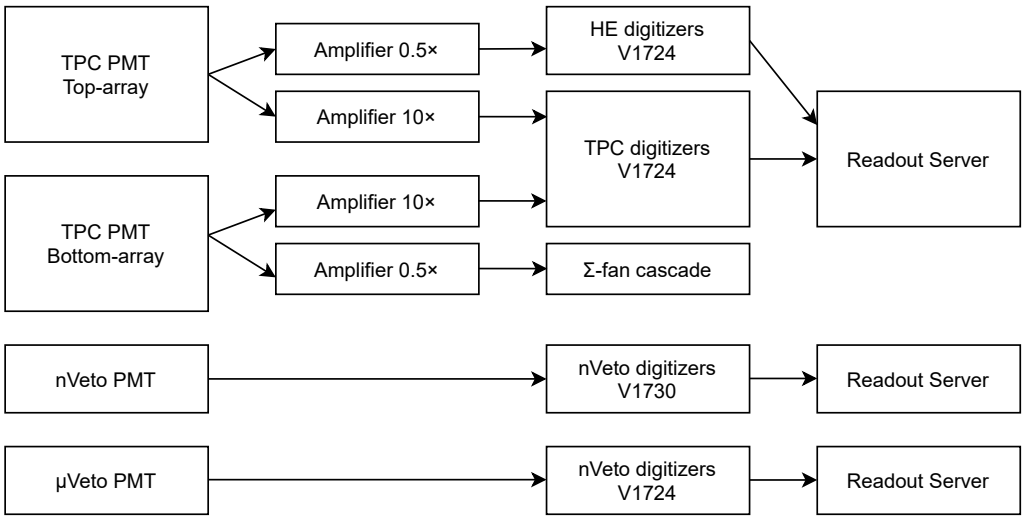

FIGURE 3.7. Design of the XENONnT DAQ system. The TPC signals are amplified 10 times for WIMP search and digitized then recorded. Other subsystems, nVeto and μVeto waveforms are recorded independently.

amplified 10 times and digitized with Flash ADCs, model V1724 supplied by CAEN S.p.A. The sampling rate of the digitizer is 100 MS/s. In addition for the top PMTs, the data for high energy events are taken with another low-gain amplifier. For the bottom PMTs, a sum of the signals is fed to the amplifier to monitor the data online. The digitizer firmware uses CAEN's Digital Pulse Processing with Dynamic Acquisition Window (DPP-DAW) [67] to perform a deadtime-less data acquisition. With the firmware, the digitizer records the waveforms which are above the threshold (Figure 3.8). The digitized data are collected with the readout servers via CAEN optical link. As a middleware, a software called redax is developed and used [68]. This redax is a DAQ with a 'NoSQL' backend. The redax is a DAQ solution capable of reading multiple channels in parallel. The redax is designed as a production system for XENONnT experiments. The nVeto and μVeto data are also taken with the similar system and redax middleware. The DAQ system for nVeto is described in Section 4.1.3. All subsystems, TPC, nVeto and μVeto data are collected independently. Synchronized clock signals are supplied for these digitizers. Then, each readout server adds Unix timestamps enhanced for nanoseconds for each waveform with a GPS module.

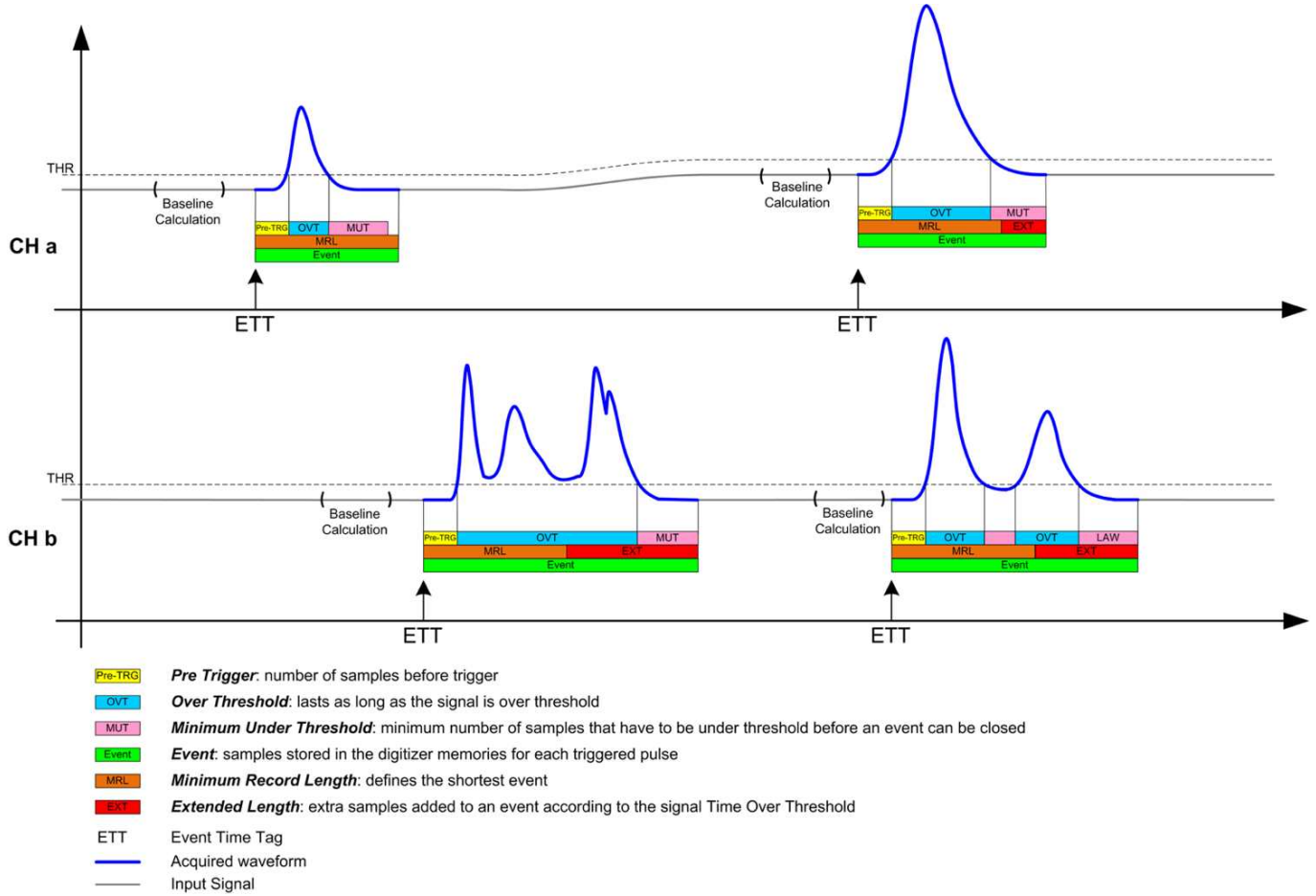

FIGURE 3.8. Aquired data scheme by DPP-DAW firmware [67]. Only data above a threshold (blue) and the peripheral regions, pre-trigger (yellow) and minimum under threshold region after the pulse (pink) are recorded with dead-time free. The data is trunked at least with the minimum record length (orange). For longer pulses, it extends the length (red). The total recorded region is defined 'Event' (green) in this firmware.

3.7 Analysis framework

XENONnT analysis framework is built on a python environment. Strax and straxen package has been developed to process the TPC data [69, 70]. The scope of the strax is a pure framework for general TPC experiments, and the straxen provides XENONnT specific analysis. Both packages are open and developed on GitHub as a public repository. The packages help us to calculate variables from large, low-level data, e.g., raw waveforms to small, high-level abstract data, e.g., event information. Figure 3.9 shows the data process flow. The group of the calculated variables is trunked in called "data type". The strax/straxen frameworks also manage the configurations to calculate each data type. The configurations are stored with a python dictionary and the configuration parameters are used on-demand during processing. For the dictionary, sufficient variations of non-overlapping hash values are provided so that data were taken with different configurations are not mixed. For example, the hash calculated with the default configurations is '2lvxbyw5vg'. The data is saved as '000001-records_nv-2lvxbyw5vg'. In this example, '000001' is run ID, 'records_nv' is the data type. When an analyzer changes one configuration parameter, e.g., software threshold, the hash is re-calculated. The data is saved as a separate file as '000001-records_nv-xr4o33zywa'. When an analyzer requires the stored data that someone has already processed, the framework provides directly the stored data without additional processing to save computing resources.

The starting data type is 'raw_records', which includes one fragment of the pulse and its Unix timestamp with nanoseconds. This data type is built with DAQ. The concept of the data structure of 'raw_records' is shown in Figure 3.10. With the XENON DAQ framework, the waveform length is dynamic. One record waveforms split with static length (110 samples) of the fragments. The 'raw_records' has also the position of the total waveforms and the total number of samples in the waveforms. After valid data, zeros are filled. In addition, 'raw_records' includes PMT ID and the baseline supplied by the DAQ.

The next 'records' is a data type that calculated baseline for 'raw_records'. This raw-level processing is heavy work for the python framework generally because python is a dynamically typed language thus it should check the types for each variable. To improve the performance, NumPy and numba libraries were used on demand. In the Numpy framework, almost all functions are implemented to work with C and Fortran language sometimes via Cython and PyPy. As a requirement, used variables should be typed but in the low-level processing variables are typed. On the other hand, numba is a framework to provide Just-in-time (JIT) compile from python source to machine code. Numba supports the subsets of python and NumPy. Under these limitations, it is possible to process the data with high performance.

Then, the fragments of the pulses are interpreted as each peak ('peaklets' and 'lone_hits'). From the previous data type, 'raw_records', it finds hits and peaks, splits the peaks, and computes the sum of the peaks and other characterized parameters. In this data type, raw waveforms are dropped and the parameters characterizing the waveforms are calculated. When there are many hits, which can be from physical events, they are stored as 'peaklets', and when they are considered to be from dark noise in PMTs, they are stored as 'lone_hits'.

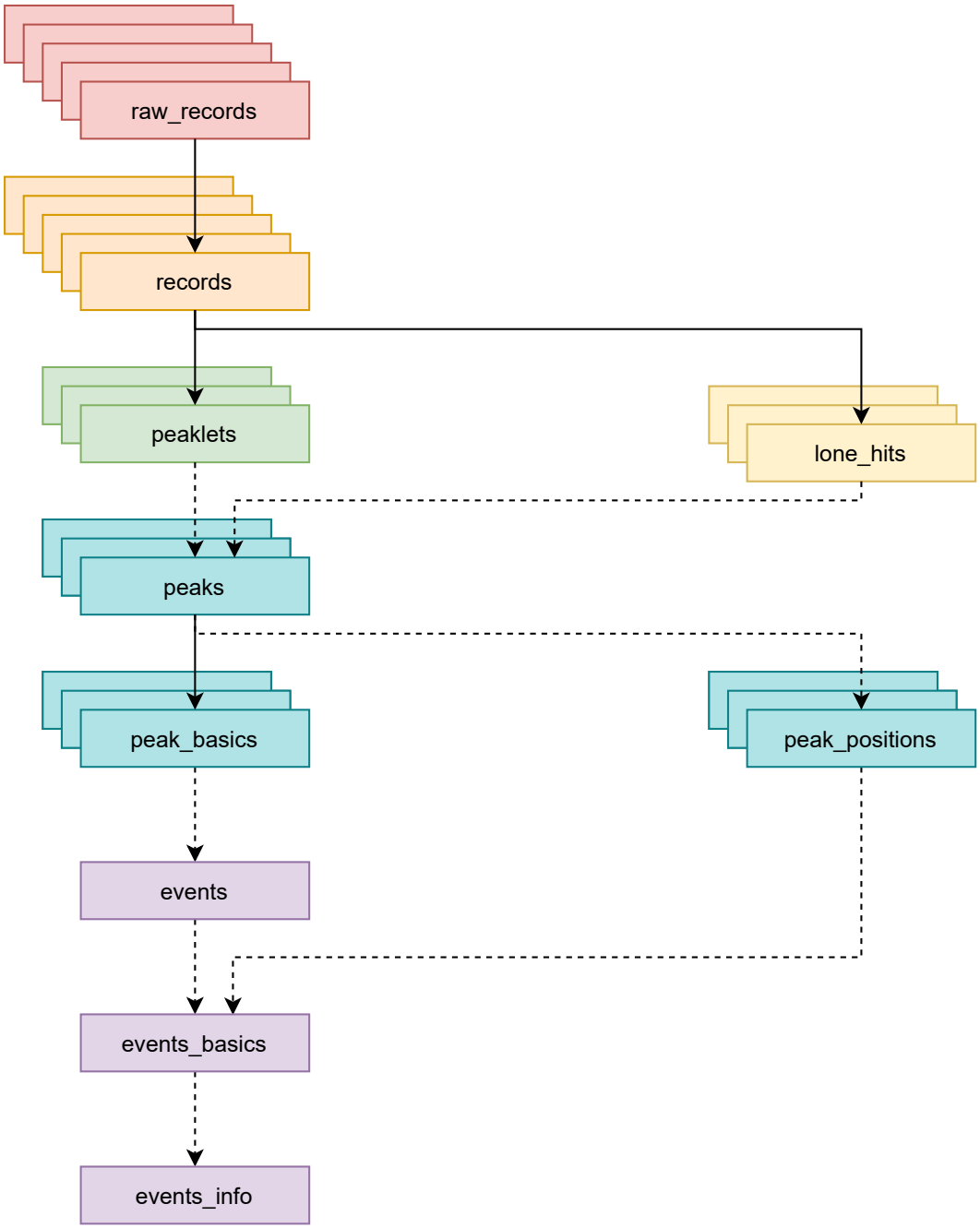

FIGURE 3.9. Analysis flow of XENONnT streaming method. The boxes show the data type and arrows show their dependencies. These colors show the data kind. Some data types are omitted.

Moreover, the number of photoelectrons including each ‘peaklets’ is also computed with the gain values.

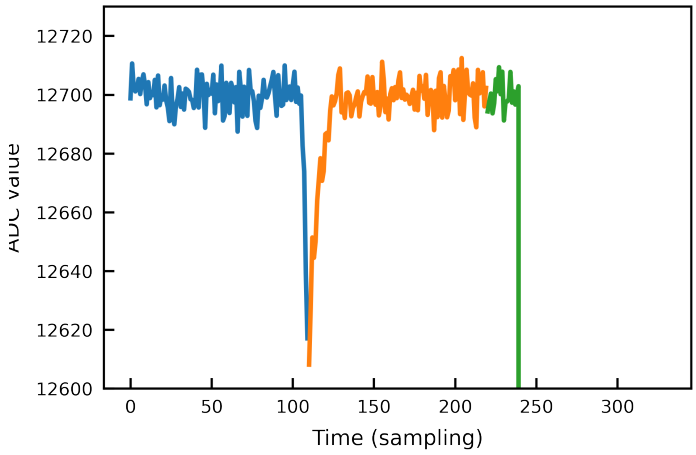

FIGURE 3.10. Concept of the 'raw_records' structure. The colored waveforms show each fragment including a 'raw_records' of the entire waveform to store with a static range of arrays. The 'raw_records' save the pulse above a threshold and small forward and backward waveforms. Zeros are filled after the valid pulse data.

The data type 'peaks' means groups of the 'peaklets' occurred near timings. It will be origins to construct S1 and S2 signals. The 'peaks' has only fundamental information of the signal. There are a variety of data types with the same level of abstraction as 'peak'. 'peak_positions_gcn', 'peak_positions_cnn', 'peak_positions_mlp' used to compute the signal potisions with machine learning techniques. Finally, these position evaluations are merged to the 'peak_positions' data type. 'peak_basics' is a data type including the basic peak properties, for example, peak timing, its width, number of contributing PMTs, peak integral, and classification of the peak (S1 or S2).

In this data type, a large amount of the data is dropped. As an interface of the analysis, 'pandas' DataFrame is available instead of the Numpy.structured_array for the later data types. The 'pandas' is the library to support data analysis and the DataFrame is an object to handle the data with advanced memory management and interface.

Finally, it is reconstructed as an event which is a group of the 'peaks' in a fixed range of time. The 'events', 'events_basic', and 'events_info' have been extracted basic information, for example, S1 and S2 signal properties, event vertexes, reconstruct energy, etc. The WIMP signal is searched in this level data type.

Data obtained with other subsystems, nVeto and μVeto, are reconstructed with a similar analysis chain then merged to the event-level data of TPC analysis. The nVeto analysis process is described in Section 4.3.

CHAPTER 4

Neutron Veto

One of the most serious background sources for WIMP search is a neutron. Neutrons generated in detector components scatter xenon nucleus in the TPC like WIMPs. In order to tag the neutron background events, a nVeto detector was newly installed in the XENONnT detector. This chapter shows the principle, components, and performance of the nVeto detector.

4.1 The nVeto detector

The nVeto detector is a water Cherenkov detector installed around the TPC. The detector consists of Gd-loaded water (or pure water), PMTs, and reflective material as shown in Figure 4.1.

4.1.1 Gd-loaded water

The nVeto detector is filled with pure water at the beginning of the experiment and then with $\mathrm{Gd_2(SO_4)_3 \cdot 8H_2O}$ aqueous solution (Gd-water) with a gadolinium mass concentration of 0.2% as a target value. The gadolinium isotopes have very high neutron capture cross sections (Table 4.1). The gadolinium sulfate needs to satisfy these points: small uranium

TABLE 4.1. Cross sections of targets for thermal neutrons in the nVeto detector [71].

Isotope	Natural abundance (%)	Cross section for thermal neutrons (barn)
^{1}H	99.99	0.33
^{152}Gd	0.20	735
^{154}Gd	2.18	85.1
^{155}Gd	14.80	60700
^{156}Gd	20.47	1.83
^{157}Gd	15.65	253000
^{158}Gd	24.84	2.20
^{160}Gd	21.86	0.786

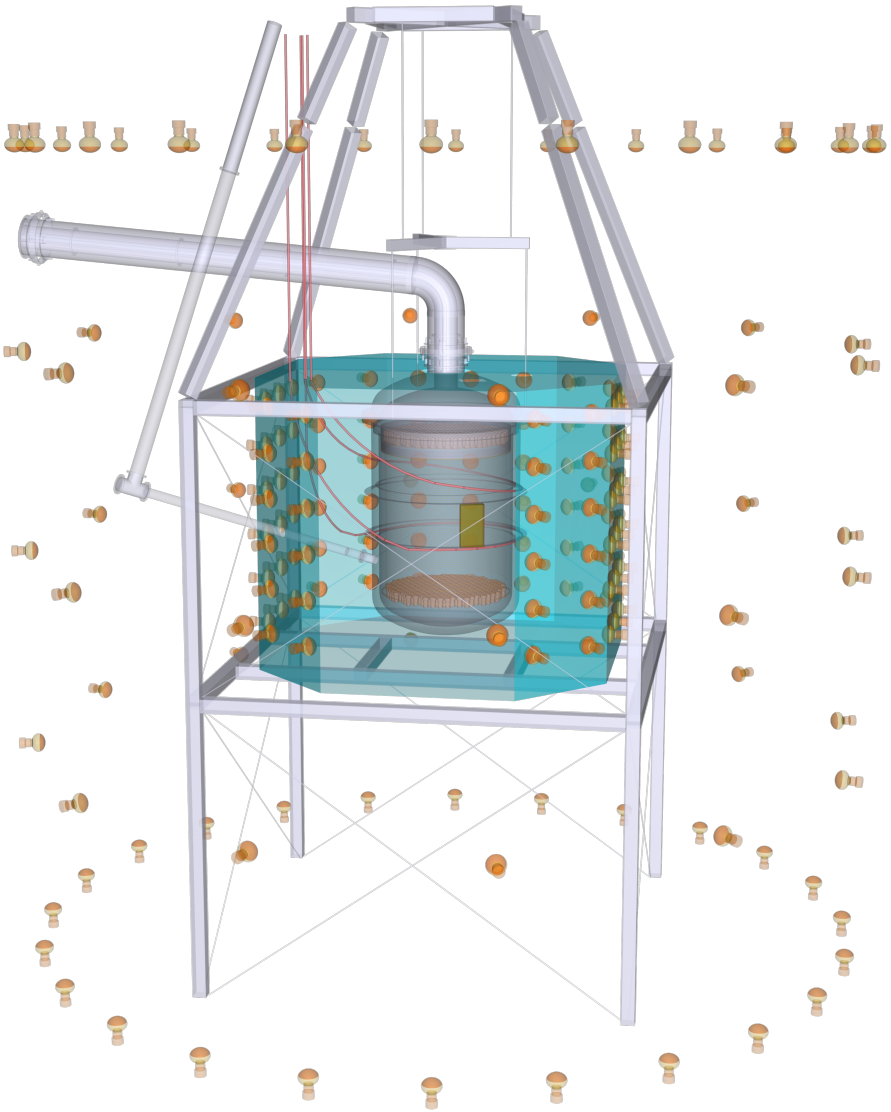

FIGURE 4.1. The XENONnT with TPC, nVeto and μVeto detectors. A center TPC is surrounded by nVeto and μVeto, water Cherenkov detectors. All components are installed in a water tank. This figure is rendered for a Geant4-based simulation geometry.

and thorium contamination, good water transparency after being dissolved in water, and the chemical stability of detector components in the water tank. The uranium and thorium contaminations are measured with germanium detectors. The water transparency was measured with spectromenters (Figure 4.2). For this experiment, low-radioactivity and chemically highly pure Gd sulfate are supplied by Nippon Yttrium Co. LTD. (NYC) and Treibacher Industrie AG (Treibacher). [1] The water tank is connected to a water purification plant for continuous

[1] We thankfully acknowledge the work of the Super-Kamiokande gadolinium group on developing a source of radio-pure gadolinium sulfate with the Nippon Yttrium Co. LTD. in Japan and giving us access to their product.

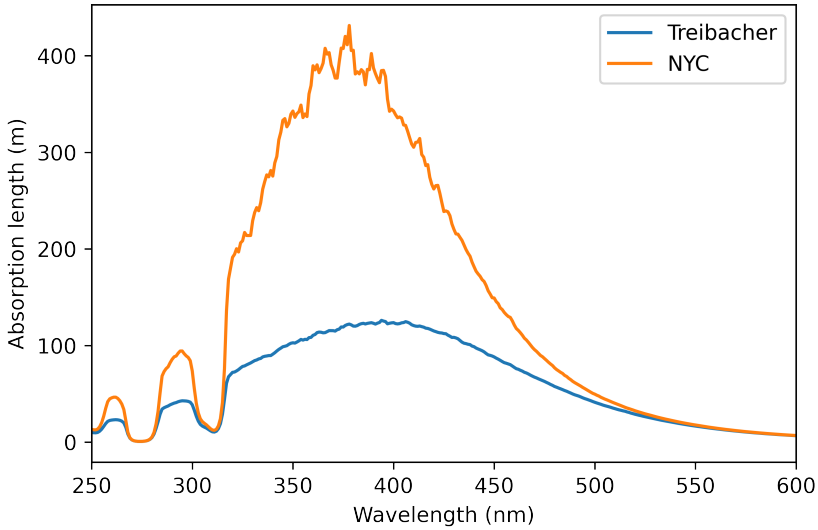

FIGURE 4.2. Measured water absorption length as a function of wavelength in the Gd-loaded water. Results for the gadolinium sulfate supplied by Treibacher and NYC are shown.

recirculation removing Gd sulfate from the water. The water transparency is monitored by sampling the water during the experiment. All materials of the components in the water tank were verified not to pollute the water with the Gd-water soaking test.

4.1.2 PMT

As a photon detector, 120×8-inch PMTs (model R5912-100-10 supplied by Hamamatsu Photonics K.K.) [62] were installed. Figures 4.3 and 4.4 show the PMT picture and drawing, respectively. This model of PMTs is certificated of being high Q.E. and low radioactivities. Performances of the 125 PMTs, including spare ones, were tested in a surface laboratory before being sent underground. The test characterized the PMT properties: gains, gain spreads, dark count rates, transit times, and transit time spreads. Then, 120 PMTs were chosen to be installed.

The nVeto PMTs are arranged in 20 columns and 6 levels in the nVeto detector. The level IDs are defined as 1-6 from the bottom. Figure 4.5 shows the nVeto PMT column ID. The PMT IDs of nVeto are 2000–2119.

Figure 4.6 shows the summary of Q.E. of the nVeto PMTs. The shown PMT Q.E. are provided by Hamamatsu Photonics K.K. The Q.E. are measured at the cathode output applying

We further acknowledge productive collaboration in developing suitable gadolinium sulfate for XENONnT by Treibacher Industrie AG in Austria.

FIGURE 4.3. PMT R5912 image [72]

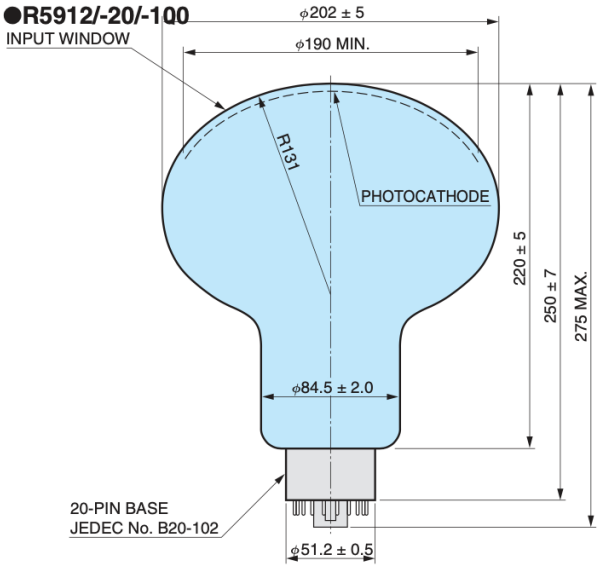

FIGURE 4.4. PMT R5912 drawing [72]

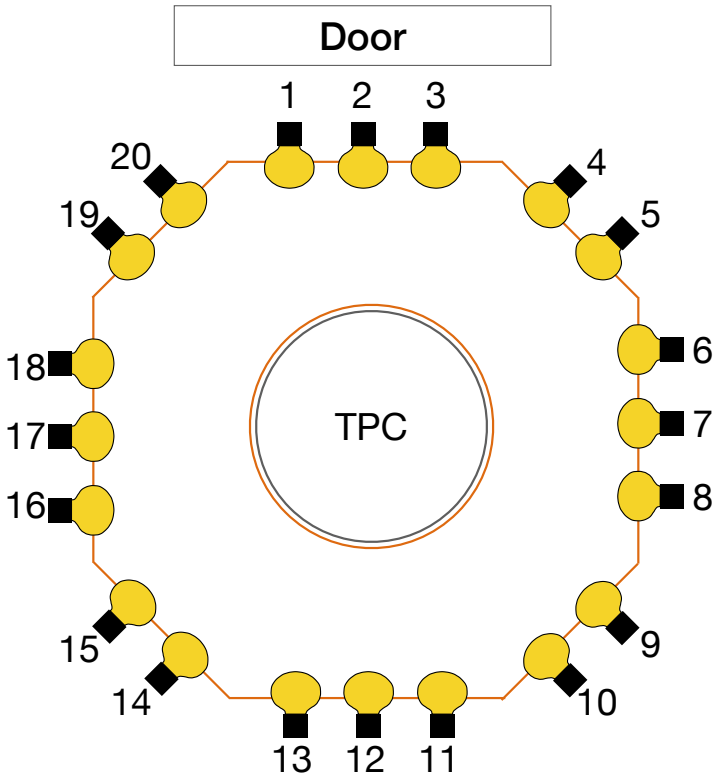

FIGURE 4.5. nVeto top view to show the arrangement of PMT column IDs.

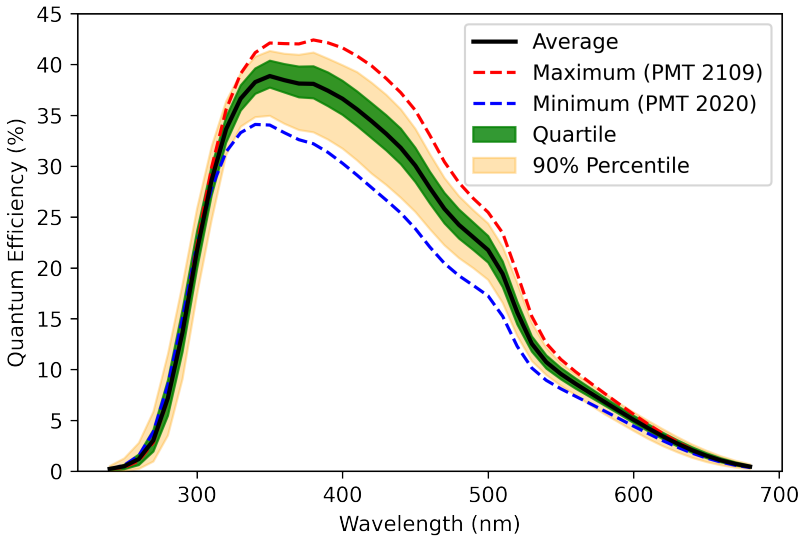

FIGURE 4.6. Q.E. of nVeto PMTs. The black line shows average efficiency for all nVeto PMTs. The green and orange-filled areas show quartile and 90% percentile regions, respectively. The dotted lines show the maximum and minimum examples.

approximately 100 V to dynode. In the case of measuring Q.E. in the range of 200 to 1200 nm, the light incident on the PMT is spread out to some extent. The size of the incident light is adjusted by moving the PMT to be measured back and forth in the instrument. The incident light size is adjusted to the effective diameter of the PMT (Φ190 mm). The PMT Collection Efficiency (C.E.) has not been included. The PMTs were arranged randomly in terms of their performances so as not to bias the properties of the nVeto detector.

4.1.3 Data acquisition system

The DAQ of nVeto was built in a similar manner as the one for the TPC. The waveforms are digitized by eight flash ADC boards, V1730 supplied by CAEN S.p.A [73] mounted on a VME crate. The sampling rate is 500 MS/s and the dynamic range is 2.0 V with a 14 bits resolution. The synchronized clock is connected to all boards using a daisy chain. Eight V1730 boards, providing a total of 128 readout channels, are daisy-chained via their onboard optical links driven by a CAEN A3818 PCIe board lodged in a Fujitsu server RX2540 M4, which is in charge of the nVeto DAQ server. The PMTs are positively biased by CAEN SY4527/A7435SP HV power suppliers (+3.5kV, 3.5mA, SHV Conn. and a common floating HV return). Considering given PMT signal duration, which is about 15 ns, and the measured dark rate (about 2 kHz per PMT) data throughput is estimated to be about 40 MB/s for a time acquisition window of 150 ns. The system can cope with the data throughput by using one link (out of 4) of the A3818, capable of supporting up to 90 MB/s. The fast solid state

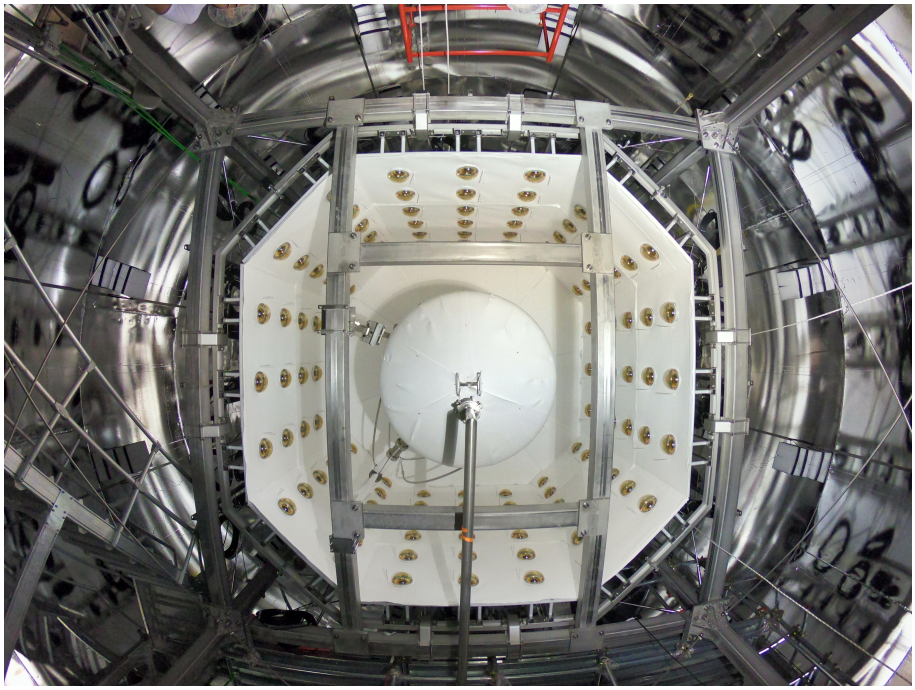

FIGURE 4.7. Picture of the inside of the nVeto detector. The nVeto detector surface is covered with reflective material (white). The picture was taken during construction, finally, the nVeto detector is entirely wrapped with the reflective material.

disk of the Fujitsu server can easily support that data rate as well. The PMT signals are reconstructed with offline software. The nVeto will use the same infrastructure as the TPC for data processing. The processing software is based on strax/straxen, but the nVeto uses its own plugin for its specific analysis. The largest difference compared to the TPC analysis chain is that the neutron veto processing chain is not deadtime-free. We apply a software trigger to the data by taking coincidences among the PMT signals. This is needed to reduce noise events because of the high dark counting rate of the PMTs. The trigger condition is 3 hits above 15 ADC counts within 300 ns, which was obtained in the toy simulation study. Pre-trigger data is not deleted directly, but kept them 1 day for a case when we receive a SNEWS alert.

4.1.4 Reflective material

The inner surface of nVeto except for PMT areas and the outer surface of the TPC are covered with a reflective material to improve the light collection efficiency. Figure 4.7 shows the inside of the nVeto from the bottom side of the detector. The reflective material is 1 mm thick expanded ePTFE. The ePTFE is a chemically stable porous material with a microstructure, and it is known to diffuse ultraviolet light with high reflectivity (more than 99%) with 1 mm thinkness. The reflectivity in the water was measured in an independent setup described in Section 4.4.

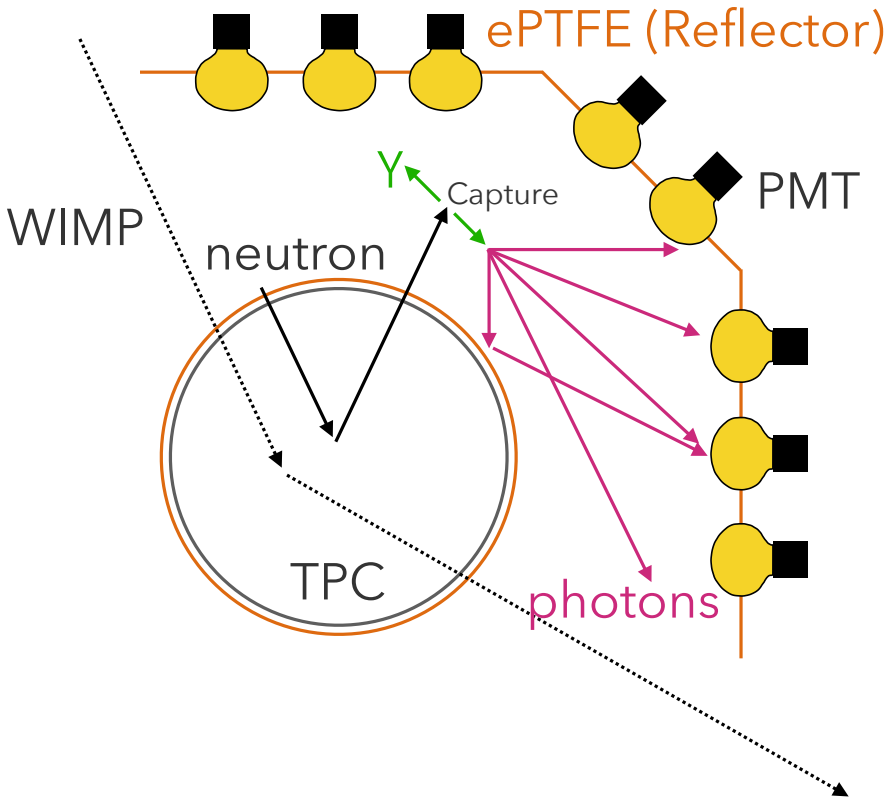

FIGURE 4.8. Top view of the detector illustrating the nVeto detection principle. WIMPs (black dotted line) passes through the XENONnT detector after scattering in TPC, but most of the neutrons are captured by hydrogen or gadolinium nuclei in the nVeto detector. These nuclei produce γ-rays (green) then electrons are produced by photoelectric effect or Compton scattering. The electrons make Cherenkov light and the photons (pink) are detected by the PMT of the nVeto detector. The reflective material, ePTFE, is used on the outer surface of the TPC and the inner surface of the nVeto detector to increase the detection efficiency of the photons.

4.2 Neutron Veto principle

The nVeto detector is an octagonal water Cherenkov detector with a diameter of 10 m and a height of 10 m surrounding the TPC. Figure 4.8 shows the detection principle of neutron background events with the nVeto detector. In the nVeto detector, neutrons are captured by hydrogen or gadolinium, then γ-rays are emitted through an (n, γ) reaction. These γ-rays emit electrons with energies of several MeV by photoelectric effect and Compton scattering. Cherenkov light is emitted when a charged particle passes through an insulating dielectric with a velocity exceeding the phase speed of light, c. In the nVeto detector, this charged particle is an electron and the dielectric is (Gd-)water. With the velocity of the electron v and

the refractive index of the water n, the threshold speed of the electron to emit Cherenkov light is

$$\beta = \frac{v}{c} \geq \frac{1}{n}. \tag{4.1}$$

Using the mass and the energy of the electron m_e and E, β is

$$\beta = \left[1 - \left(\frac{1}{E/m_e + 1}\right)^2\right]^{\frac{1}{2}}. \tag{4.2}$$

In the nVeto detector, $n = 1.332$, which gives the threshold energy of 263 keV.

The emission time of the Cherenkov light is less than 1 ns. Cherenkov light is directional, and its emission angle θ is expressed by the following equation.

$$\cos\theta = \frac{1}{n\beta}. \tag{4.3}$$

In the nVeto detector, the walls are covered with the ePTFE to improve the light collection efficiency. The ePTFE diffuses the light, thus it is difficult to use the angle information for position reconstruction like Super-Kamiokande experiment.

4.3 Analysis framework

For the nVeto data processing, strax and straxen analysis framework are used like the TPC data processing. Figure 4.9 shows the analysis streaming scheme for the nVeto. The raw waveforms are stored with the data type 'raw_records_nv' instead of 'raw_records' for TPC processing. Unlike the TPC analysis, 'raw_records_coin_nv' is computed next, to reduce the data size. The nVeto PMT dark rate is $\sim$ 2 kHz each. The dead-time free DAQ stores even the single dark noise in each PMT. However, these noise events are not useful for the nVeto. To save the capacity of the storage, these pulses are dropped with a data-processing in 'raw_records_coin_nv' using a coincidence level (as a default, 3) within a coincidence window (default 600 ns).

Then, 'records_nv' is computed. This data type has waveforms of subtracted baseline. For an ordinary dark matter run, this 'records_nv' is saved as the lowest level data type in the storage.

The 'hitlets_nv' is a data type to characterize each pulse for 'hits'. The 'hits' is a small pulse above a threshold with some neighborhood bins. In the nVeto analysis, it often means a detected signal of one photoelectron. Table 4.2 shows the variables to characterize the pulse, including 'hitlets_nv'. Variables of particular importance are 'area' and 'amplitude'. The 'area' is a total charge of the pulse with the unit of Photo-Electrons (PE). PMT gains are monitored with Light Emitting Diode (LED) calibrations described below. The 'area' is treated as the number of detected photons in the high-level analysis. The 'amplitude' is the maximum pulse height above baseline. It is not used as often as the 'area'. Unlike the TPC

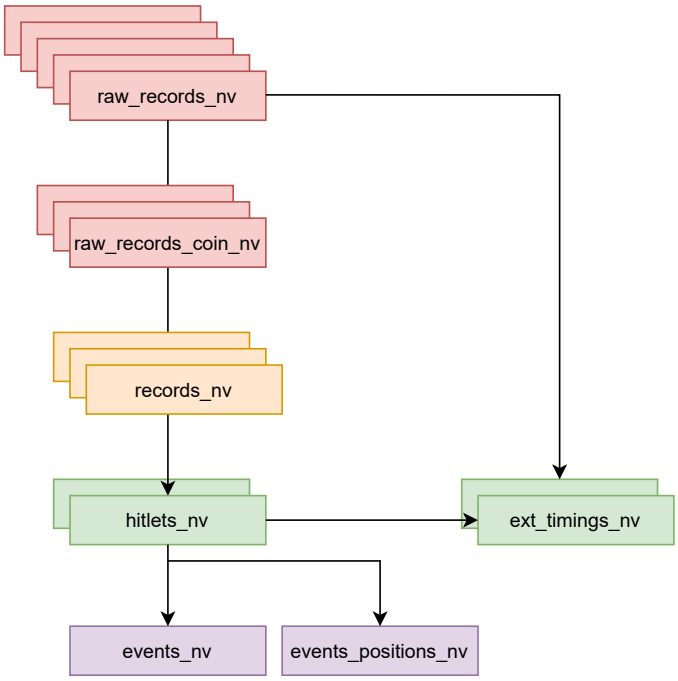

FIGURE 4.9. Analysis flow for the nVeto. The boxes show the data type and arrows show their dependencies. These colors show the data kind.

TABLE 4.2. Variables characterizing each pulse defined in data type, 'hitlets_nv'

Variable name	Type	Description
time	int64	Start time since unix epoch [ns]
length	int32	Length of the interval in samples
dt	int16	Width of one sample [ns]
channel	int16	Channel/PMT number
area	float32	Total hit area in PE
amplitude	float32	Maximum of the PMT pulse in pe/sample
time_amplitude	int16	Position of the Amplitude in ns (minus time)
left_area	float32	Position of the 25% area decile [ns]
low_left_area	float32	Position of the 10% area decile [ns]
range_hdr_50p_area	float32	Width of the highest density region covering a 50% area
range_hdr_80p_area	float32	Width of the highest density region covering a 80% area
left_hdr	float32	Left edge of the 50% highest density region [ns]
low_left_hdr	float32	Left edge of the 80% highest density region [ns]
fwhm	float32	FWHM of the PMT pulse [ns]
left	float32	Left edge of the FWHM [ns] (minus time)
fwtm	float32	FWTM of the PMT pulse [ns]
low_left	float32	Left edge of the FWTM [ns] (minus time)

TABLE 4.3. Variables defined in events_nv' and 'events_positions_nv'

Variable name	Type	Description
time	int64	Start time since unix epoch [ns]
endtime	int64	Exclusive end time since unix epoch [ns]
event_number_nv	int64	Veto event number in this dataset
area	float32	Total area of all hitlets in event [pe]
n_hits	int32	Total number of hitlets in events
n_contributing_pmt	uint8	Total number of contributing channels
area_per_channel	('<f4', (120,))	Area in event per channel [pe]
center_time	float32	Area weighted mean time [ns]
center_time_spread	float32	Weighted variance of time [ns]
pos_x	float32	Area weighted mean of position in x [mm]
pos_y	float32	Area weighted mean of position in y [mm]
pos_z	float32	Area weighted mean of position in z [mm]
pos_x_spread	float32	Weighted variance of position in x [mm]
pos_y_spread	float32	Weighted variance of position in y [mm]
pos_z_spread	float32	Weighted variance of position in z [mm]
angle	float32	Azimuthal angle of neutron capture [0, 2π).

analysis process, nVeto target is only the Cherenkov signal thus the nVeto analysis process is simpler. The 'events_nv' and 'events_positions_nv' are data types to reconstruct events to collect hits in a certain time window. In other words, this event data kind defines a time boundary and counts the hits in the region. The variables are summarized in Table 4.3 The 'area' is the sum of the 'area' of the 'hitlets_nv' with the unit of PE. The 'n_hits' is the number of the 'hitlets_nv'. In the nVeto detector , almost all hits are single photoelectron signals. There is a strong correlation between 'area' and 'n_hits', and in most cases 'area' $\sim$ 'n_hits'.

The 'n_contributing_pmt' is a number of PMTs constructing the event. This variable helps to remove the events in which only one PMT has a large signal. The absolute value of the time is stored in 'time' and 'endtime', and the relative value of the time in the event is stored in 'center_time'. In other words, the emission center of nVeto in an event is expressed absolutely as events_nv['time'] + events_nv['center_time'] with Unix time.

We use these events and variables to define the neutron events to veto TPC neutron events. First, we select neutron tagged event. Here, we apply selections to exclude the accidental dark events of PMTs (e.g., n_hits> 5, etc.). Then, we optimize the time width of nVeto and veto the TPC events within the time width. By loosening the cut to select events for the nVeto, the neutron tagging efficiency is increased, while the livetime of the TPC is decreased. The same trend can be observed by increasing the time width of nVeto. These conditions need to be optimized by data–driven analysis and simulation.

For external triggered runs, i.e., optical calibration, an additional data type 'ext_timings_nv' is calculated. 'raw_records_nv' is removed after processing but required to find the trigger timings. This data type stores the time difference from the trigger timings to the hits. This

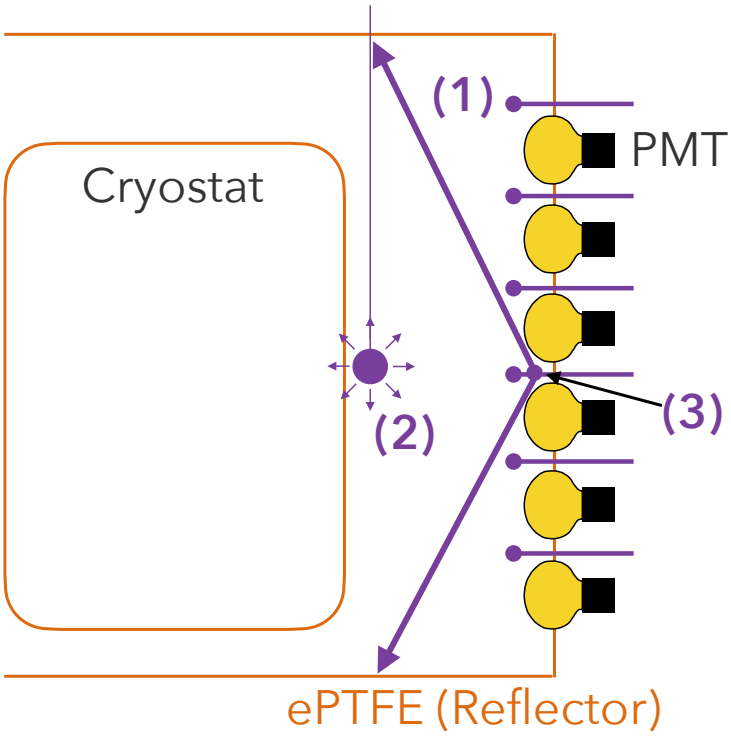

FIGURE 4.10. Positions of three types of nVeto optical calibration devices, (1) LED, (2) laser, and (3) reflectivity monitor in the side view of the nVeto detector. The LED is used to collect SPE signals. The laser calibrates the PMT timings. The reflectivity monitor is used to calibrate the optical behavior in the nVeto detector.

process is performed online. The 'raw_records_nv' and 'records_nv' are not required for timing analysis with optical devices.

4.4 Optical calibrations

For optical calibrations of the nVeto detector, three types of devices, namely LED, and laser reflectivity monitor were installed.

The optical fiber called "LED" is placed at the side of each PMT. The main purpose of it is a collection of single photoelectron signals to evaluate PMT gains. Figure 4.11 shows typical Single PhotoElectorn (SPE) waveforms obtained from the LED calibration. The obtained SPE distribution is used to monitor the PMT gains during a run.

Teflon diffuser balls called "laser" illuminated by laser light were also installed. The laser calibration is used to adjust the timing for each PMT. Each PMT has a bit different transit time and the digitizer has also a timing offset. Four Teflon diffuser balls were placed close to

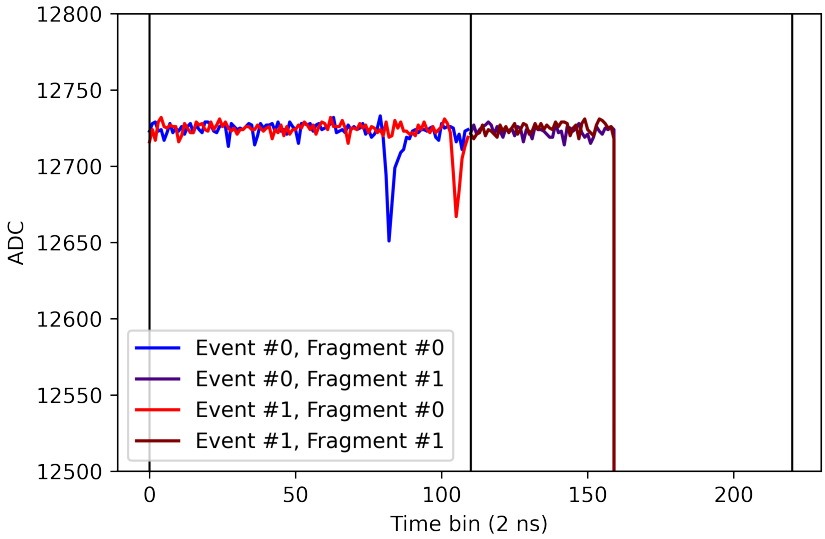

FIGURE 4.11. Typical Single photoelectron pulses obtained with the LED calibration.

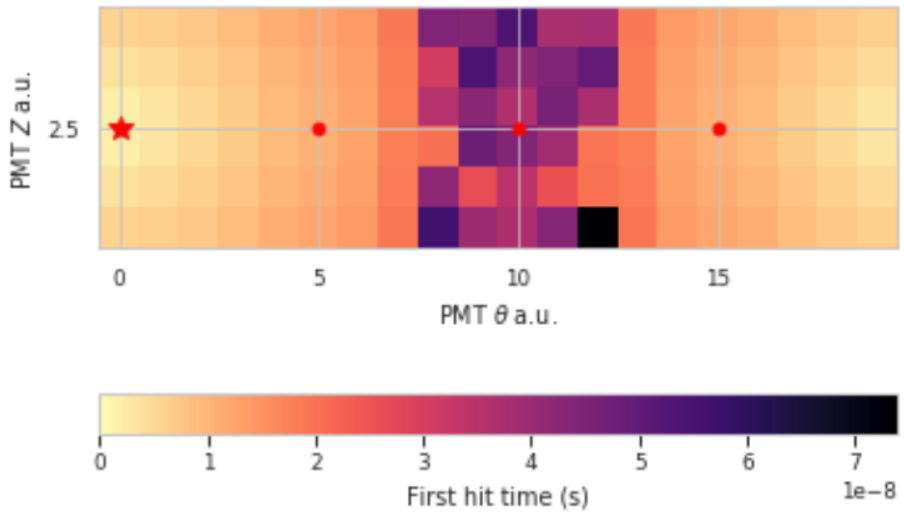

FIGURE 4.12. Timing offsets for a laser calibration in simulation.

the TPC, center of the nVeto detector. Using the photons which directly enter into each PMT, the photon reaching timings are obtained. The correct timing difference which comes from the difference of the light path is obtained Monte-Carlo simulation described in Chapter 5. Figure 4.12 shows the expected timings for diffuser balls with a simulation. To achieve this result, we add a time offset for each channel to correct the timing.

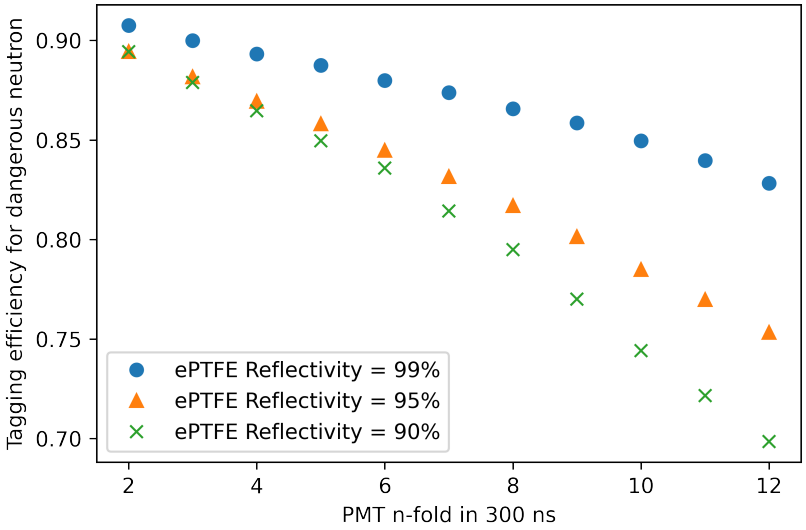

FIGURE 4.13. Evaluated nVeto tagging efficiency with a preliminary simulation without PMT waveform in each assumption of ePTFE reflectivity. When 10-fold PMT coincidence is used to veto event, the evaluated tagging efficiency decreases 85% to 78% if the reflectivity decreases 99% to 95%

The most frequently used optical calibration device for nVeto detectors is the reflectivity monitor. The reflective material and water absorption length affect the neutron tagging efficiency. Figure 4.13 shows the dependence of the nVeto neutron tagging efficiency on the ePTFE reflectivity with a simple preliminary simulation with Geant4 application and PMT Q.E. without the consideration of PMT waveforms and later analysis process. In the worst case, physical and chemical change of the ePTFE may occur, and the reflectivity may decrease during the experiment. The target water is sampled time-to-time to measure the absorption length. The ePTFE reflectivity should be monitored without opening the tank during the measurement. Four optical lasers have been prepared to monitor reflectivity. Two lasers of the reflectivity monitor point upper and the others do lower. The drawing of the laser head of the reflectivity monitor is shown in Figure 4.14. The optical fiber is housed in a stainless steel tube to prevent flooding. If the fiber is flooded in water, the light intensity may decrease due to capillary action between the core and the clad of the fiber. A picture of the installed laser head of the reflectivity monitor is shown in Figure 4.15. The laser wavelength of the reflectivity monitor is set to 375 nm for effective ones considering the spectrum of the Cherenkov light and nVeto PMT Q.E. (Figure 4.16).

The reflectivity monitor is used to validate the entire optical model of the nVeto detector. The lasers emit photons to the ePTFE wall and the ePTFE diffuses the photons. The photons are reflected on the nVeto wall many times, pass through the nVeto until they are detected by PMT, absorbed in water, or absorbed by the ePTFE. Thus, the photon arrival time after emission of the laser indicates the probability of the loss of the photons. The timings are

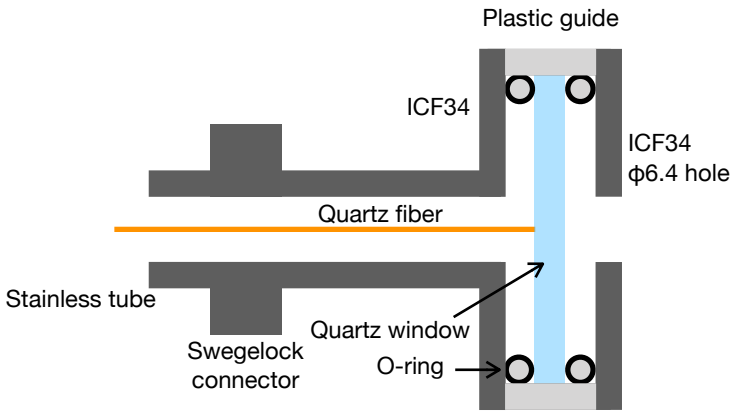

FIGURE 4.14. Mechanical drawing of the reflectivity monitor laser head.

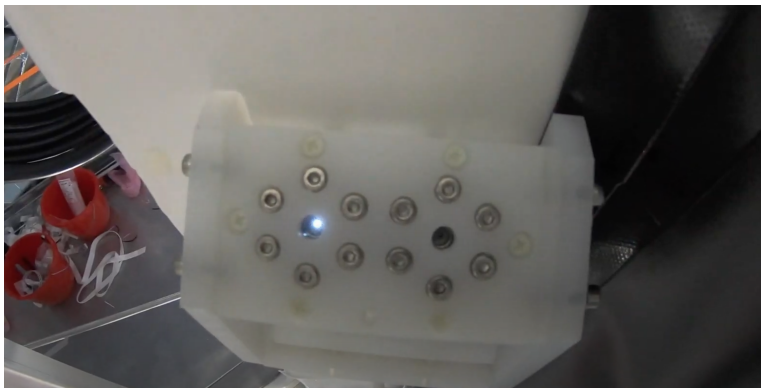

FIGURE 4.15. Installed laser head of the reflectivity monitor. The fibers are checked with a handy light source during the construction.

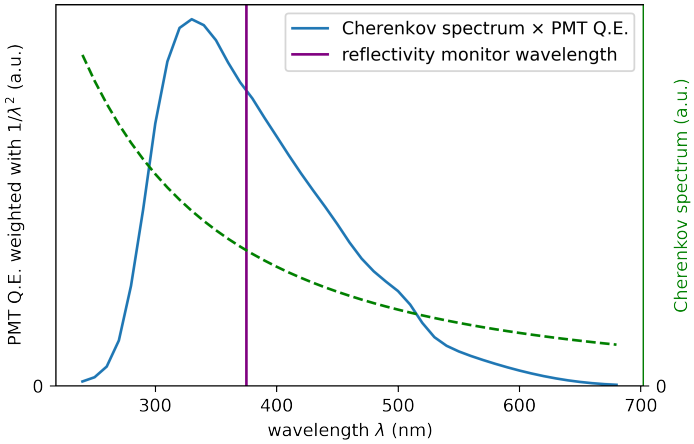

FIGURE 4.16. Effective wavelength of PMT and the reflectivity monitor laser.

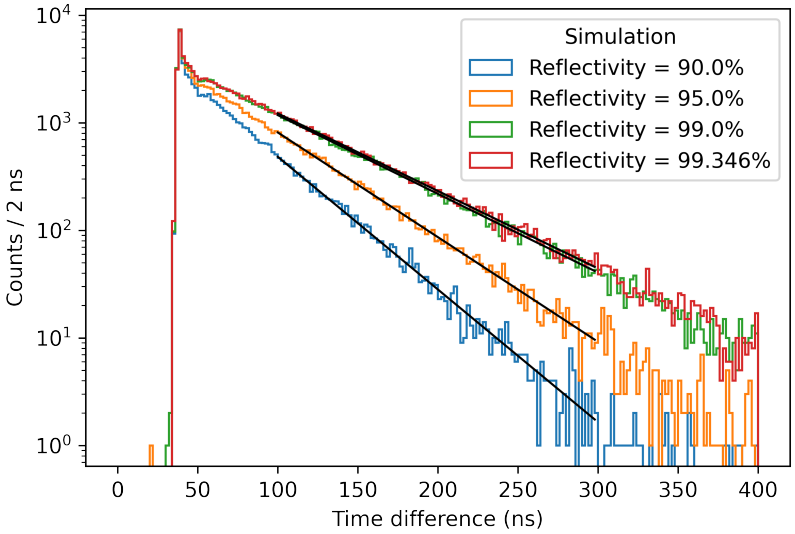

FIGURE 4.17. Simulated timing distributions with reflectivity monitor. The time slopes are coupled to the nVeto ePTFE reflectivity implemented.

observed as a result of the influence of the PMT surface optical properties, water transparency, and ePTFE reflectivity. The results cannot be expanded for each effect. The optical properties of PMT are known [74, 75]. The last unknown parameter is the reflectivity of the ePTFE. Finally, the reflectivity can be extracted from the distribution of the photon arrival timing. These optical effects are calibrated with a parameter, the ePTFE reflectivity. Figure 4.17 shows these distributions of each ePTFE reflectivity with known PMT parameters and ideal water transparency (Figure 4.2). The ePTFE reflectivity is clearly observed in the slope.

Measured calibration results of the photon arrival timing are shown in Figure 4.18. All PMTs detect the timing distributions with the same slopes. The distributions of the data and simulations are obtained with the same algorithm, thus they can be compared directly. Both distributions are fitted with an exponential function taking time constants as a fitting parameter. Here, the cost function is an unbinned likelihood function, the time constants are evaluated. The observed time constant in the calibration data is $60.13 \pm 0.08_{(\mathrm{stat.})}$ ns. This value is equivalent to 99.3% reflectivity in Figure 4.19 The time constant is also affected by uncertainties of the PMT properties and the water transparency. However, the simulation parameters which reproduce the slope are enough to evaluate the nVeto neutron tagging efficiency as an effective behavior because the new simulation is validated with the data-driven calibration. In other words, the ePTFE reflectivity is an effective parameter to describe the photon survival probability in the nVeto detector, including other reflections and absorptions.

In addition, in a preliminary measurement at Kobe University [76] called 'Mini bucket test', the ePTFE reflectivity in the water was measured independently. The measurement is described in Appendix A. As a result, the reflectivity of ePTFE was determined to be

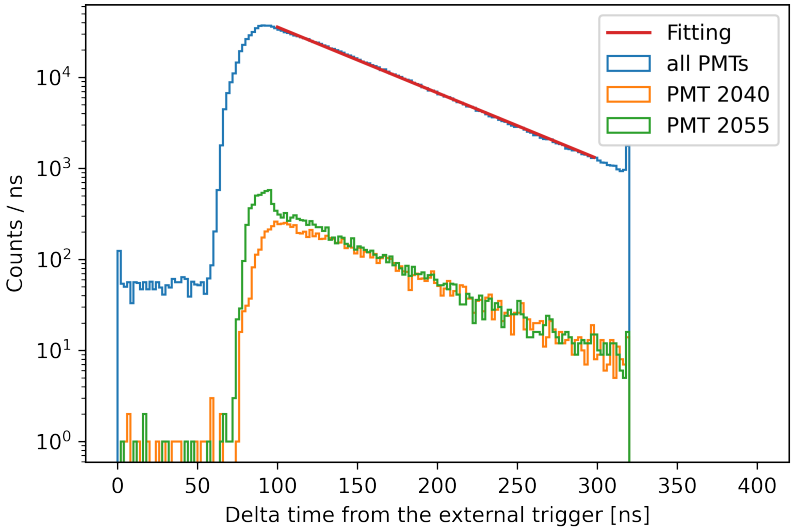

FIGURE 4.18. Observed photon arrival timing distributions. The distributions are fitted with exponential functions.

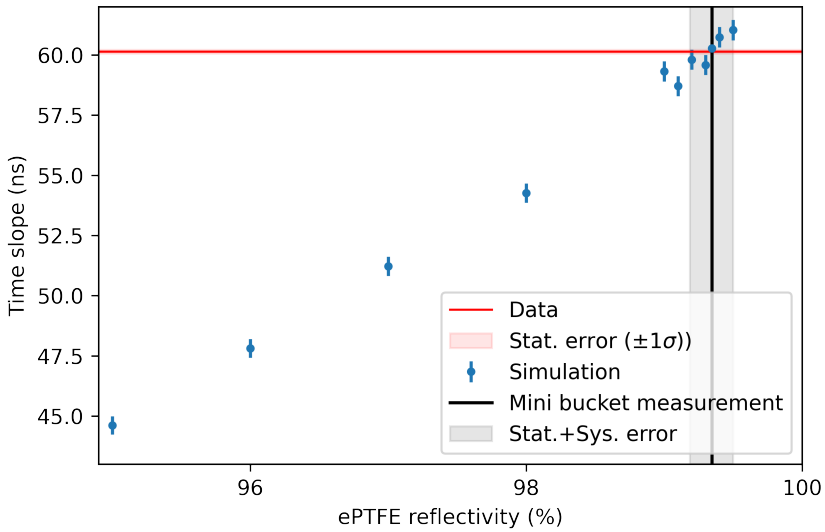

FIGURE 4.19. Time constants of the slope reproduced in the simulation with each reflectivity of the ePTFE (blue). The red line shows the observed time constant by the calibration. The black line is obtained by independent ePTFE reflectivity measurement with a mini bucket.

$99.346 \pm 0.004(\text{stat.})^{+0.149}_{-0.156}(\text{syst.})\%$. This result is in good agreement with the calibration result shown in Figure 4.19.

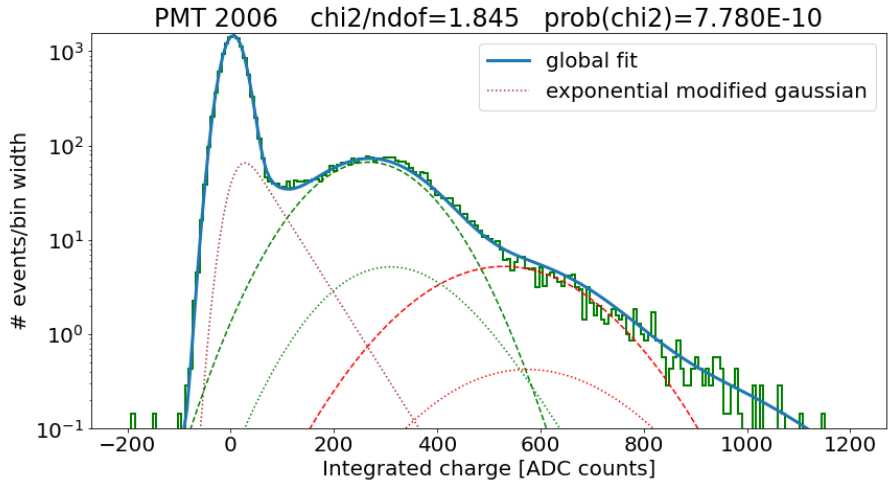

FIGURE 4.20. Typical pedestal and single photoelectron spectrum.

4.5 Commissioning data

A commissioning run of 94 days (DAQ livetime) was carried out under the same conditions as the dark matter search. The data were taken in linked-mode DAQ with TPC and muon Veto detector.

In the commissioning run, the nVeto detector was filled with pure water without gadolinium dissolved. Therefore, the main target for the neutron capture during the commissioning run is hydrogen in pure water. Hydrogen captures neutrons and emits Cherenkov light and the cross section is 0.3326 barn for thermal neutron [77]. The Q-value is 2.2 MeV [78].

Optical calibrations were carried out every week during this period. These calibrations were performed in an unlinked mode DAQ. First, PMT gains and SPE distributions were observed with LED calibration described in Section 4.4. Figure 4.20 shows a typical spectrum of integrated charge with the unit of PE for LED calibration data. The spectra were fitted with exponential modified function and Gaussian functions. The differences of the means of the Gaussian distributions, which are the peaks of the pedestal and single photoelectron, are calculated as the gains for all PMTs. Figure 4.21 shows the typical gains of PMTs during the commissioning run. The gains of any PMTs were stable within 5%. The observed gain map is used for conversion from ADC$\times$sample to PE in the 'hitlets_nv' level data.

The pedestal data has been collected with the external trigger during the commissioning run. Figure 4.22 shows the obtained baselines in the pedestal run. The baseline level is adjusted around 12700 ADC with the digitizer configurations. The projection of the nVeto baseline spreads is shown in Figure 4.23. Considering that the typical SPE pulse height is approximately 70 ADC and the nVeto DAQ threshold is 15 ADC, the noise level is quite calm. The noise effect is not much affected for the analysis, but we consider the noise effect in the simulation described in Chapter 5.

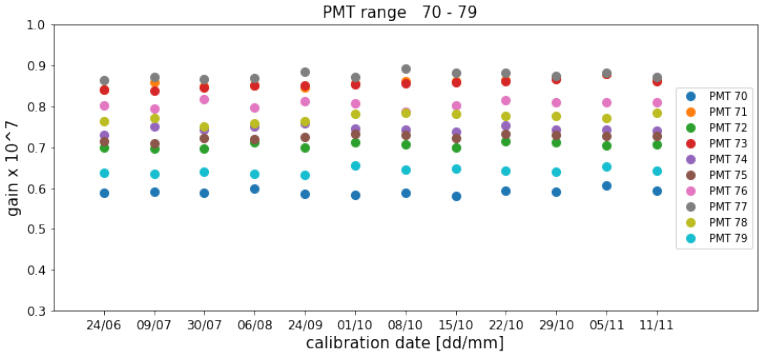

FIGURE 4.21. PMT gains observed in weekly calibrations.

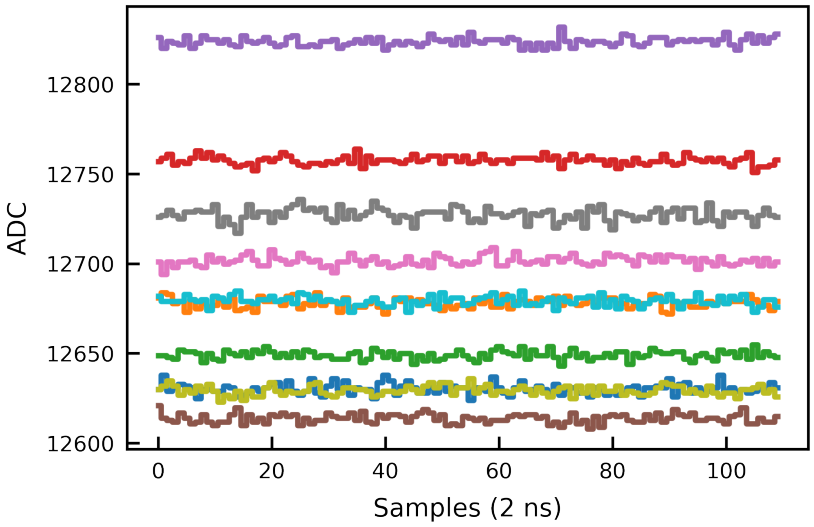

FIGURE 4.22. Typical baseline noises of nVeto PMTs.

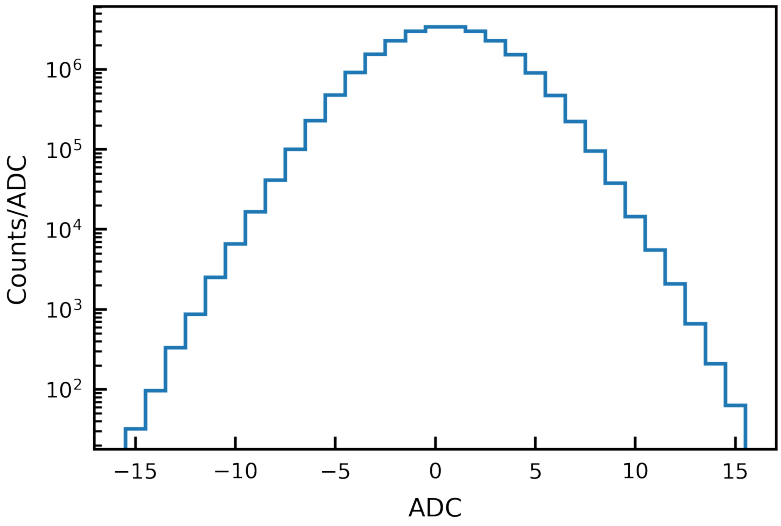

FIGURE 4.23. Projection of nVeto Baseline noises. Fifteen ADC counts are a threshold to record the waveform.

CHAPTER 5

Simulation

In this chapter, simulation for the XENONnT experiment is described.

5.1 Simulation Framework

Simulation for the XENONnT experiment is constructed with several software tools called mc, EPIX, and WFSim. Figure 5.1 shows the simulation flow. The purpose of the chain of simulations tools is to simulate background and calibration events with the data-like format

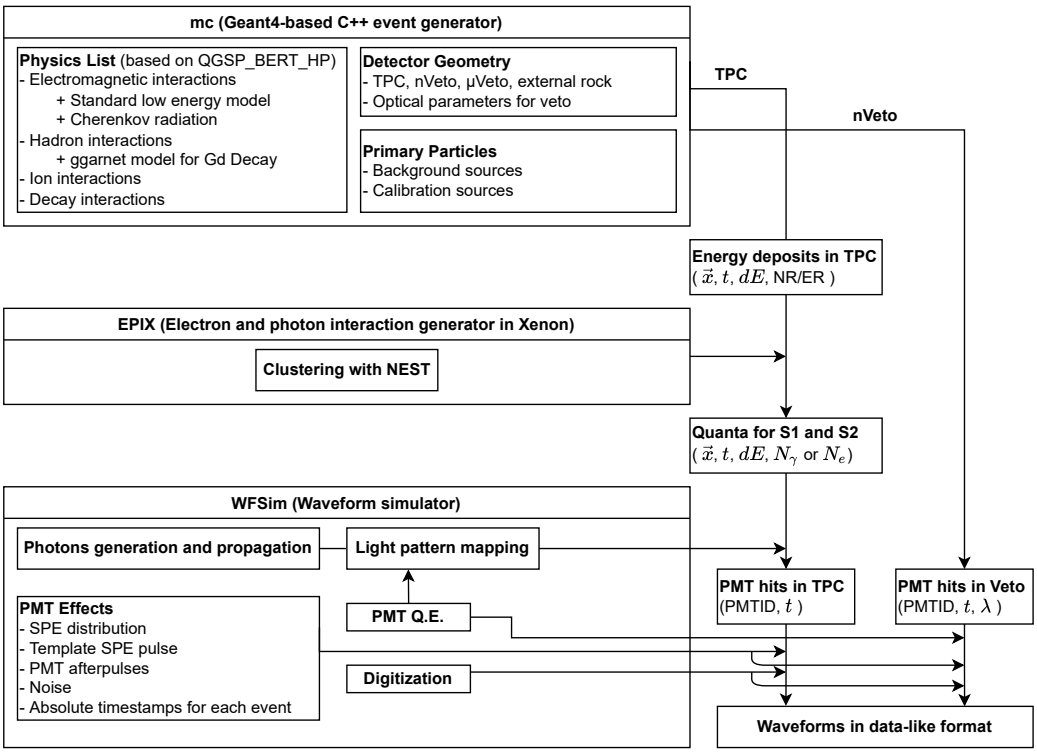

FIGURE 5.1. XENONnT experiment simulation flow.

to evaluate the sensitivity for WIMPs and other physics targets. The output includes the waveform data that can be processed by exactly the same analysis as the real data.

5.1.1 Geant4 application

The starting application is called mc, Geant4 (Version 10.6-patch3)-based event generator written in C++. Geant4 is a toolkit for the simulation of the passage of particles through matter with the Monte-Carlo method [79, 80, 81]. Geant4 requires at least three inputs by the user: physics list, detector geometry, and primary particles. This application stores the energy deposits in the xenon TPC and photon hits in the nVeto PMTs. The primary particles are described in Section 5.2.

5.1.1.1 Physics list

Physics List is an object of physical interactions implemented in Geant4. The physics list contains a list of particles to be simulated and models of interactions applied to the particles. The interaction of particles in a material is called 'Process', and it is constructed as a class based on the knowledge accumulated in the fields of particle physics, nuclear physics, atomic physics, and so on. It can also be implemented by the users. Each physical process is classified into five types: electromagnetic interaction, hadronic interaction, optical photon process, decay process, and parameter representation of the interaction. For a physical process, several different physical models are provided as a 'process', and it is necessary to determine the best combination of the processes according to the user's requirements. Since it is not easy to construct an appropriate physics list avoiding the duplications of processes, a predefined physics list is provided for typical cases, called a reference physics list. Most of the reference physics lists are a combination of processes for different electromagnetic and hadronic interactions and are named <Electromagnetic model>_<Hadronic model>_<Option>.

In the XENONnT experiment, the QGSP_BERT_HP reference physics list with some modifications is used as the default. The QGSP_BERT_HP is one of the stable lists (called Production physics lists) maintained by the Geant4 collaboration specifically for data production in LHC experiments. For electromagnetic interactions, a standard model is used. And the Bertini cascade model ($<\sim$9.9 GeV), the Fritiof model ($\sim$9.9–$\sim$18 GeV), and the QGS model ($>\sim$18 GeV) are used for hadronic processes. In addition, _HP means that the high-precision model is used for neutrons below 20 MeV. For the Veto detector, optical photon physics was added and the Cherenkov reaction process is enabled. The photons were tracked in the nVeto detector with reflections at the ePTFE surface and reached the nVeto PMT surfaces.

The simulation of γ-rays during the de-excitation of gadolinium is very important for the evaluation of the nVeto detectors, but the process (photon evaporation model) provided in the Reference physics list is not appropriate. During de-excitation, gadolinium emits several γ-rays with a total energy of about 8 MeV. The Geant4 default process, photon evaporation model is not fatal in the energy spectrum for each γ-ray but does not take into

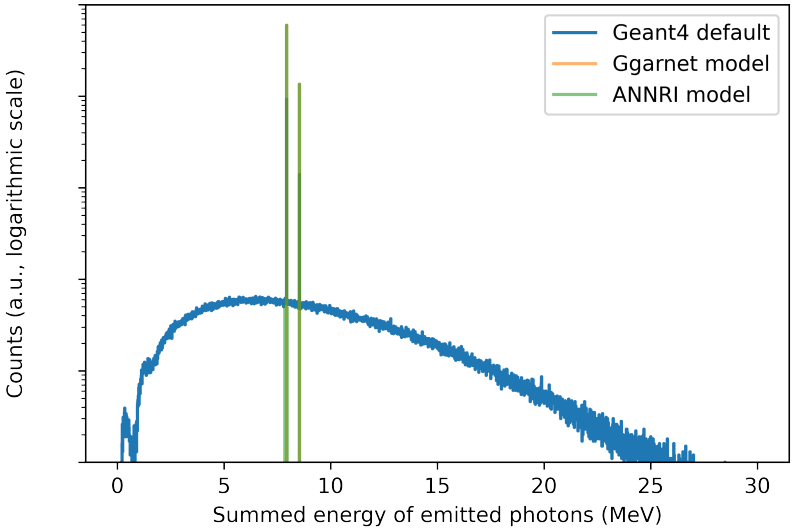

FIGURE 5.2. Summed energy of the emitted photons in Gd de-excitation. The Q-values of ^{157}Gd and ^{155}Gd are 7.9 and 8.5 MeV. The Geant4 default model does not take into account energy conservation. The GGARNET and the ANNRI models are overlapped.

account the energy conservation of total γ-rays. Therefore, we use user-defined ggnarnet and ANNRI models that are not included in Geant4. The models were developed based on data obtained by irradiating gadolinium samples with neutron beam at Materials and Life science experimental Facility (MLF) in J-PARC [82, 83]. Emitted γ-rays from thermal neutron captured were detected by the germanium crystal array of a detector. The models describe the continuous component of the γ-ray energy spectrum and the discrete peaks separately, which are eventually combined to form the overall spectrum. The generated directions are completely random without any angular correlation. The yields of discrete peaks in the model are adjusted to match the measured data. For the continuous spectrum, the Hartree-Fock-Bogliubov method for the nuclear level density and a statistical description based on the photon strength function of the electric dipole, following the enhanced generalized Lorentzian model and the Standard Lorentzian model in GGARNET and ANNRI models, respectively. Both models look similar to each other. GGARNET model is used as a default in the XENONnT simulation.

These models are provided on the web by the collaboration for Geant4 version 9.6. The models have been ported to work with our Geant4 version 10.6. Figure 5.2, 5.3, and 5.4 show the summed energy, each energy, and the number of emitted photons in the de-excitation, respectively. The summed energy is reasonable for Q-values of the nuclei, 7.9 and 8.5 MeV, in both implemented models. For other nuclei, the default photon evaporation model is used.

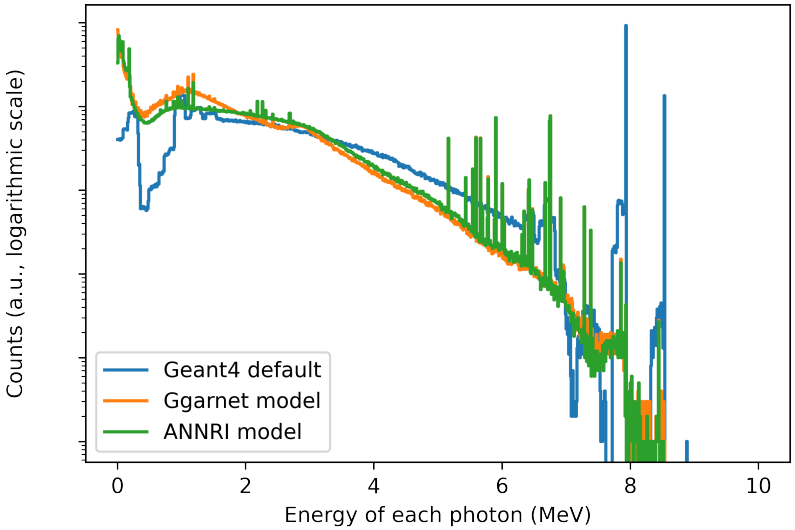

FIGURE 5.3. Energy of each emitted photon in the Gd de-excitation.

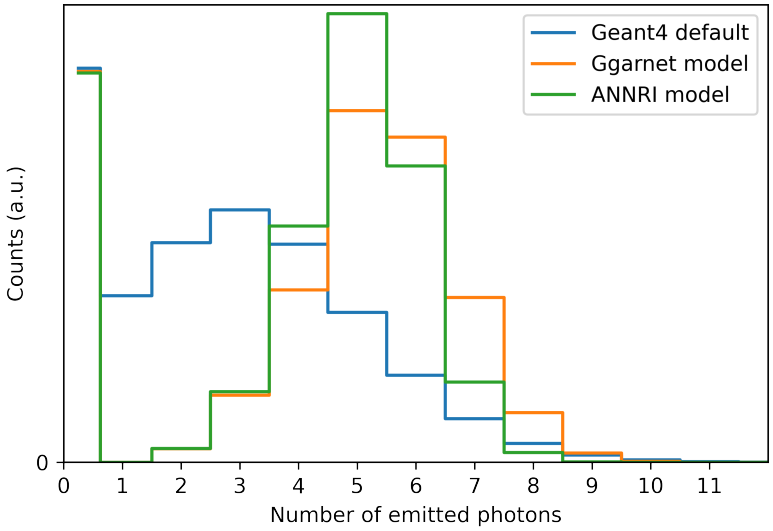

FIGURE 5.4. Number of the emitted photons in the Gd de-excitation.

5.1.1.2 Detector geometry

Another input for Geant4, geometry, which has information on materials and shapes. The geometry of the XENONnT experiment is built by following a CAD file (Figure 5.5). For the nVeto detector, optical parameters have been implemented. For example, the absorption length of the water provided by the Super-Kamiokande experiment was used as an ideal

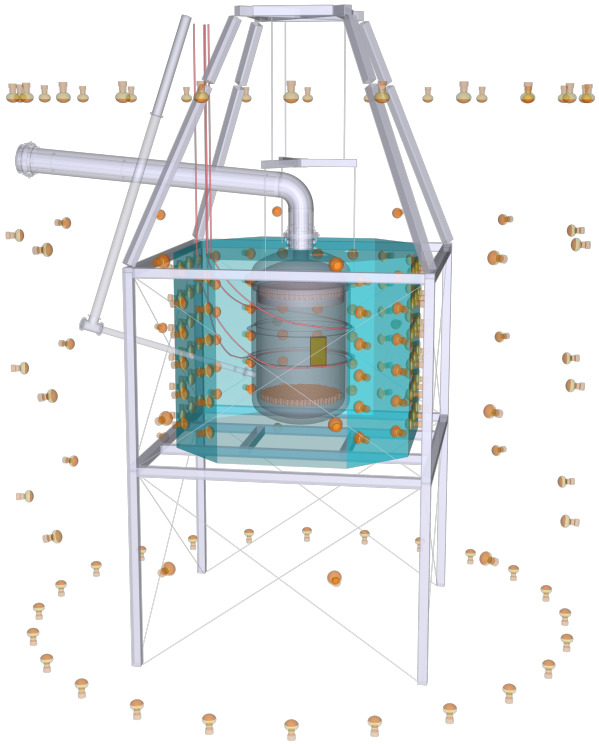

FIGURE 5.5. Detector geometry for the simulation. All components of the detector and wall rock are implemented. For a clear view, some components (water tank, nVeto reflector, etc. are set to be invisible.

case (Figure 5.6). In addition, the ePTFE reflectivity calibrated has also been implemented. The implemented reflectivity is calibrated for this simulation framework with the observed time constant, thus the optical parameters are effective values for data-simulation comparison. For TPC simulation, the optical photons have not been tracked. The signal response is considered on the following model described in Section 5.1.2.

5.1.2 Signal response

In the first stage of the Geant4 application, the energy deposits via ionization and diatomic de-excitation in the TPC are conserved. The quanta, free electrons and photons are evaluated with the established model, the Noble Element Simulation Technique (NEST) [85] and the energy deposits. The NEST is a parameterized model taking into account fluctuations in the scintillation and ionization processes, electron-ion recombination, and drift field dependence. In addition, the Liquid Xenon (LXe) emission model was obtained with high-statistics calibrations in the XENON1T experiment [86]. The photon and electron yields below 1 keV for ER and 3.5 keV for NR are extrapolated based on measurements at higher energies, where zero-emission below 1 keV NR is assumed. TPC parameters used in the simulation are summarized in Table 5.1.

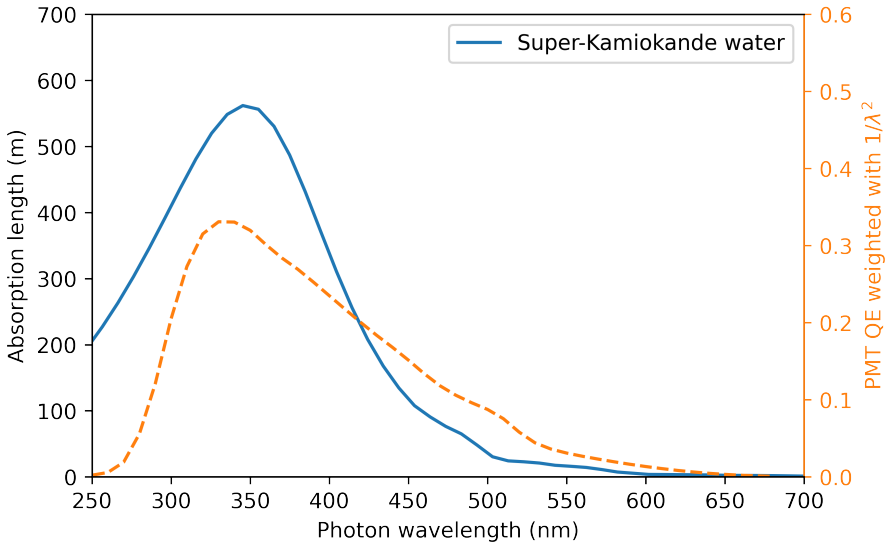

FIGURE 5.6. Inplemented water absorption length (blue) [84]. The effective wavelength of the nVeto detector for Cherenkov light is shown in orange dotted line with the right axis.

The original NEST model is written and provided in C++. NEST model ported into pure-python, called nestpy (https://github.com/NESTCollaboration/nest), is used with a wrapper called EPIX [90]. The EPIX converts the output of Geant4 into the input of the following waveform simulator. The nVeto simulation does not require EPIX because the PMT hits are constructed by direct optical simulation in Geant4.

In this study, the generated quanta, photons and electrons which are the origin of the signals are used for the TPC analysis.

5.1.3 Waveform simulation

Geant4 application, mc, and EPIX generate quanta for TPC and PMT hits for the nVeto. Finally, a waveform simulator namely WFSim [91] is applied. The Waveform simulator outputs the waveforms obtained by each PMT in the format 'raw_records' according to the analysis framework. This format is the same as the one used by DAQ to store the waveforms. Therefore, the analysis chain for the real data can be directly used to compare the data with the simulation. Figure 5.7 shows the concept to generate the pulse from Geant4 output. In the output of Geant4, the timings when a photon arrived at the PMT, the wavelengths of the photons, and the IDs of the arrived PMTs are stored for each event. First, the waveform simulator arranges the events of Geant4 randomly on the time axis according to the assumed rate (purple dots). Then, the timing of each photon is placed on the absolute time axis relative to the time at which the event is placed. Some hits are removed using the Q.E. of the PMT, which depends on the wavelength of the photon. In addition to the Q.E., a collection factor

TPC parameters	Value
Optical parameters	
PTFE-LXe (Gaseous Xe) reflectivity	0.99 (0.99)
LXe absorption length [m]	50
LXe Rayleigh scattering length [cm]	30
LXe (Gaseous Xe) refractive index	1.63 (1)
PMT quartz window refractive index	1.59
Electrodes optical transparency	
Top screen	0.957
Anode	0.956
Gate	0.956
Cathode	0.960
Bottom screen	0.971
Signal generation	
PMT QE	0.34
PMT collection efficiency [87]	0.90
Double photoelectron (PE) probability [88, 89]	0.219
Photon detection probability (g_1) [PE/ph]	0.169
Electron extraction efficiency	0.96
Effective charge gain (g_{2b}) [PE/e^-]	14.3
S1 PMT coincidence level	3
Detector conditions	
Drift field [V/cm]	200
Electron lifetime [µs]	1000

TABLE 5.1. TPC parameters used in the XENONnT detector response model. The average PMT QE at room temperature and the wavelength-dependent optical parameters are given for the xenon scintillation wavelength of 175 nm. Although the purity of the xenon target is expected to be higher thanks to the upgraded purification system, the LXe absorption length is conservatively taken from XENON1T.

calibrated with AmBe source is also taken into account in Section 5.1.4. The collection factor includes an unknown PMT C.E. Second, the template pulse made from the data is placed at each hit timing. The amplitudes of these pulses are scaled according to the SPE distributions. Finally, the real pedestal noise is added to the waveforms.

Figure 5.8 shows the typical SPE pulses observed in the LED calibration and generated with the waveform simulator. The template pulse is created with an average of the collected SPE pulse with the LED calibration. Here if we simply average the measured SPE pulses we obtain a template pulse smeared by the sampling effect of 2 ns. Relatively sharper pulses are selected to compensate for this effect. The scheme and the template pulse should be validated with the real data.

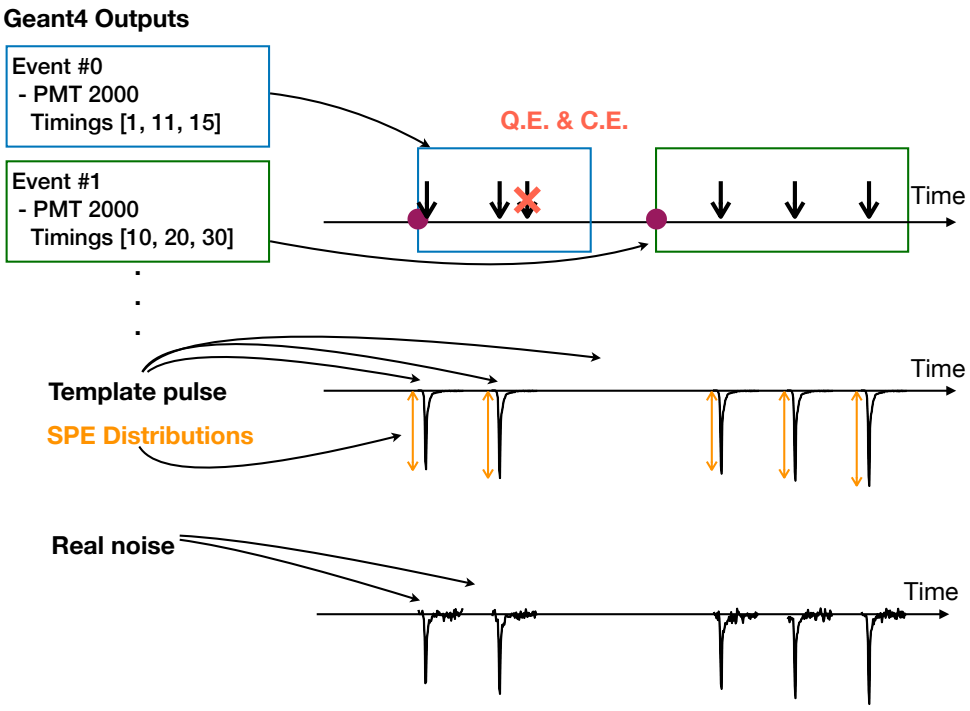

FIGURE 5.7. Concept of waveform simulation.

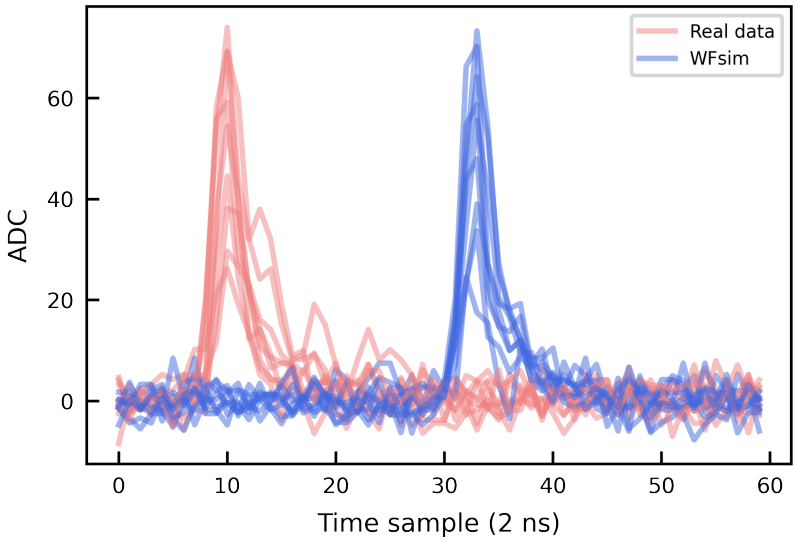

FIGURE 5.8. Typical SPE pulses (light red) and generated pulses with WFSim (light blue).

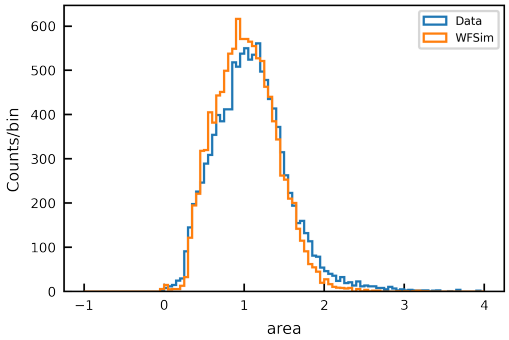

FIGURE 5.9. The 'area' distributions for 'hitlets_nv' of data and WFSim.

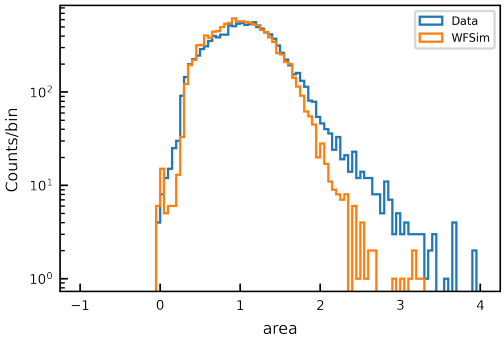

FIGURE 5.10. Figure 5.9 with a logarithmic axis.

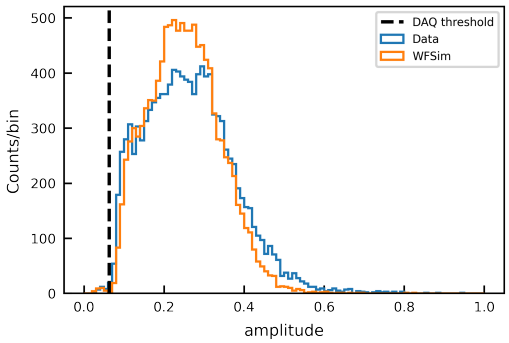

FIGURE 5.11. The 'amplitude' distributions for 'hitlets_nv' of data and WFSim. The dotted black line shows the ADC counts of 15 as a typical DAQ threshold.

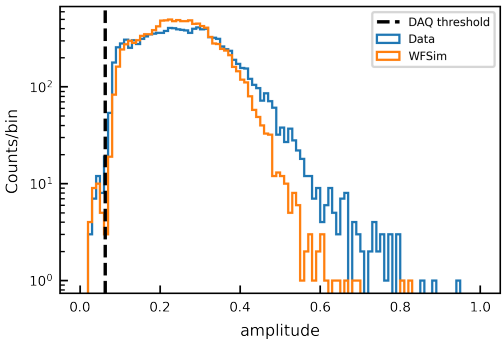

FIGURE 5.12. Figure 5.11 with a logarithmic axis.

Figures 5.9 and 5.10 show the comparison of the distributions of the 'area' for the 'hitlets_nv' in the data and the waveform simulator. The 'area', integrated charge distribution is well reproduced. The small difference around 2–3 comes from that signals of two or more photons are included in the data.

Another typical characteristic parameter is 'amplitude'. The parameter shows the maximum pulse height. Figures 5.11 and 5.12 show the distributions of the amplitude. As shown in Table 4.2, a unit of the 'amplitude' is PE/sample. For the nVeto analysis, the 'amplitude' is used as a threshold at the lowest level analysis. The threshold is 15 ADC counts shown with the black dotted line. The 'amplitude' distribution is well reproduced around the threshold. The rest uncertainties of the shape of the waveforms are considered in Section 6.3.

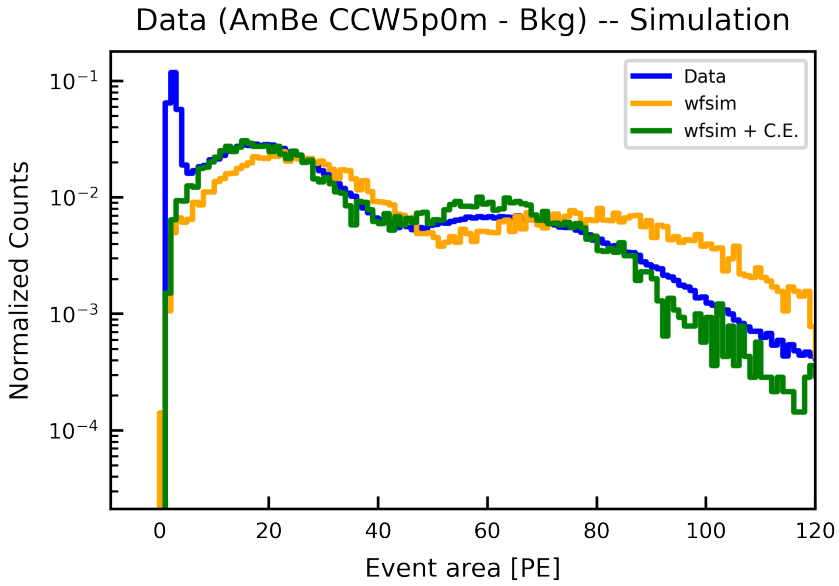

FIGURE 5.13. Data (blue) and simulation (orange) comparison for 'area' of 'events_nv' for AmBe calibration data. Simulation results with a correction factor (green) reproduce the measured one well.

5.1.4 Correction factor from AmBe calibration

The simulation framework and the waveform simulator were validated with measured AmBe calibration data. As the Geant4 primary particles, γ-ray and neutron are generated following Equation 3.4. The neutron capture peak of hydrogen at 2.2 MeV and the prompt emission γ-ray peak at 4.4 MeV are observed for measured data and simulated one in Figure 5.13. In the simulation, the 'area' was found to be overestimated. An additional correction factor, ϵ_{c} was introduced. The correction factor ϵ_{c} includes the PMT C.E. The correction factor was determined by fitting with double Gaussian distributions, 0.7852 to match the 2.2 MeV peaks. That is, the number of the PMT hits (N_{hit}) was corrected from the original number of the hits in Geant4 (N_{G4}) as,

$$N_{\mathrm{hit}} = N_{\mathrm{G4}} \times \epsilon_{\mathrm{Q.E.}}(\mathrm{PMT}, \lambda) \times \epsilon_{\mathrm{c}} \tag{5.1}$$

The $\epsilon_{\mathrm{Q.E.}}(\mathrm{PMT}, \lambda)$ is a PMT quantum efficiency provided by Hamamatsu. The value depends on each PMT and the incident photon wavelength λ distribution is summarized in Figure 4.6. The correction factor ϵ_{c} is an independent value. Applying this value, the simulated distributions of 'n_hits' and 'n_contributing_pmt' were found to reproduce the measured one at the same time (Fugure 5.14 and 5.15). The provided Q.E. doesn't include the collection efficiency thus the ϵ_{c} comes mainly from the PMT C.E. The photon behavior is calibrated with the reflectivity monitor. The correction factor includes the rest unknown effects to lose photons discussed in Chapter 7.

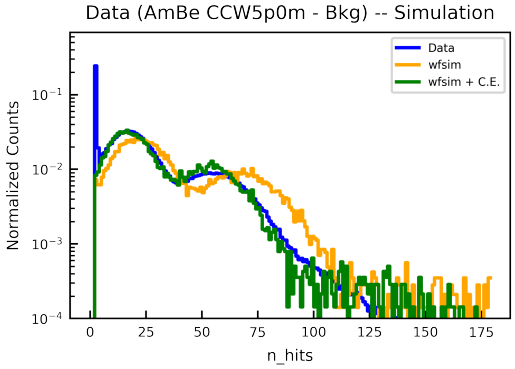

FIGURE 5.14. Data and simulation comparison for 'area' of 'events_nv'.

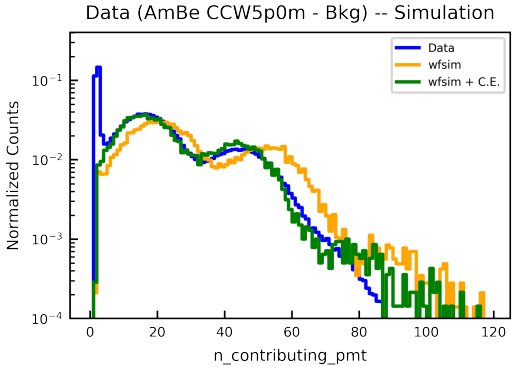

FIGURE 5.15. Data and simulation comparison for 'n_contributing_pmt' of 'events_nv'.

5.2 Backgrounds Evaluation

The XENONnT sensitivity is limited by the background events. Using the simulations, we evaluate the background rates. The background events are ER or NR events in the xenon TPC. The WIMP event is observed as a single NR event because the cross section is small. Therefore, it is important to estimate the background NR events. On the other hand, the ratio of S1 and S2 events and fiducial volume cut is used to discriminate ER events, but some of them are statistically contaminated in the NR. It is necessary to evaluate the ER events quantitatively. For NR events, the Energy Range of Interest (Energy ROI) is used to evaluate the background events within the (4, 50) keV range of the S1 signal. This corresponds to (1, 13) keV for ER events.

As ER background sources, we considered radioactive materials contained in the detector materials, radioactive materials contained in xenon (Xe itself, Rn, Kr), and solar neutrino. Neutrons and coherent elastic neutrino-nucleus scattering (CEνNS) were also considered as NR background sources. These radiation sources were produced as Primary Particles in the simulation, and the total amount was evaluated quantitatively.

5.2.1 Radioassay of detector components

All material used for the XENONnT detector is chosen to be low backgrounds [92] and the radioactivities were measured with a high-purity germanium detector and high-resolution ICP-MS. ^{238}U, ^{235}U, ^{226}Ra, ^{232}Th, ^{228}Th chains and ^{60}Co, ^{40}K, ^{137}Cs are measured. As the primary generators, 28 detector components are used. Table 5.2 summarizes radioactivity levels of the main detector components.

Component	Mass	Activity [mBq/kg]							
	[kg]	^{238}U	^{235}U	^{226}Ra	^{232}Th	^{228}Th	^{60}Co	^{40}K	^{137}Cs
Cryostat vessels	1120	3.2 (9)	0.37 (13)	0.37 (5)	0.29 (7)	0.45 (5)	2.5 (5)	2.1 (3)	< 0.41
Cryostat flanges	730	1.4 (4)	0.06 (2)	< 4	0.21 (6)	4.5 (6)	14.1 (9)	< 5.6	< 1.5
Bell and electrodes	190	3.2 (7)	0.57 (10)	0.62 (10)	0.36 (14)	0.46 (9)	0.78 (11)	1.6 (6)	< 0.17
PTFE	128	0.12 (5)	< 0.06	0.10 (2)	0.11 (5)	< 0.06	< 0.053	2.4 (3)	< 0.038
Copper	355	< 0.69	< 0.28	0.033 (5)	< 0.027	< 0.023	0.11 (2)	< 0.29	< 0.016
PMTs and bases	98	53 (15)	2.2 (7)	4.6 (10)	3.5 (12)	4.2 (8)	7.1 (9)	73 (18)	0.9 (3)

TABLE 5.2. Radioactivity levels of the XENONnT detector components, with uncertainties in parenthesis. Upper limits are given at a 90% confidence level. The activities are averaged by mass over all the individually simulated sub-components.

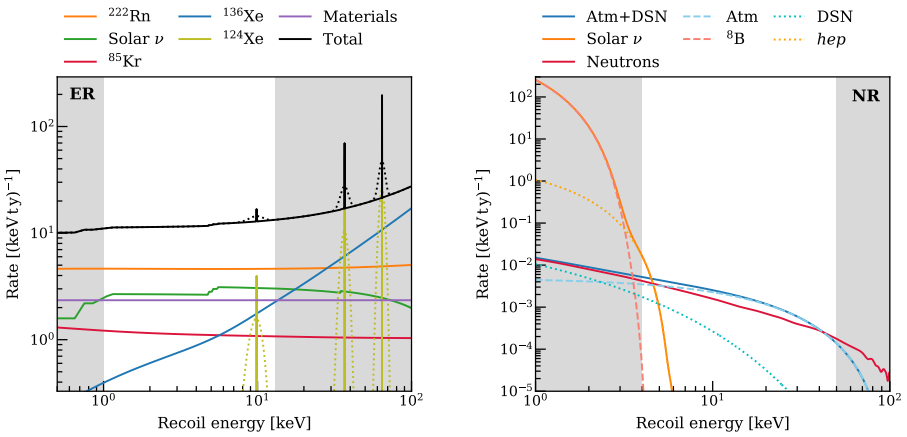

FIGURE 5.16. Energy spectra of the ER backgrounds. The white background area shows the energy ROI (1, 13) keV and (4, 50) keV for ER and NR events respectively.

5.2.2 ER Backgrounds

γ-rays emitted from radiation sources are observed especially as a low-energy background event with single Compton scattering. The detector material uniformly produces γ-rays as a background event source. The left plot in Figure 5.16 shows the energy spectra of ER backgrounds in the 4 t fiducial volume of the XENONnT TPC. The amounts of the material backgrounds are evaluated for each material summarized in Table 5.2. The Compton scattering of the material radiogenic background distribution is flat at less than 200 keV region. The rate is 2.1 (keV t y)$^{-1}$ at the 4t fiducial volume. The dominant background sources are PMT (51%) and Cryostat (41%).

^{222}Rn was the main ER background in the XENON1T experiment. Radon is a noble gas and is contaminated in liquid xenon. ^{222}Rn decays with a half-life of 3.8 days and produces radioactive nuclei of the uranium series in the entire xenon TPC by successive alpha and beta decays. The background decay in the series nuclei is the beta decay from ^{214}Pb to ^{214}Bi with a Q-value of 1.02 MeV. (The half-life is 27 minutes). The branching ratio is 10.9% according to

ENSDF. The beta decay of ^{214}Bi can be neglected by tagging the alpha decay of ^{214}Po in the daughter nucleus. ^{214}Po has an alpha decay with a Q-value of 7.7 MeV at a branching ratio of almost 100%, and its half-life is 160 µs. In this study, the radon concentration was assumed as 1 µBq/kg. The value is estimated on the reached concentration, 4.5 µBq/kg in the XENON1T Experiment and the new radon distillation columns for the XENONnT experiment.

^{220}Rn is an isotope in the thorium series and is emitted during the decay process. Downstream of ^{220}Rn is ^{212}Pb, which also undergoes beta decay. On the other hand, the concentration of ^{220}Rn is about 0.3% of that of ^{222}Rn, as measured in the XENON1T experiment. The background contribution of ^{212}Pb to ^{214}Pb is about 1%, which is negligible.

Xenon itself can be also an ER background source. There is an unstable isotope, ^{136}Xe, in xenon. The natural isotope ratio of ^{136}Xe is 8.9%, and the half-life of double beta decay is 2.17×10^{21} years. The Q-value of the double beta decay is 2.46 MeV. It is observed in the ROI of the WIMP search at a rate of 1.3 (keV t y)$^{-1}$. ^{124}Xe has a natural abundance ratio of 0.009% and is a two neutrino double electron capture, emitting neutrinos, electrons, and X-ray cascades. Double electron capture was first observed in the XENON1T experiment[93], and the half-life is 1.8×10^{22} years. In the Energy RoI, the energy loss is 9.8 keV with a branching ratio of 1.7% and a rate of 3.7 (t y)$^{-1}$. Outside the Energy RoI, the 36.7 keV and 64.3 keV lines exist with branching ratios of 23% and 75%, respectively. ^{127}Xe (half-life 36 days) is found in nature but is rarely produced by excitation by cosmic rays. ^{127}Xe is negligible with respect to other Xe background events.

^{85}Kr is another noble gas that pollutes xenon and undergoes beta decay with a half-life of 10.76 years. ^{85}Kr emits electrons of up to 687 keV and is observed in the Energy ROI as an inelastic background. In the XENON1T experiment, a ^{85}Kr/Xe ratio of 0.36 ppt (mol/mol) was achieved by xenon distillation. In the XENONnT experiment, a concentration of 0.1 ppt (mol/mol) is expected by further updating the distillation system. Using this concentration, the background rate in the Energy ROI is estimated to be 1.1 (keV t y)$^{-1}$. This effect is one-fifth of the background event in ^{222}Rn.

Solar neutrinos scatter elastically off the xenon nuclei, producing an ER signal in the Energy ROI region. The main sources of solar neutrinos contributing to the background event are pp-chain and i^{7}Be. This contribution is assumed to be 98% of the total neutrinos. Solar neutrinos are evaluated to be background events at a rate of 2.8 (keV t y)$^{-1}$ in the Energy ROI.

The evaluated amounts of the ER backgrounds are summarized in Table 5.3.

5.2.3 NR Backgrounds

The NR background event is a direct background event to the WIMP that is impossible to distinguish using the S1/S2 signal ratio. NR background events can be roughly classified into

Source	Rate [(t y)$^{-1}$]
Detector radioactivity	25 ± 3
^{222}Rn	55 ± 6
^{136}Xe	16 ± 2
^{124}Xe	4 ± 1
^{85}Kr	13 ± 1
Solar neutrinos	34 ± 1
Total	148 ± 7

TABLE 5.3. Evaluated amounts of the ER backgrounds.

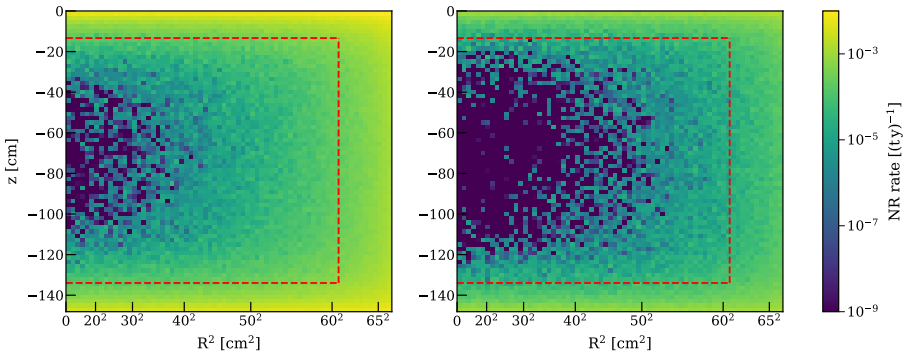

FIGURE 5.17. Spatial distribution of the radiogenic neutron backgrounds events without nVeto (Left) and with nVeto (Right).

those caused by neutrons and neutrinos. Neutron background events can be reduced by the newly introduced nVeto detector.

Neutrons as background events are produced by spontaneous fission (SF) of radioactive materials and by (α, n) reactions from α decay in the detector components. The SF is dominated by ^{238}U. The emission spectrum of SF is known as the Watt spectrum. SOURCES-4A was used as a tool to calculate the emission rates and spectra of (α, n) reactions. We neglect the reduction of the background event by the tag of γ-rays emitted simultaneously with neutrons conservatively but consider the single scattering event that causes the energy loss included in the Energy ROI in the TPC as the background event.

The fiducial volume (FV) is defined as the area approximately 6 cm inside the detector wall, then the background events from the detector material can be effectively reduced. Figure 5.17 shows the scattering positions of neutron background events in the detector. In addition, the nVeto detector at the outside of the TPC tags the neutron events. The design value of the nVeto tagging efficiency is 87%. The nVeto tagging efficiency will be evaluated with waveform simulator quantitatively in Section 4.3.

Cosmogenic neutron is also a candidate of NR backgrounds. Cosmic rays (mainly muon) activate the nuclei in the rocks of the laboratory and in the tank of the detector. Cosmic rays

Source	Rate [(t y)$^{-1}$]
Neutrons with nVeto (design)	4.1×10^{-2}
CEνNS (Solar ν)	6.3×10^{-3}
CEνNS (Atm + DSN)	5.4×10^{-2}
Total	1.0×10^{-2}

TABLE 5.4. Evaluated amounts of the NR backgrounds.

directly excite a nucleus around the detector. The products of the cosmic ray can be tagged by μVeto and nVeto detectors. The background rate is estimated to be less than 0.01 (t y)$^{-1}$ in the energy ROI, based on experience from the XENON1T experiment. It is negligible for other backgrounds, ER, neutron, and neutrino.

The CEνNS also makes NR backgrounds. The CEvNS background events include solar neutrino, atmospheric neutrino (Atm neutrino) and, diffuse supernova neutrino (DSN neutrino). The rates that can be expected in these Energy ROIs are evaluated independently. The major sources of solar neutrinos are produced with called ^{8}B process ($^8\mathrm{B} \rightarrow^8 \mathrm{B}^* + e^+ + \nu_e$) and hep process ($^3\mathrm{He} + p \rightarrow^4 \mathrm{He} + e^+ + \nu_e$). The production spectra of ^{8}B neutrinos can be neglected because the spectra are less than the lower limit of the Energy ROI, 4 keV. Neutrinos from hep are expected in the Energy ROI at a rate of 6.3×10^{-3} (t y)$^{-1}$. Atm neutrino is expected at the rate of 4.8×10^{-2} (t y)$^{-1}$, DSN neutrino is observed at the rate of 5.6×10^{-3} (t y)$^{-1}$. The spectra are shown in Figure 5.16.

The evaluated amounts of the NR backgrounds are summarized in Table 5.4. The uncertainties of the backgrounds are evaluated in Section 6.3.

CHAPTER 6

Evaluation of WIMP Sensitivity

WIMP sensitivity of the XENONnT experiment is evaluated in this chapter.

6.1 nVeto performance

To estimate WIMP sensitivity, the nVeto detector performance should be evaluated. We updated the performance evaluation of the nVeto detector, especially the tagging efficiency, making use of the waveform simulations described in the previous chapter.

The nVeto tagging efficiency, ϵ_{tag} is defined as,

$$\epsilon_{\mathrm{tag}} = \frac{N_{\mathrm{nVeto}}}{N_{\mathrm{TPC}}}, \tag{6.1}$$

where N_{TPC} is the number of the NR single scatter events in the energy ROI and the 4 tonne fiducial volume in the TPC. The N_{nVeto} is the number of tagged events in the nVeto detector with the following selections.

To determine the tagged events in the nVeto detector, several cuts have been applied. First cuts are for these variables, 'area', 'n_hits' of 'events_nv'. They are the observed light intensity and the total number of hits observed. The PMTs of the nVeto detector typically observe a dark current at $\sim$ 2 kHz. The livetime of the TPC will be significantly reduced if we use the raw rates of the PMTs. The dark current generates a hit equivalent to 1 PE in a random PMT. We use 'area' and 'n_hits' of 'events_nv' to eliminate the dark current events. Figures 6.1 to 6.4 show the distribution of the 'area' and 'n_hits' and its tagging efficiencies when the events are less than the value are removed. Fisures 6.1 and 6.2 are for 'area', Figure 6.3 and 6.4 are for 'n_hits'. The tagging efficiency with the loosest cut is not 100%. The nVeto inefficiency comes from the neutron capture in the TPC. There is an insensitive region in the TPC cryostat, typically, the LXe region under the bottom PMT array. If the neutron is captured in the region, the signal has been observed in neither TPC nor nVeto.

In addition to the cuts, we determined the time difference between TPC and nVeto events, defined as ΔT. Figure 6.5 shows the distribution of the ΔT between the simulated nVeto and TPC events. The longer time window increases the tagging efficiency whereas reduces

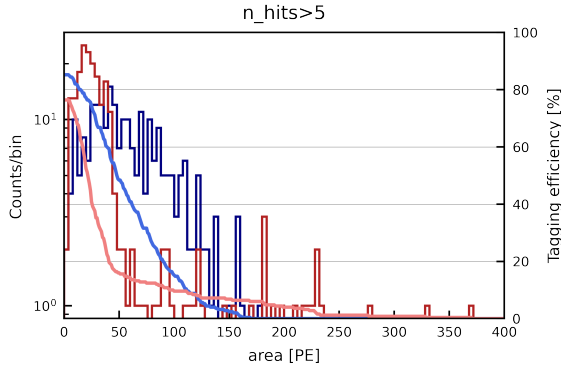

FIGURE 6.1. 'area' distribution and nVeto tagging efficiency for pure water (dark red) and Gd-water (dark blue). The light red and blue lines show the tagging efficiencies with the events more than the 'area'. The tagging efficiencies calculated with 'n_hits'>5 and ΔT less than 600 μs and 100 μs for pure water and Gd-water, respectively.

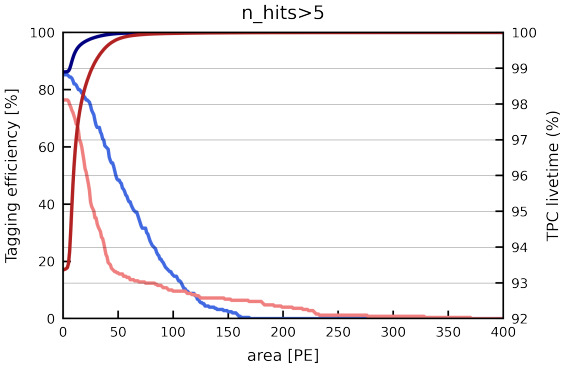

FIGURE 6.2. TPC livetime is shown in dark blue and red lines for Gd-water and pure water with 'area' criteria. The nVeto tagging efficiencies with 'area' cut for pure water (light red) and Gd-water (light blue) (Same plots for Figure 6.1).

the TPC livetime. Figure 6.6 shows the dependences of the tagging efficiency and the TPC livetime on the ΔT. The livetime is calculated with the commissioning data taken with the same condition of the WIMP search. There is a trade-off between these two values: if we increase the ΔT threshold to achieve high tagging efficiency, the TPC livetime decreases. Almost all events are tagged with a time window of 100 μs for Gd-water. In the case of pure water without gadolinium, a longer Veto time window is required. In this study, events with ΔT<100 μs for Gd-water and with ΔT<600 μs for pure water are determined as the time window for the neutron tagging.

Considering the tagging efficiency and TPC livetime, 'area'>5, 'n_hits'>5, and ΔT<100 μs (600 μs), are determined as the criteria to select the nVeto events for Gd-water (pure water). The obtained nVeto tagging efficiencies are $(84.8 \pm 1.1_{\mathrm{stat.}})\%$ and $(76.0 \pm 1.4_{\mathrm{stat.}})\%$ with the TPC livetime of 98.9% and 93.5% for Gd-water and pure water, respectively. In particular, for Gd-water, we obtained tagging efficiency values close to the initial design values, 87%. In the simulations constructed using the real data, the detector response of the PMTs was more realistically evaluated, and it is considered that the obtained tagging efficiency is slightly lower than the preliminary simulations with optimistic parameters. In contrast, a slightly better value than the design value of 98.5% was obtained for the TPC live time with these realistic simulation results. The design values are evaluated by the results based on the dark rate of PMT measured in a small water tank before starting the nVeto experiment. Systematic uncertainties are evaluated in Section 6.3.

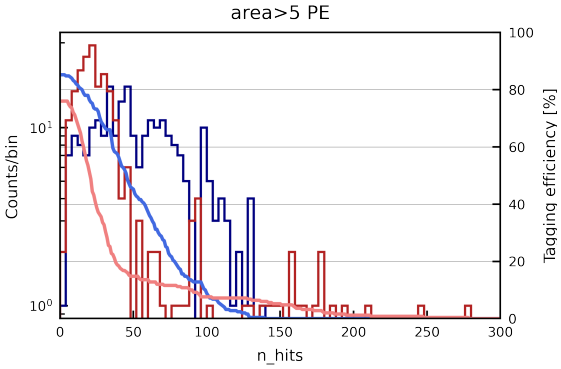

FIGURE 6.3. "n_hits' distribution and nVeto tagging efficiency for pure water (dark red) and Gd-water (dark blue). The light red and blue lines show the tagging efficiencies with the events more than the 'n_hits'. The tagging efficiencies calculated with 'area'>5 and ΔT less than 600 µs and 100 µs for pure water and Gd-water, respectively.

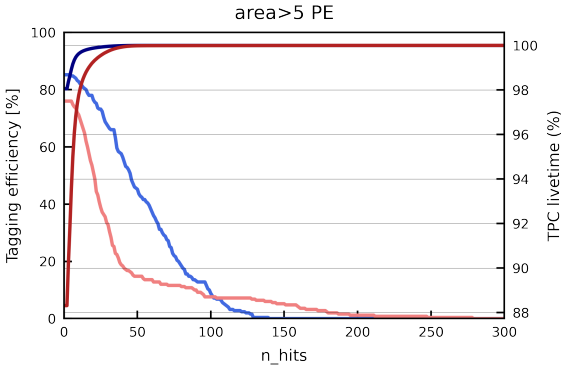

FIGURE 6.4. TPC livetime for 'n_hits' criteria (dark blue and red lines). The nVeto tagging efficiencies for 'n_hits' (Same plots for Figure 6.3).

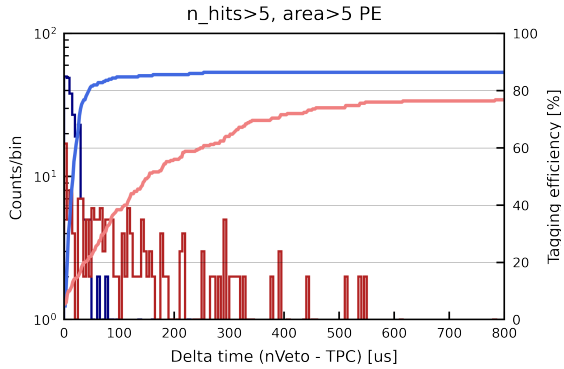

FIGURE 6.5. ΔT from TPC single scatter events to nVeto events in pure water (dark red) and Gd-water (dark blue) targets. The light red and blue lines show the tagging efficiencies with the ΔT cuts for pure water and Gd-water, respectively.

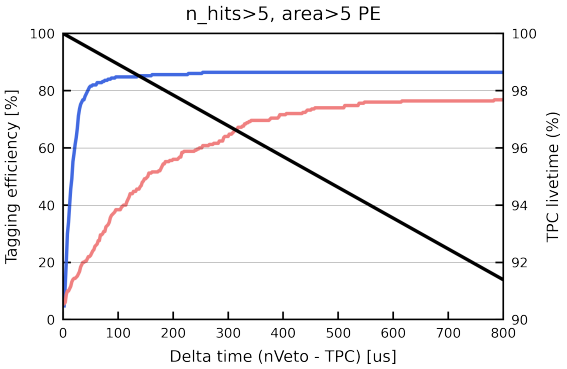

FIGURE 6.6. nVeto tagging efficiencies for ΔT and TPC livetime (black line).

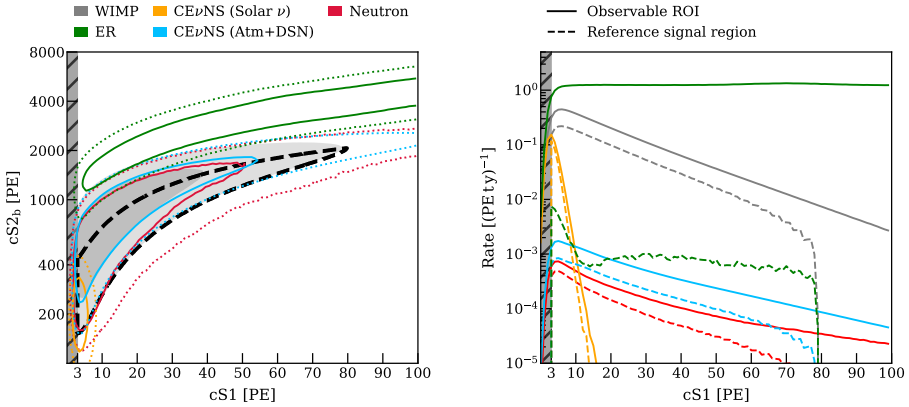

FIGURE 6.7. (Left) Background and WIMP signal PDFs in the (cS1, $cS2_b$) space. The solid and dotted lines show 1 and 2σ regions. (Right) Rates projections onto cS1 space.

6.2 Backgrounds and WIMP signal models

The ER and NR background rates were estimated in the previous chapter. They are summarized Tables 5.3 and 5.4. Expected signals in the TPC are characterized by the magnitudes of the S1 and S2 signals. We use the corrected S1 signal (cS1) as in the method used in the XENON1T experiment, and the corrected S2 signal ($cS2_b$) constructed by the PMT at the bottom taking into account position-dependent light collection efficiency, PMT Q.E., liquid xenon temperature [94], and PMT collection efficiency at the first dynode. In agreement with the method followed for the XENON1T experiment results [95], the S2 signals were reconstructed with the bottom PMT array because the signals with top PMTs are highly localized and the bottom signals are more uniform and robust for variable light collection efficiency. Figure 6.7 shows the expected responses in the TPC for WIMP and background signals. The neutron background is overlapping the WIMP signals in the parameter spaces thus we installed the nVeto detector to discriminate the backgrounds. CEνNS is also on the WIMP signal region. CEνNS (Solar) and CEνNS (Atm+DSN) have a chance to obtain information in projected cS1 spectra shown in the right panel of Figure 6.7 . The ER background is clearly discriminated from the WIMP signal region. In the XENON1T experiment, the ER discrimination power is 99.7%. An ER discrimination power is estimated to be 99.9% for the XENONnT experiment from the XENON1T experience with a 50% NR events acceptance. An observable ROI is defined as (3, 100) PE of cS1. Table 6.1 shows the expected number of the background events in the observable ROI and reference signal region (the energy ROI and fiducial volume) applying the discrimination. With the nVeto, an impact of the neutron background is smaller than the other backgrounds. As a reference, the expected numbers of the WIMP signals are shown in Table 6.2. The numbers are a demonstration of our background-less detector of the XENONnT. The sensitivity of the XENONnT experiment with the background rate was evaluated using a profile likelihood method in Section 6.4.

Background source	Expectation value [20 t y]	
	Observable ROI	Reference signal region
ER	2400	1.6
Neutrons with nVeto (without nVeto)	0.29	0.15 (1.0)
CEvNS (Solar)	7.6	5.4
CEvNS (Atm + DSN)	0.82	0.36

TABLE 6.1. Expected number of the background events.

WIMP signal	Expectation value [20 t y]	
	Observable ROI	Reference signal region
6 GeV/c^2 ($\sigma_{\rm DM} = 3 \times 10^{-44}$cm^2)	25	19
50 GeV/c^2 ($\sigma_{\rm DM} = 5 \times 10^{-47}$cm^2)	186	88
1 TeV/c^2 ($\sigma_{\rm DM} = 8 \times 10^{-46}$cm^2)	286	118

TABLE 6.2. Expected numbers of the WIMP events in each mass. The cross sections are close to limits evaluated in the XENON1T experiment.

Component		Rate uncertainty [%]
Neutron	Material amount	$\sim$10
	Neutron Production	$\sim$30
	Simulation transportation	0.15
	Tagging analysis	1.3
CEνNS (Solar ν)		$\sim$4
CEνNS (Atm+DSN)		$\sim$20

TABLE 6.3. Summary of the systematic uncertainty of the NR rate.

6.3 Systematic Uncertainties

The systematic uncertainties for the NR rate analysis are evaluated. Table 6.3 summarizes the uncertainties for the NR rate. The main uncertainty for the NR rate comes from the neutron background. The evaluation of the amount of the radioactive materials including the detector components has approximately 10% uncertainty. The neutrons are produced in the materials with (α, n) reaction and spontaneous fission. The (α, n) reaction cross section has the largest uncertainties evaluated with the tool, SOURCES–4A. The uncertainty was evaluated to be approximately 30% [96] with the comparison of a novel alternative tool, NeuCBOT [97]. The NeuCBOT is based on TALYS [98], a general calculation tool. The difference between these tools was used to estimate the uncertainties. I used the value in both (α, n) reaction and spontaneous fission conservatively. Neutron transportation uncertainty in the simulation was suppressed with the reflectivity monitor calibration. The uncertainty is related to the photon survival probability in the nVeto detector thus the optical calibration using photon detection time-constant evaluates the transportation behavior. The transportation uncertainty is evaluated to be 0.15% with the data-driven calibration described in Section 4.4. The tagging analysis with the 'area' and 'amplitude' of the 'hitlets_nv' has also uncertainty.

Estimated uncertainty by considering the binomial distribution errors was 1.3%. Once the data acquisition is completed, the neutron rate can be evaluated more accurately by using the background data and the calibration data. The uncertainties of the simulation transportation and the tagging analysis will be other uncertainties.

The uncertainties of the solar neutrino backgrounds should be considered for the NR events rate. The prediction of the uncertainty of the ^{8}B neutrino flux is evaluated as 4% in a SNO study [99]. For the atmospheric and DSN neutrino, the uncertainty is evaluated with a simulation knowledge [100], as 20% in this study. This uncertainty is used for the WIMP sensitivity evaluation.

6.4 WIMP sensitivity

Background and WIMP event rates were known by the simulation through the studies up to the previous section. In this section, I evaluate the sensitivity of WIMP using a likelihood-based statistical model. The extended unbinned likelihood $\mathcal{L}$ is given by the following equation.

$$\mathcal{L}(\sigma_{\rm DM}, \boldsymbol{\theta}) = \mathrm{Pois}(N|\ \mu_{\rm tot}(\sigma_{\rm DM}, \boldsymbol{\theta})) \cdot \prod_{i=1}^{N} \left[\sum_c \frac{\mu_c(\sigma_{\rm DM}, \boldsymbol{\theta})}{\mu_{\rm tot}(\sigma_{\rm DM}, \boldsymbol{\theta})} \cdot f_c(\boldsymbol{x}_i|\boldsymbol{\theta}) \right] \cdot \mathcal{L}_{\rm anc}(\boldsymbol{\theta})\ . \quad (6.2)$$

The $\mathcal{L}$ depends on the cross section of the dark matter $\sigma_{\rm DM}$ and nuisance parameters $\boldsymbol{\theta}$. The N is a vector of observed events, and the index of each event is i. The $\mu_{\rm tot}(\sigma, \boldsymbol{\theta}) \equiv \sum_c \mu_c(\sigma, \boldsymbol{\theta})$ and the $\mu_c(\sigma, \boldsymbol{\theta})$ is an expectation number for each c, which components (DM, background sources). $f_c(\boldsymbol{x}_i|\boldsymbol{\theta})$ is PDFs for the each component with a PDF $\boldsymbol{x}$ = (cS1, cS2$_{\rm b}$). The $\mathcal{L}_{\rm anc}$ is an ancillary term defined as

$$\mathcal{L}_{\rm anc}(\boldsymbol{\theta}) \equiv \prod_k \mathrm{Gaus}(\hat{\mu}_k|\ \mu_k, \xi_k)\ , \quad (6.3)$$

where k is an index for background components (neutron, solar neutrino, and Atm+DSN neutrino). The rate uncertainties ξ from ancillary measurements are taken into account as Gaussian constraints in this term.

For each DM mass, $M_{\rm DM}$, the profiled log-likelihood $q(\sigma_{\rm DM})$ is defined as,

$$q(\sigma_{\rm DM}) \equiv -2 \cdot \log \frac{\mathcal{L}(\sigma_{\rm DM}, \hat{\hat{\boldsymbol{\theta}}})}{\mathcal{L}(\hat{\sigma}_{\rm DM}, \hat{\boldsymbol{\theta}})} \quad (6.4)$$

The likelihood is maximised at $(\hat{\sigma}_{\rm DM}, \hat{\boldsymbol{\theta}})$, and $\hat{\hat{\boldsymbol{\theta}}}$ are the nuisance parameters that maximize the likelihood for a given $\sigma_{\rm DM}$. The distributions of $q(\sigma_{\rm DM})$ are estimated with $\mathcal{O}(10^4)$ toy MC simulations of the experimental data, including both the science data and ancillary measurements.

Figure 6.8 shows a projected sensitivity for Spin-independent WIMPs of the XENONnT experiment. Figure 6.9 shows the sensitivity as a function of the exposure. Both plots are

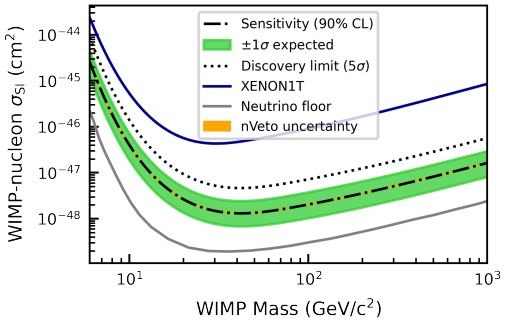

FIGURE 6.8. Projections of the XENONnT sensitivity (dashed line) with 1σ band (green) for an ultimate exposure, 20 [t y] [101]. The discovery limit (5σ) is shown in a dotted line. The nVeto uncertainty region (orange) is overlapped the sensitivity line.

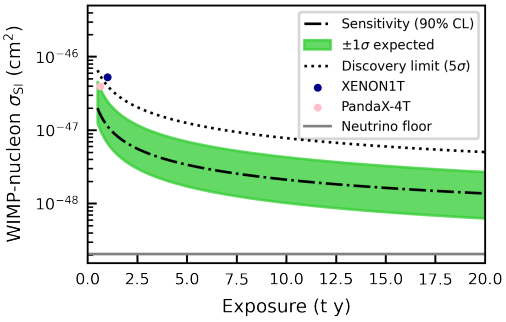

FIGURE 6.9. The sensitivity for the exposure for 50 GeV/c^2 WIMP with XENONnT experiment [101]. The grey solid line shows the neutrino floor as known as the ultimate background. The markers show the XENON1T final result [102] and PandaX-4T commissioning result [20].

for the 50 GeV/c^2 WIMP. The sensitivity is limited by the background events, and with an exposure of 20 [t y], it is expected to update the sensitivity of the XENON1T experiment by more than an order of magnitude. At a 90% confidence level, the sensitiviety is 1.4×10^{-48} cm^2 for 50 GeV/c^2 WIMPs. The major background for the exposure will be the CEνNS. The neutron background is expressed to be suppressed with the nVeto detector. Except for the ultimate background events of neutrinos, the nVeto has greatly reduced the number of the neutron background events that can be dealt with. The estimated nVeto uncertainty affects the sensitivity less than 1%.

In the first science run of the XENONnT, the XENONnT experiment will update the current upper limit set by the PandaX-4T experiment [20]. The sensitivity and that for the exposure for SD WIMP were also evaluated in Figure 6.10. The sensitivity for the SD WIMPs will be updated to the result reported by PICO–60 experiment [33] for several tens GeV/c^2 WIMPs. The Sub-GeV region search is limited with the threshold.

The XENONnT experiment with the new nVeto detector is ready to release its results in the aspect of the simulation. The XENONnT experiment is ready to search WIMP dark matter in the world-leading sensitivity with the nVeto detector. The expected sensitivity is reaching the neutrino floor and the dominant background is expected to be neutrino. Almost all current experiments do not have a technique to exclude neutrino signals except for directional search projects. The XENONnT and planned DARWIN experiment will find the WIMP signals or conclude that we should develop new techniques to find WIMPs beyond the neutrino floor.

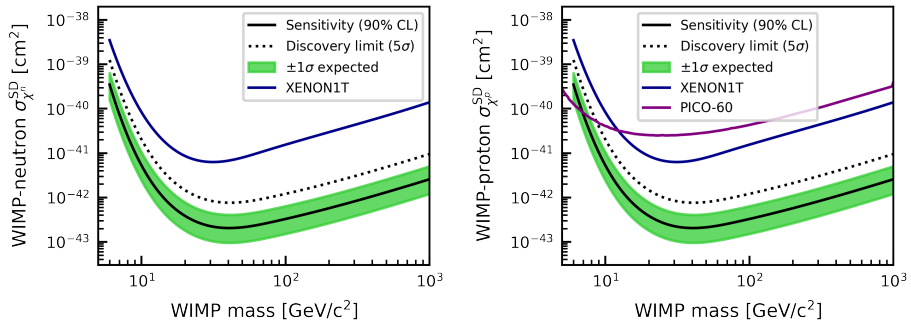

FIGURE 6.10. Projections of the XENONnT sensitivity and discovery power in the search for spin-dependent WIMP-neutron and WIMP-proton couplings with exposure, 20 [t y] [101].

CHAPTER 7

Discussion

The remaining issues for the further development of this research are discussed in this chapter.

7.1 Correction factor of the nVeto PMT

To calibrate the number of the observed photons, the PMT correction factor has been introduced as ϵ_c in Section 5.1.4. One of the reasons to reduce the number is the unknown PMT C.E. The provided Q.E. doesn't include the C.E. effect. However, the ϵ_c value, 0.7852 is slightly smaller than the general PMT C.E. It suggests that there is another reason to lose photons.

The ϵ_c is calibrated with a 2.2 MeV peak of the AmBe source. The light yield is fully understood in the simulation, thus the number of generated photons is reliable.

The photon behavior in the nVeto detector is calibrated with the reflectivity monitor as ePTFE reflectivity. The ePTFE reflectivity includes the reflection of PMT, the absorption of water, and the effect of fine structures. The wavelength of the laser is 375 nm, which is designed in consideration of the sensitivity wavelengths of Cherenkov light and the PMT of nVeto (Figure 4.16). Thus the behavior should be matched for the wavelength. However, if the water specifically absorbs light in a specific wavelength region other than 375 nm, the simulation overestimates the light intensity. The ϵ_c is independent of the wavelength in this study. The direct measurement of the water absorption length or the reflectivity monitor calibration with another wavelength will figure it out.

The ϵ_c calibrates the 2.2 MeV peak with the AmBe calibration source, however, they are slightly different at higher energy regions. Figure 7.1 reprints Figure 5.13. There is a discrepancy between the measured data and the simulation results in 4.4 MeV for the AmBe calibration source. This discrepancy should be attributed to neglecting the minor branch described Equation 3.5 at the AmBe source which was not taken into account. It is expected to be improved by updating the primary generator of Geant4. Since this AmBe source is used for calibration, the minor branch cannot be evaluated on the basis of observations with the nVeto detector. It is necessary to measure and implement the AmBe prompt γ-ray and neutron energy in detail with independent detectors and setups. This update will allow us to expand

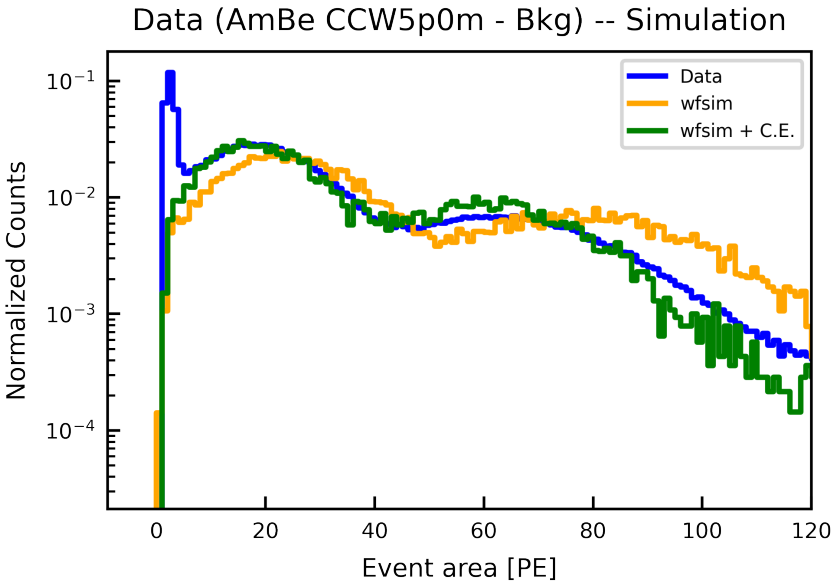

FIGURE 7.1. Figure 5.13 (reprinted). The distribution calibrated for 2.2 MeV is matched, however, they are slightly different at higher energy regions.

the energy range of the simulation to a higher one. It should be noted that the main result of this work, evaluated tagging efficiency, is not affected even before the update because the detector was well-calibrated at relevant energy, 2.2 MeV.

7.2 Waveform simulator improvements

More improvements are necessary for future analyses using machine learning, in which the output of the simulation is used as supervised data. First, the shape of the waveform shown as the amplitude distribution (Figure 5.11) can be improved. This variable 'amplitude' is used only in the threshold and not in the later analysis. However, if the distributions do not match, it means that the waveform is not perfectly reproduced. This discrepancy would be attributed to the simple linear-scalings of template pulse to produce the waveforms.

A statistical uncertainty that comes from the number of electrons observed in PMTs may be the reason. Electrons amplified by PMT have been observed in the PMT anode. Then we see the numbers of electrons in a small time window as a current. The bin should have uncertainties, $\sqrt{N_{e,\mathrm{bin}}} \propto \sqrt{\mathrm{pulse\ height}}$. The higher ADC bins have more uncertainties. The 'amplitude' is the highest bin in a pulse thus the distribution is smeared. In addition, the effects of unexpected baseline noise and bin-bin correlation are not fully taken into account. This simulation applied the baseline noise recorded with an external trigger. If the baseline noises are not perfectly the same for the self-trigger mode used for WIMP search, that is a bias for the pulse. The 'amplitude', the highest bin in a pulse is affected by the noise fluctuation. Another reason is a bin–bin correlation which depends on the arriving timing of electron to

the anode. The digitizer sampling rate of the nVeto is 500 MS/s. It is a small window for pulse timing. There is uncertainty as to whether the current produced by an electron will enter one bin as the peak or not. This effect has also smeared the distribution.

One solution is to map a large number of actual SPE pulses to the simulated hits, instead of starting from a template pulse. Although this solution cannot completely reproduce the noise, it is considered to be almost negligible with the current noise level of the nVeto detector. In order to realize this update, it is necessary to improve the performance of the simulator because it needs to handle a large number of template pulses. The current python-based simulator is based on the Numpy framework, which requires a certain amount of waveforms to be loaded into memory at once for parallel computation but the memory is not enough for the approach. Thus, a drastic update will be necessary to enable event-based iterable computation.

CHAPTER 8

Conclusions

Even though cosmology and observations of the universe strongly suggest the existence of dark matter, especially WIMPs, direct scattering has not been detected yet. One of the world-leading direct WIMP searches, the XENONnT experiment completed the commissioning and is almost ready to release its first science run results. The XENONnT detector is able to discriminate most of the electron recoil background events with light and charge signals. Other background sources for the WIMP search are evaluated in this study. In particular, a neutron is one of the most serious backgrounds in the rest. We introduced a new water Cherenkov detector to veto neutrons as an upgrade from the XENON1T experiment. With the commissioning data, a data-driven simulation is constructed. The simulation physics on the Geant4 framework is tuned up with an independent beam experiment. The optical behavior in the detector was calibrated with the optical calibrations. The detector performance was characterized by material reflectivity including effects of water absorption and reflection at PMT surface. The unknown PMT collection efficiencies and other effects to lose the photons are also calibrated with a source calibration. Finally, the simulation framework constructs waveforms were implemented in the simulation with the same format of the data so that both can be processed with the same analysis chain. As a result of this work, a neutron tagging efficiency of 84.8% and TPC livetime of 98.9% were obtained. In addition, systematic uncertainty for the tagging efficiency was estimated.

With the established simulation, we evaluated the amounts of the backgrounds and obtained WIMP sensitivity for the XENONnT experiment. The sensitivity of the XENONnT experiment to the SI (SD WIMP, including the nVeto detector, was evaluated to be 1.4×10^{-48} cm^2 (2.2×10^{-43} cm^2 for neutron) for 50 GeV/c^2 mass at a 90% confidence level. The XENONnT experiment with the new nVeto detector is ready to release its results in the aspect of the simulation.

Acronyms

μVeto: muon Veto. 24

ALPS: Axion-Like ParticleS. 9
AmBe: Ameritium-Belyrium. 25
Atm neutrino: Atmospheric neutrino. 66

C.E.: Collection Efficiency. 37
CCD: Charge-Coupled Device. 14
CDM: Cold Dark Matter. 4
CEνNS: Coherent Elastic Neutrino-Nucleus Scattering. 62, 66
CMB: Cosmic Microwave Background. 4
cS1: corrected S1 signal. 70
cS2$_b$: corrected S2 signal with bottom PMT array. 70

DAQ: Data AcQuisition system. 37
DPP-DAW: Digital Pulse Processing with Dynamic Acquisition Window. 28
DSN neutrino: Diffuse Supernova Neutrino. 66

ePTFE: expanded PolyTetraFluoroEthylene. 2, 23, 38
ER: Electron Recoil. 19

Fermi-LAT: Fermi Large Area Telescope. 17
FV: Fiducial Volume. 65

HV: High Voltage. 37

ICP-MS: Inductively Coupled Plasma Mass Spectrometry. 15, 62
INFN: Istituto Nazionale di Fisica Nucleare (National Institute for Nuclear Physics). 19

LED: Light Emitting Diode. 40
LHC: Large Hadron Collider. 18
LNGS: Laboratori Nazionali del Gran Sasso (National Laboratory of Gran Sasso). 13, 19
LSM: Laboratoire Souterrain de Modane (Modane Underground Laboratory). 14
LUX: Large Underground Xenon Experiment. 13
LXe: Liquid Xenon. 56

MLF: Materials and Life science experimental Facility. 54
MOND: MOdified Newtonian Dynamics. 6

NEST: Noble Element Simulation Technique. 56
NR: Nuclear Recoil. 19
nVeto: neutron Veto. 23, 33
NYC: Nippon Yttrium Co. LTD.. 34

PandaX: Particle AND Astrophysical Xenon (Experiment). 13
PBH: Primordial Black Hole. 9
PE: Photo-Electrons. 40
PMT: Photomultiplier Tube. 1, 20, 33
PSD: Pulse Shape Descrimination. 14
PTFE: PolyteTraFluoroEthylene. 21

Q.E.: Quantum Efficiency. 20, 35

ROI: Range Of Interest. 62

S1: 1st Signal of scintillation light in TPC. 22
S2: 2nd Signal of electroluminescence light in TPC. 22
SD: Spin-Dependent. 10, 78
SF: Spontaneous Fission. 65
SHM: Standard Halo Model. 7
SI: Spin-Independent. 10, 78
SPE: Single PhotoElectron. 43
SURF: Sanford Underground Laboratory. 13

TPC: Time Projection Chamber. 1, 13, 19
Treibacher: Treibacher Industrie AG. 34

WIMP: Weakly Interacting Massive Particle. 1, 8, 19

References

[1] E Aprile et al. 'Dark Matter Search Results from a One Ton-Year Exposure of XENON1T'. In: *Phys. Rev. Lett.* 121 (11 Sept. 2018), p. 111302. DOI: 10.1103/PhysRevLett.121.111302. URL: https://link.aps.org/doi/10.1103/PhysRevLett.121.111302.

[2] Y Suzuki. 'The Super-Kamiokande experiment'. In: *The European Physical Journal C* 79.4 (2019), p. 298. ISSN: 1434-6052. DOI: 10.1140/epjc/s10052-019-6796-2. URL: https://doi.org/10.1140/epjc/s10052-019-6796-2.

[3] European Space Agency and Planck Collaboration. *Planck CMB*. URL: %5Curl%7Bhttps://www.esa.int/ESA_Multimedia/Images/2013/03/Planck_CMB%7D.

[4] PAR Ade et al. 'Planck 2013 results. XVI. Cosmological parameters'. In: *Astronomy & Astrophysics* 571 (Nov. 2014), A16. ISSN: 0004-6361. DOI: 10.1051/0004-6361/201321591. URL: http://www.aanda.org/10.1051/0004-6361/201321591.

[5] JD Simon. 'The Faintest Dwarf Galaxies'. In: *Annual Review of Astronomy and Astrophysics* 57.1 (2019), pp. 375–415. DOI: 10.1146/annurev-astro-091918-104453. eprint: https://doi.org/10.1146/annurev-astro-091918-104453. URL: https://doi.org/10.1146/annurev-astro-091918-104453.

[6] D Clowe et al. 'A Direct Empirical Proof of the Existence of Dark Matter'. In: *The Astrophysical Journal* 648.2 (Aug. 2006), pp. L109–L113. DOI: 10.1086/508162. URL: https://doi.org/10.1086/508162.

[7] F Zwicky. 'Die Rotverschiebung von extragalaktischen Nebeln'. In: *Helvetica Physica Acta* 6 (Jan. 1933), pp. 110–127.

[8] KG Begeman, AH Broeils and RH Sanders. 'Extended rotation curves of spiral galaxies: dark haloes and modified dynamics'. In: *Monthly Notices of the Royal Astronomical Society* 249.3 (Apr. 1991), pp. 523–537. ISSN: 0035-8711. DOI: 10.1093/mnras/249.3.523. eprint: https://academic.oup.com/mnras/article-pdf/249/3/523/18160929/mnras249-0523.pdf. URL: https://doi.org/10.1093/mnras/249.3.523.

[9] B Famaey and SS McGaugh. 'Modified Newtonian Dynamics (MOND): Observational Phenomenology and Relativistic Extensions'. In: *Living Reviews in Relativity* 15.1 (2012), p. 10. ISSN: 1433-8351. DOI: 10.12942/lrr-2012-10. URL: https://doi.org/10.12942/lrr-2012-10.

[10] SW Randall et al. 'Constraints on the Self-Interaction Cross Section of Dark Matter from Numerical Simulations of the Merging Galaxy Cluster 1E 0657-56'. In: *The Astrophysical Journal* 679.2 (June 2008), pp. 1173–1180. DOI: 10.1086/587859. URL: https://doi.org/10.1086/587859.

[11] SD McDermott, HB Yu and KM Zurek. 'Turning off the lights: How dark is dark matter?' In: *Phys. Rev. D* 83 (6 Mar. 2011), p. 063509. DOI: 10.1103/PhysRevD.83.063509. URL: https://link.aps.org/doi/10.1103/PhysRevD.83.063509.

[12] S Tremaine and JE Gunn. 'Dynamical Role of Light Neutral Leptons in Cosmology'. In: *Phys. Rev. Lett.* 42 (6 Feb. 1979), pp. 407–410. DOI: 10.1103/PhysRevLett.42.407. URL: https://link.aps.org/doi/10.1103/PhysRevLett.42.407.

[13] B Audren et al. 'Strongest model-independent bound on the lifetime of Dark Matter'. In: *Journal of Cosmology and Astroparticle Physics* 2014.12 (Dec. 2014), pp. 028–028. DOI: 10.1088/1475-7516/2014/12/028. URL: https://doi.org/10.1088/1475-7516/2014/12/028.

[14] EO Nadler et al. 'Constraints on Dark Matter Microphysics from the Milky Way Satellite Population'. In: *The Astrophysical Journal* 878.2 (June 2019), p. L32. DOI: 10.3847/2041-8213/ab1eb2. URL: https://doi.org/10.3847/2041-8213/ab1eb2.

[15] MA Monroy-Rodriguez and C Allen. 'New limits on macho masses from halo wide binaries'. In: *The Astrophysical Journal* 790.2 (July 2014), p. 159. DOI: 10.1088/0004-637x/790/2/159. URL: https://doi.org/10.1088/0004-637x/790/2/159.

[16] JI Read. 'The local dark matter density'. In: *Journal of Physics G: Nuclear and Particle Physics* 41.6 (May 2014), p. 063101. DOI: 10.1088/0954-3899/41/6/063101. URL: https://doi.org/10.1088/0954-3899/41/6/063101.

[17] D Hooper. *TASI 2008 Lectures on Dark Matter*. 2009. eprint: arXiv:0901.4090.

[18] RD Peccei and HR Quinn. 'CP Conservation in the Presence of Pseudoparticles'. In: *Phys. Rev. Lett.* 38 (25 June 1977), pp. 1440–1443. DOI: 10.1103/PhysRevLett.38.1440. URL: https://link.aps.org/doi/10.1103/PhysRevLett.38.1440.

[19] M Sasaki et al. 'Primordial Black Holes - Perspectives in Gravitational Wave Astronomy -'. In: (2018). DOI: 10.1088/1361-6382/aaa7b4. eprint: arXiv:1801.05235.

[20] Y Meng et al. 'Dark Matter Search Results from the PandaX-4T Commissioning Run'. In: *Phys. Rev. Lett.* 127 (26 Dec. 2021), p. 261802. DOI: 10.1103/PhysRevLett.127.261802. URL: https://link.aps.org/doi/10.1103/PhysRevLett.127.261802.

[21] DS Akerib et al. 'Results from a Search for Dark Matter in the Complete LUX Exposure'. In: *Phys. Rev. Lett.* 118 (2 Jan. 2017), p. 021303. DOI: 10.1103/PhysRevLett.118.021303. URL: https://link.aps.org/doi/10.1103/PhysRevLett.118.021303.

[22] R Ajaj et al. 'Search for dark matter with a 231-day exposure of liquid argon using DEAP-3600 at SNOLAB'. In: *Phys. Rev. D* 100 (2 July 2019), p. 022004. DOI:

10.1103/PhysRevD.100.022004. URL: https://link.aps.org/doi/10.1103/PhysRevD.100.022004.

[23] P Agnes et al. 'Low-Mass Dark Matter Search with the DarkSide-50 Experiment'. In: *Phys. Rev. Lett.* 121 (8 Aug. 2018), p. 081307. DOI: 10.1103/PhysRevLett.121.081307. URL: https://link.aps.org/doi/10.1103/PhysRevLett.121.081307.

[24] R Agnese, T Aramaki et al. 'Results from the Super Cryogenic Dark Matter Search Experiment at Soudan'. In: *Phys. Rev. Lett.* 120 (6 Feb. 2018), p. 061802. DOI: 10.1103/PhysRevLett.120.061802. URL: https://link.aps.org/doi/10.1103/PhysRevLett.120.061802.

[25] DS Akerib, S Alsum et al. 'Results of a Search for Sub-GeV Dark Matter Using 2013 LUX Data'. In: *Phys. Rev. Lett.* 122 (13 Apr. 2019), p. 131301. DOI: 10.1103/PhysRevLett.122.131301. URL: https://link.aps.org/doi/10.1103/PhysRevLett.122.131301.

[26] E Aprile, J Aalbers, F Agostini, M Alfonsi, L Althueser, FD Amaro, VC Antochi, E Angelino et al. 'Search for Light Dark Matter Interactions Enhanced by the Migdal Effect or Bremsstrahlung in XENON1T'. In: *Phys. Rev. Lett.* 123 (24 Dec. 2019), p. 241803. DOI: 10.1103/PhysRevLett.123.241803. URL: https://link.aps.org/doi/10.1103/PhysRevLett.123.241803.

[27] E Aprile et al. 'Light Dark Matter Search with Ionization Signals in XENON1T'. In: *Phys. Rev. Lett.* 123 (25 Dec. 2019), p. 251801. DOI: 10.1103/PhysRevLett.123.251801. URL: https://link.aps.org/doi/10.1103/PhysRevLett.123.251801.

[28] P Agnes et al. 'Low-Mass Dark Matter Search with the DarkSide-50 Experiment'. In: *Phys. Rev. Lett.* 121 (8 Aug. 2018), p. 081307. DOI: 10.1103/PhysRevLett.121.081307. URL: https://link.aps.org/doi/10.1103/PhysRevLett.121.081307.

[29] R Agnese, T Aralis et al. 'Search for low-mass dark matter with CDMSlite using a profile likelihood fit'. In: *Phys. Rev. D* 99 (6 Mar. 2019), p. 062001. DOI: 10.1103/PhysRevD.99.062001. URL: https://link.aps.org/doi/10.1103/PhysRevD.99.062001.

[30] AH Abdelhameed et al. 'First results from the CRESST-III low-mass dark matter program'. In: *Phys. Rev. D* 100 (10 Nov. 2019), p. 102002. DOI: 10.1103/PhysRevD.100.102002. URL: https://link.aps.org/doi/10.1103/PhysRevD.100.102002.

[31] Q Arnaud et al. 'First results from the NEWS-G direct dark matter search experiment at the LSM'. In: *Astroparticle Physics* 97 (2018), pp. 54–62. ISSN: 0927-6505. DOI: https://doi.org/10.1016/j.astropartphys.2017.10.009. URL: https://www.sciencedirect.com/science/article/pii/S0927650517301871.

[32] A Aguilar-Arevalo et al. 'Results on Low-Mass Weakly Interacting Massive Particles from an 11 kg d Target Exposure of DAMIC at SNOLAB'. In: *Phys. Rev. Lett.* 125 (24 Dec. 2020), p. 241803. DOI: 10.1103/PhysRevLett.125.241803. URL: https://link.aps.org/doi/10.1103/PhysRevLett.125.241803.

[33] C Amole et al. 'Dark matter search results from the complete exposure of the PICO-60 C_3F_8 bubble chamber'. In: *Phys. Rev. D* 100 (2 July 2019), p. 022001. DOI: 10.1103/PhysRevD.100.022001. URL: https://link.aps.org/doi/10.1103/PhysRevD.100.022001.

[34] E Aprile et al. 'Constraining the Spin-Dependent WIMP-Nucleon Cross Sections with XENON1T'. In: *Phys. Rev. Lett.* 122 (14 Apr. 2019), p. 141301. DOI: 10.1103/PhysRevLett.122.141301. URL: https://link.aps.org/doi/10.1103/PhysRevLett.122.141301.

[35] DS Akerib and ohters. 'Limits on Spin-Dependent WIMP-Nucleon Cross Section Obtained from the Complete LUX Exposure'. In: *Phys. Rev. Lett.* 118 (25 June 2017), p. 251302. DOI: 10.1103/PhysRevLett.118.251302. URL: https://link.aps.org/doi/10.1103/PhysRevLett.118.251302.

[36] J Xia et al. 'PandaX-II constraints on spin-dependent WIMP-nucleon effective interactions'. In: *Physics Letters B* 792 (2019), pp. 193–198. ISSN: 0370-2693. DOI: https://doi.org/10.1016/j.physletb.2019.02.043. URL: https://www.sciencedirect.com/science/article/pii/S0370269319301492.

[37] C Patrignani et al. 'Review of Particle Physics'. In: *Chin. Phys.* C40.10 (2016), p. 100001. DOI: 10.1088/1674-1137/40/10/100001.

[38] J Aalbers et al. 'DARWIN: towards the ultimate dark matter detector'. In: *Journal of Cosmology and Astroparticle Physics* 2016.11 (Nov. 2016), pp. 017–017. DOI: 10.1088/1475-7516/2016/11/017. URL: https://doi.org/10.1088/1475-7516/2016/11/017.

[39] M Ibe et al. 'Migdal effect in dark matter direct detection experiments'. In: *Journal of High Energy Physics* 2018.3 (2018), p. 194. ISSN: 1029-8479. DOI: 10.1007/JHEP03(2018)194. URL: https://doi.org/10.1007/JHEP03(2018)194.

[40] KD Nakamura et al. 'Detection capability of the Migdal effect for argon and xenon nuclei with position-sensitive gaseous detectors'. In: *Progress of Theoretical and Experimental Physics* 2021.1 (Nov. 2020). 013C01. ISSN: 2050-3911. DOI: 10.1093/ptep/ptaa162. eprint: https://academic.oup.com/ptep/article-pdf/2021/1/013C01/36123316/ptaa162.pdf. URL: https://doi.org/10.1093/ptep/ptaa162.

[41] E Armengaud et al. 'Searching for low-mass dark matter particles with a massive Ge bolometer operated above ground'. In: *Phys. Rev. D* 99 (8 Apr. 2019), p. 082003. DOI: 10.1103/PhysRevD.99.082003. URL: https://link.aps.org/doi/10.1103/PhysRevD.99.082003.

[42] AK Drukier, K Freese and DN Spergel. 'Detecting cold dark-matter candidates'. In: *Phys. Rev. D* 33 (12 June 1986), pp. 3495–3508. DOI: 10.1103/PhysRevD.33.3495. URL: https://link.aps.org/doi/10.1103/PhysRevD.33.3495.

[43] R Bernabei et al. 'The DAMA project: Achievements, implications and perspectives'. In: *Progress in Particle and Nuclear Physics* 114 (2020), p. 103810. ISSN: 0146-6410. DOI: https://doi.org/10.1016/j.ppnp.2020.103810. URL: https://www.sciencedirect.com/science/article/pii/S0146641020300570.

[44] G Adhikari et al. *Strong constraints from COSINE-100 on the DAMA dark matter results using the same sodium iodide target*. 2021. arXiv: 2104.03537 [hep-ex].

[45] A Zhitnitsky. 'DAMA/LIBRA annual modulation and axion quark nugget dark matter model'. In: *Phys. Rev. D* 101 (8 Apr. 2020), p. 083020. DOI: 10.1103/PhysRevD.101.083020. URL: https://link.aps.org/doi/10.1103/PhysRevD.101.083020.

[46] J Morales et al. 'The Canfranc Underground Laboratory. Present and Future'. In: 17 (Jan. 2004). DOI: 10.1142/9789812701848_0067.

[47] D Hooper and L Goodenough. 'Dark matter annihilation in the Galactic Center as seen by the Fermi Gamma Ray Space Telescope'. In: *Physics Letters B* 697.5 (2011), pp. 412–428. ISSN: 0370-2693. DOI: https://doi.org/10.1016/j.physletb.2011.02.029. URL: https://www.sciencedirect.com/science/article/pii/S0370269311001742.

[48] KN Abazajian and M Kaplinghat. 'Detection of a gamma-ray source in the Galactic Center consistent with extended emission from dark matter annihilation and concentrated astrophysical emission'. In: *Phys. Rev. D* 86 (8 Oct. 2012), p. 083511. DOI: 10.1103/PhysRevD.86.083511. URL: https://link.aps.org/doi/10.1103/PhysRevD.86.083511.

[49] T Damour and LM Krauss. 'A New Solar System Dark Matter Population of Weakly Interacting Massive Particles'. In: *Phys. Rev. Lett.* 81 (26 Dec. 1998), pp. 5726–5729. DOI: 10.1103/PhysRevLett.81.5726. URL: https://link.aps.org/doi/10.1103/PhysRevLett.81.5726.

[50] SL Adler. 'Planet-bound dark matter and the internal heat of Uranus, Neptune, and hot-Jupiter exoplanets'. In: *Physics Letters B* 671.2 (2009), pp. 203–206. ISSN: 0370-2693. DOI: https://doi.org/10.1016/j.physletb.2008.12.023. URL: https://www.sciencedirect.com/science/article/pii/S0370269308015025.

[51] J Casanellas and I Lopes. 'First asteroseismic limits on the nature of dark matter'. In: *The Astrophysical Journal* 765.1 (Feb. 2013), p. L21. DOI: 10.1088/2041-8205/765/1/l21. URL: https://doi.org/10.1088/2041-8205/765/1/l21.

[52] GD Mack, JF Beacom and G Bertone. 'Towards closing the window on strongly interacting dark matter: Far-reaching constraints from Earth's heat flow'. In: *Phys. Rev. D* 76 (4 Aug. 2007), p. 043523. DOI: 10.1103/PhysRevD.76.043523. URL: https://link.aps.org/doi/10.1103/PhysRevD.76.043523.

[53] S Adrián-Martínez et al. 'Limits on dark matter annihilation in the sun using the ANTARES neutrino telescope'. In: *Physics Letters B* 759 (2016), pp. 69–74. ISSN: 0370-2693. DOI: https://doi.org/10.1016/j.physletb.2016.05.019. URL: https://www.sciencedirect.com/science/article/pii/S0370269316301666.

[54] M Aartsen et al. 'Improved limits on dark matter annihilation in the Sun with the 79-string IceCube detector and implications for supersymmetry'. In: *Journal of Cosmology and Astroparticle Physics* 2016.04 (Apr. 2016), pp. 022–022. DOI: 10.1088/1475-7516/2016/04/022. URL: https://doi.org/10.1088/1475-7516/2016/04/022.

[55] M Aguilar et al. 'First Result from the Alpha Magnetic Spectrometer on the International Space Station: Precision Measurement of the Positron Fraction in Primary Cosmic Rays of 0.5–350 GeV'. In: *Phys. Rev. Lett.* 110 (14 Apr. 2013), p. 141102. DOI: 10.1103/PhysRevLett.110.141102. URL: https://link.aps.org/doi/10.1103/PhysRevLett.110.141102.

[56] N Trevisani. 'Collider Searches for Dark Matter (ATLAS + CMS)'. In: *Universe* 4.11 (2018). ISSN: 2218-1997. DOI: 10.3390/universe4110131. URL: https://www.mdpi.com/2218-1997/4/11/131.

[57] E Tolley. 'Dark Matter searches with the ATLAS Detector'. In: *Proceedings of The 39th International Conference on High Energy Physics — PoS(ICHEP2018)*. Vol. 340. 2019, p. 171. DOI: 10.22323/1.340.0171.

[58] WC Kalderon. 'Dark Matter searches with the ATLAS Detector'. In: *PoS* DIS2018 (2018), p. 085. DOI: 10.22323/1.316.0085.

[59] D Vannerom. 'Dark Matter searches with CMS'. In: *PoS* DIS2019 (2019), p. 111. DOI: 10.22323/1.352.0111.

[60] G Gomez-Ceballos. 'Dark Matter Searches with the CMS Experiment'. In: *PoS* EDSU2018 (2018), p. 014. DOI: 10.22323/1.335.0014.

[61] M Battaglieri et al. *US Cosmic Visions: New Ideas in Dark Matter 2017: Community Report*. 2017. eprint: arXiv:1707.04591.

[62] HAMAMATSU PHOTONICS K.K. *Photomultiplier products Datasheet*. 2021. URL: https://www.hamamatsu.com/resources/pdf/etd/High_energy_PMT_TPMZ0003E.pdf (visited on 21/08/2021).

[63] E Aprile et al. 'Energy resolution and linearity of XENON1T in the MeV energy range'. In: *Eur. Phys. J. C* 80.8 (2020), p. 785. DOI: 10.1140/epjc/s10052-020-8284-0. arXiv: 2003.03825 [physics.ins-det].

[64] CE Dahl. 'The physics of background discrimination in liquid xenon, and first results from Xenon10 in the hunt for WIMP dark matter'. PhD thesis. Princeton U., 2009.

[65] Z Liu et al. 'The 4.438MeV gamma to neutron ratio for the Am–Be neutron source'. In: *Applied Radiation and Isotopes* 65.12 (2007), pp. 1318–1321. ISSN: 0969-8043. DOI: https://doi.org/10.1016/j.apradiso.2007.04.007. URL: https://www.sciencedirect.com/science/article/pii/S0969804307001200.

[66] E Aprile et al. 'First Dark Matter Search Results from the XENON1T Experiment'. In: *Phys. Rev. Lett.* 119 (18 Oct. 2017), p. 181301. DOI: 10.1103/PhysRevLett.119.181301. URL: https://link.aps.org/doi/10.1103/PhysRevLett.119.181301.

[67] CAEN S.p.A. *Digital Pulse Processing with Dynamic Acquisition Window*. 2021. URL: https://www.caen.it/products/dpp-daw/ (visited on 21/08/2021).

[68] *AxFoundation/redax*. 2021. URL: https://github.com/AxFoundation/redax (visited on 11/01/2022).

[69] *AxFoundation/strax*. 2021. URL: https://github.com/AxFoundation/strax (visited on 11/01/2022).

[70] *XENONnT/straxen*. 2021. URL: https://github.com/XENONnT/straxen (visited on 11/01/2022).

[71] K SHIBATA et al. 'JENDL-4.0: A New Library for Nuclear Science and Engineering'. In: *Journal of Nuclear Science and Technology* 48.1 (2011), pp. 1–30. DOI: 10.1080/18811248.2011.9711675. eprint: https://doi.org/10.1080/18811248.2011.9711675. URL: https://doi.org/10.1080/18811248.2011.9711675.

[72] HAMAMATSU PHOTONICS K.K. *Photomultiplier R5912 Datasheet*. 2021. URL: https://www.hamamatsu.com/jp/en/product/type/R5912/index.html (visited on 21/08/2021).

[73] CAEN S.p.A. *730 Digitizer Family*. 2021. URL: https://www.caen.it/subfamilies/730-digitizer-family (visited on 21/08/2021).

[74] G Horton-Smith. *GLG4sim page*. 2021. URL: http://neutrino.phys.ksu.edu/~GLG4sim/ (visited on 17/08/2021).

[75] D Motta and S Schönert. 'Optical properties of bialkali photocathodes'. In: *Nuclear Instruments and Methods in Physics Research Section A: Accelerators, Spectrometers, Detectors and Associated Equipment* 539.1 (2005), pp. 217–235. ISSN: 0168-9002. DOI: https://doi.org/10.1016/j.nima.2004.10.009. URL: https://www.sciencedirect.com/science/article/pii/S0168900204022132.

[76] R Ueno. 'Evaluation of response of XENONnT neutron Veto detector'. MA thesis. Kobe University, Feb. 2021.

[77] SF Mughabghab Ph.D. MSc BSc. *Atlas of Neutron Resonances: Resonance Parameters and Thermal Cross Sections. Z=1-100*. English. Hardcover. Elsevier Science, Apr. 2006, p. 1372. ISBN: 978-0444520357. URL: https://lead.to/amazon/jp/?op=bt&la=en&key=044452035X.

[78] *Database of Prompt Gamma Rays from Slow Neutron Capture for Elemental Analysis*. Non-serial Publications. Vienna: INTERNATIONAL ATOMIC ENERGY AGENCY, 2007. ISBN: 92-0-101306-X. URL: https://www.iaea.org/publications/7030/database-of-prompt-gamma-rays-from-slow-neutron-capture-for-elemental-analysis.

[79] Geant4 Collaboration. 'Geant4—a simulation toolkit'. In: *Nuclear Instruments and Methods in Physics Research Section A: Accelerators, Spectrometers, Detectors and Associated Equipment* 506.3 (2003), pp. 250–303. ISSN: 0168-9002. DOI: https://doi.org/10.1016/S0168-9002(03)01368-8. URL: http://www.sciencedirect.com/science/article/pii/S0168900203013688.

[80] Geant4 Collaboration. 'Geant4 developments and applications'. In: 53.1 (2006), pp. 270–278. DOI: 10.1109/TNS.2006.869826.

[81] Geant4 Collaboration. 'Recent developments in Geant4'. In: *Nuclear Instruments and Methods in Physics Research Section A: Accelerators, Spectrometers, Detectors and Associated Equipment* 835 (2016), pp. 186–225. ISSN: 0168-9002. DOI: https://doi.org/10.1016/j.nima.2016.06.125. URL: http://www.sciencedirect.com/science/article/pii/S0168900216306957.

[82] K Hagiwara et al. 'Gamma-ray spectrum from thermal neutron capture on gadolinium-157'. In: *Progress of Theoretical and Experimental Physics* 2019.2 (Feb. 2019). 023D01. ISSN: 2050-3911. DOI: 10.1093/ptep/ptz002. eprint: https://academic.oup.com/ptep/article-pdf/2019/2/023D01/

27970473/ptz002.pdf. URL: https://doi.org/10.1093/ptep/ptz002.

[83] T Tanaka et al. 'Gamma-ray spectra from thermal neutron capture on gadolinium-155 and natural gadolinium'. In: *Progress of Theoretical and Experimental Physics* 2020.4 (Apr. 2020). 043D02. ISSN: 2050-3911. DOI: 10.1093/ptep/ptaa015. eprint: https://academic.oup.com/ptep/article-pdf/2020/4/043D02/33040537/ptaa015.pdf. URL: https://doi.org/10.1093/ptep/ptaa015.

[84] Super Kamiokande Collaboration. Private communication.

[85] B Lenardo et al. 'A Global Analysis of Light and Charge Yields in Liquid Xenon'. In: *IEEE Transactions on Nuclear Science* 62.6 (2015), pp. 3387–3396. DOI: 10.1109/TNS.2015.2481322.

[86] E Aprile et al. 'XENON1T dark matter data analysis: Signal and background models and statistical inference'. In: *Phys. Rev. D* 99 (11 June 2019), p. 112009. DOI: 10.1103/PhysRevD.99.112009. URL: https://link.aps.org/doi/10.1103/PhysRevD.99.112009.

[87] K Lung et al. 'Characterization of the Hamamatsu R11410-10 3-Inch Photomultiplier Tube for Liquid Xenon Dark Matter Direct Detection Experiments'. In: *Nucl. Instrum. Meth.* A696 (2012), pp. 32–39. DOI: 10.1016/j.nima.2012.08.052. arXiv: 1202.2628 [physics.ins-det].

[88] CH Faham et al. 'Measurements of wavelength-dependent double photoelectron emission from single photons in VUV-sensitive photomultiplier tubes'. In: *JINST* 10.09 (2015), P09010. DOI: 10.1088/1748-0221/10/09/P09010,10.1088/1748-0221/2015/9/P09010. arXiv: 1506.08748 [physics.ins-det].

[89] B López Paredes et al. 'Response of photomultiplier tubes to xenon scintillation light'. In: *Astropart. Phys.* 102 (2018), pp. 56–66. DOI: 10.1016/j.astropartphys.2018.04.006. arXiv: 1801.01597 [physics.ins-det].

[90] *XENONnT/epix*. 2021. URL: https://github.com/XENONnT/epix (visited on 11/01/2022).

[91] *XENONnT/wfsim*. 2021. URL: (https://github.com/XENONnT/WFSim (visited on 11/01/2022).

[92] E Aprile et al. 'Material radioassay and selection for the XENON1T dark matter experiment'. In: *Eur. Phys. J.* C77.12 (2017), p. 890. DOI: 10.1140/epjc/s10052-017-5329-0. arXiv: 1705.01828 [physics.ins-det].

[93] E Aprile et al. 'Observation of two-neutrino double electron capture in 124Xe with XENON1T'. In: *Nature* 568.7753 (2019), pp. 532–535. ISSN: 1476-4687. DOI: 10.1038/s41586-019-1124-4. URL: https://doi.org/10.1038/s41586-019-1124-4.

[94] A Lyashenko et al. 'Measurement of the absolute Quantum Efficiency of Hamamatsu model R11410-10 photomultiplier tubes at low temperatures down to liquid xenon boiling point'. In: *JINST* 9.11 (Nov. 2014), P11021–P11021. ISSN: 1748-0221. DOI: 10.1088/1748-0221/9/11/p11021. URL: http://dx.doi.org/10.1088/1748-0221/9/11/P11021.

[95] E Aprile, J Aalbers, F Agostini, M Alfonsi, L Althueser, FD Amaro, VC Antochi, F Arneodo et al. 'XENON1T dark matter data analysis: Signal reconstruction, calibration, and event selection'. In: *Phys. Rev. D* 100 (5 Sept. 2019), p. 052014. DOI: 10.1103/PhysRevD.100.052014. URL: https://link.aps.org/doi/10.1103/PhysRevD.100.052014.

[96] K Mizukoshi et al. 'Measurement of ambient neutrons in an underground laboratory at the Kamioka Observatory'. In: *Progress of Theoretical and Experimental Physics* 2018.12 (Dec. 2018). 123C01. ISSN: 2050-3911. DOI: 10.1093/ptep/pty133. eprint: https://academic.oup.com/ptep/article-pdf/2018/12/123C01/27323103/pty133.pdf. URL: https://doi.org/10.1093/ptep/pty133.

[97] S Westerdale and P Meyers. 'Radiogenic neutron yield calculations for low-background experiments'. In: *Nuclear Instruments and Methods in Physics Research Section A: Accelerators, Spectrometers, Detectors and Associated Equipment* 875 (2017), pp. 57–64. ISSN: 0168-9002. DOI: https://doi.org/10.1016/j.nima.2017.09.007. URL: https://www.sciencedirect.com/science/article/pii/S0168900217309622.

[98] AJ Koning, S Hilaire and M Duijvestijn. 'TALYS: Comprehensive Nuclear Reaction Modeling'. In: 2005.

[99] B Aharmim et al. 'Combined analysis of all three phases of solar neutrino data from the Sudbury Neutrino Observatory'. In: *Phys. Rev. C* 88 (2 Aug. 2013), p. 025501. DOI: 10.1103/PhysRevC.88.025501. URL: https://link.aps.org/doi/10.1103/PhysRevC.88.025501.

[100] M Honda et al. 'Improvement of low energy atmospheric neutrino flux calculation using the JAM nuclear interaction model'. In: *Phys. Rev. D* 83 (12 June 2011), p. 123001. DOI: 10.1103/PhysRevD.83.123001. URL: https://link.aps.org/doi/10.1103/PhysRevD.83.123001.

[101] E Aprile, J Aalbers, F Agostini, M Alfonsi, L Althueser, F Amaro et al. 'Projected WIMP sensitivity of the XENONnT dark matter experiment'. In: *Journal of Cosmology and Astroparticle Physics* 2020.11 (Nov. 2020), pp. 031–031. DOI: 10.1088/1475-7516/2020/11/031. URL: https://doi.org/10.1088/1475-7516/2020/11/031.

[102] E Aprile et al. 'Search for Light Dark Matter Interactions Enhanced by the Migdal Effect or Bremsstrahlung in XENON1T'. In: *Phys. Rev. Lett.* 123 (24 Dec. 2019), p. 241803. DOI: 10.1103/PhysRevLett.123.241803. URL: https://link.aps.org/doi/10.1103/PhysRevLett.123.241803.

Acknowledgements

First of all, I gratefully acknowledge my supervisor Prof. Kentaro Miuchi for everything, not only my research works but also my exciting life at Kobe University. I am grateful to XENON collaborators in particular the simulation team, neutron veto subgroup, and Japan group. I wish to thank members of the Kobe particle physics group, Prof. Hisaya Kurashige, Prof. Yasuo Takeuchi, Prof. Yuji Yamazaki, Prof. Ochi Atsuhiko, Prof. Atsumu Suzuki, Prof. Junpei Maeda, Prof. Yuuki Nakano, Dr. Satoshi Higashino, and Ms. Kazumi Yoshida. I thank Dr. Takashi Iida, Prof. Ken'ichi Fushimi, Prof. Masao Yoshino, Prof. Tomo Miyazaki, Prof. Kiseki D Nakamura, Prof. Takaomi Yano, Prof. Sei Yoshida, Prof. Tadafumi Kishimoto, and YMAP members for fruitful discussions. Dr. Keishi Hosokawa found Figure 2.5 for me.

This work was supported by KAKENHI Grants-in-Aid (19J20418). I acknowledge DeepL GmbH for their translation application. DeepL is capable of translating natural Japanese into English in real-time, and its translation accuracy is higher than that of competitors such as Google Translate. It is also possible to select a natural word from among the candidates. I hope to see a future in which all papers are written in their native languages. In addition, DeepL helps me in not only writing this thesis but also stay in the experimental site in Italy. Without DeepL, this research could not exist. My greatest thanks to DeepL. Translated with www.DeepL.com/Translator (free version)

Finally, I would thank Ms. Hinako Tanaka for being with me.

APPENDIX A

Mini bucket measurement for ePTFE reflectivity

The ePTFE reflectivity of the nVeto had not been measured in water. In order to verify the principle of the reflectivity monitor and to accurately measure the reflectivity of ePTFE in water, a measurement using a mini bucket was carried out at Kobe University [76]. The measurement principle is the same as the nVeto ePTFE reflectivity monitor. The timings from the laser injection to photon detections are measured. The measurements were carried out with the laser used in the reflectivity monitor, a PMT (Hamamatsu K.K., R8778), and a mini bucket (height 30 cm, diameter 30 cm) filled with pure water and lined with the ePTFE. Compared to the nVeto detector, the setup is smaller thus a more number of photon reflections are expected in the mini bucket. In addition, the configuration reduces the objects whose optical properties are unknown as much as possible. Figures A.1 show the pictures of the setup.

A simulation tool based on the Geant4 is constructed for the optical simulation. Figure A.2 shows the constructed geometry of the tool. The observed photon timings from the laser injection have obtained by the simulation. Figure A.3 shows the timing distributions evaluated for the several ePTFE reflectivities. The small setup is more sensitive for the ePTFE reflectivity than the nVeto detector.

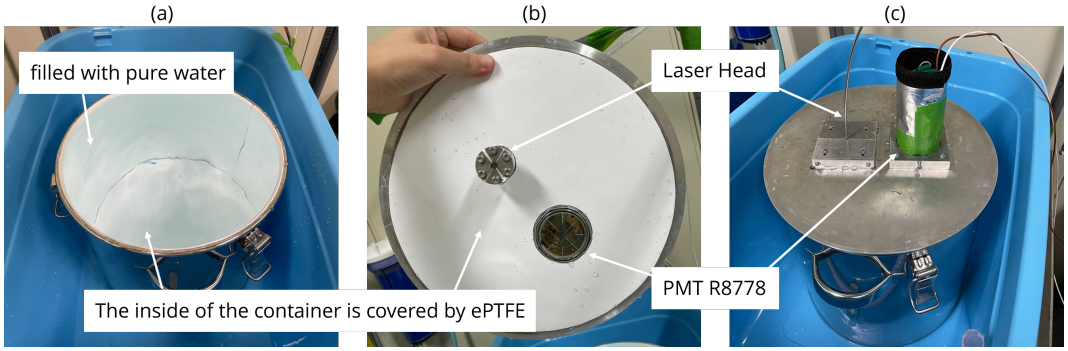

FIGURE A.1. Setup of the mini bucket measurement. (A) The bucket is lined with the ePTFE and filled with pure water. (B) The laser head and the PMT are installed. (C) The mini bucket is closed for the measurement [76].

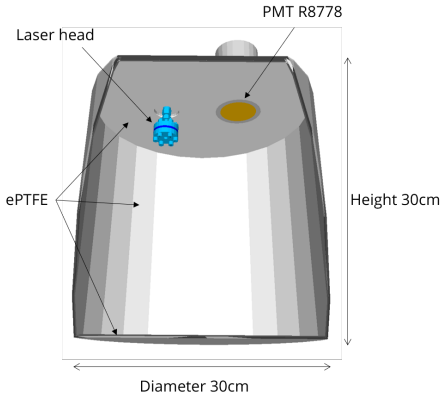

FIGURE A.2. The constructed geometry for the mini bucket measurement [76].

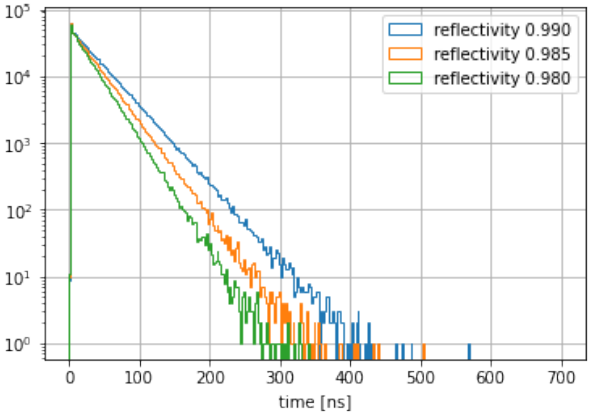

FIGURE A.3. The simulated timing distribution from the laser injection with different ePTFE reflectivities [76].

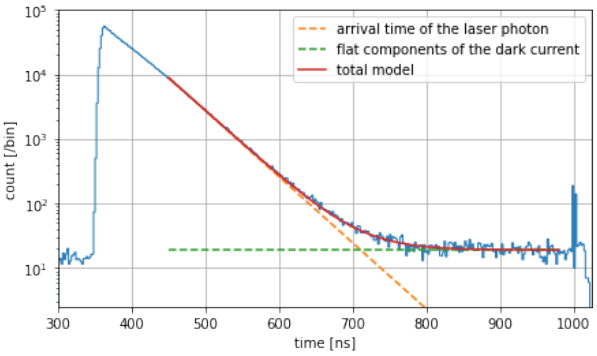

FIGURE A.4. Observed timing distribution in the mini bucket measurement. The time slope is fitted with an exponential function and a flat component [76].

The obtained distribution is shown in Figure A.4. The observed time distribution is fitted with an exponential function and a flat component.

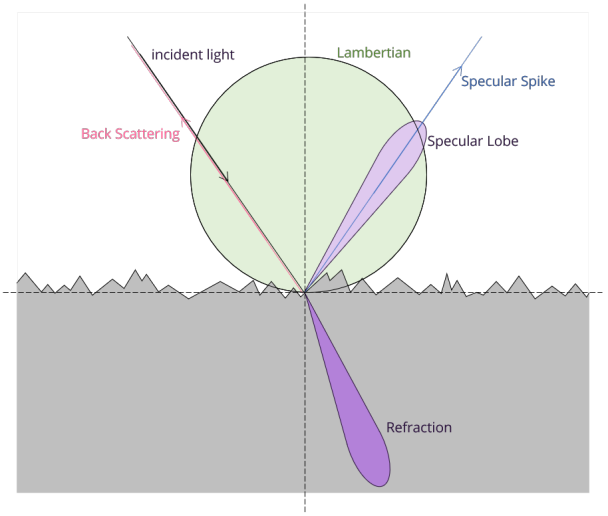

FIGURE A.5. Conceptional image of the Geant4 unified model for the optical photon [76].

The reflection models of the Geant4 are uncertainties of the measurement. The obtained time constant is 43.5 ± 0.1 ns.

The optical reflection has been implemented in Geant4 as 'Unified model' which includes a variety of models. Figure A.5 shows the models included in the 'Unified model'. The Lambertian model diffuses the photon independently to the angle of the incident photon. The specular spike model implements specular reflection depending on the incident angle. The specular lobe model is a Specular Spike model with smearing. The back scattering model returns the photon to the incident angle. The 'Unified model' is composed of these models. The ePTFE is a porous material thus the Lambertian model is suggested, however, this measurement doesn't have sensitivity for these models. In this measurement, we assumed all models to evaluate the ePTFE reflectivity. Figure A.6 shows the represented reflectivity for these models. We found that the optical model difference is not large. Considering the model difference as a systematic uncertainty, the evaluated ePTFE reflectivity is $99.346 \pm 0.004\ ^{+0.149}_{-0.156}\%$ (statistical and systematic errors). The obtained ePTFE reflectivity of the nVeto detector is in good agreement with this result.

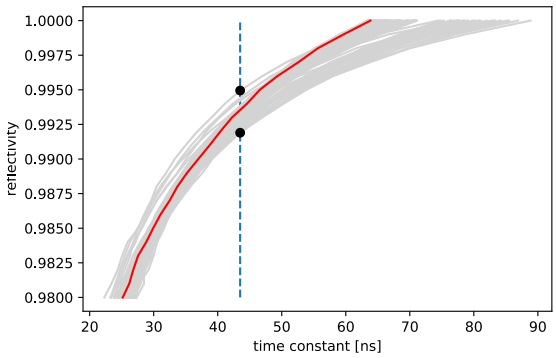

FIGURE A.6. The simulated relationship between the observed time constant and ePTFE reflectivity. The blue dotted line shows the obtained time constant. The red line shows the result assuming 100% Lambertian reflection. The grey lines show the results of the other reflection models which should be considered as a systematic uncertainty.

APPENDIX B

Uranium and Thorium decay chains

Some heavy nuclei decay continuously into unstable nuclei, which are known as decay chains (series). The first heavy nuclei have a relatively long lifetime. After that, they decay into short-lived nuclei by repeated α and β decays. The decay chains called the Uranium chain and Thorium chain, are particularly important in the search for rare events. Starting from ^{238}U, the Uranium chain is the chain of nuclei whose mass number is $4n + 2$. In the uranium chain, ^{222}Rn is gaseous and easily mixed into the detector. Starting from ^{232}Th, Thorium chain is the chain of nuclei whose mass number is $4n$. Called Actinium chain composed with the nuclei whose mass number is $4n + 1$. Figures B.1, B.2, and B.3 show Uranium, Thorium, and Actinium decay chains.

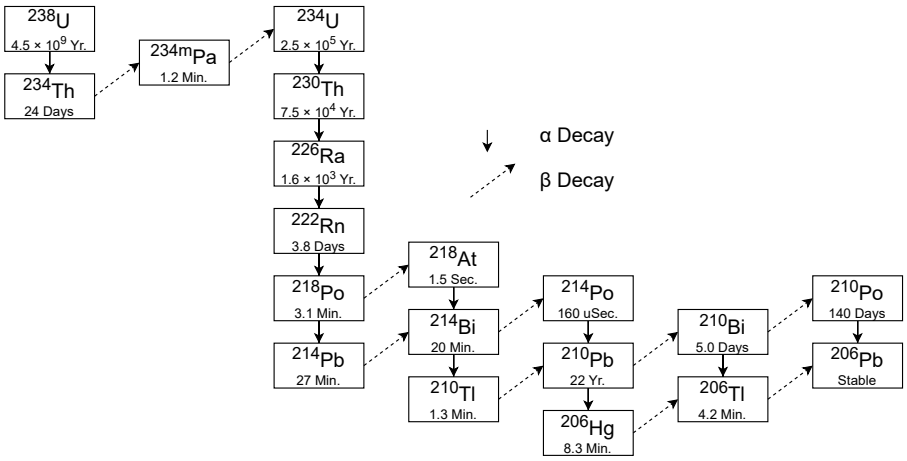

FIGURE B.1. Uranium decay chain.

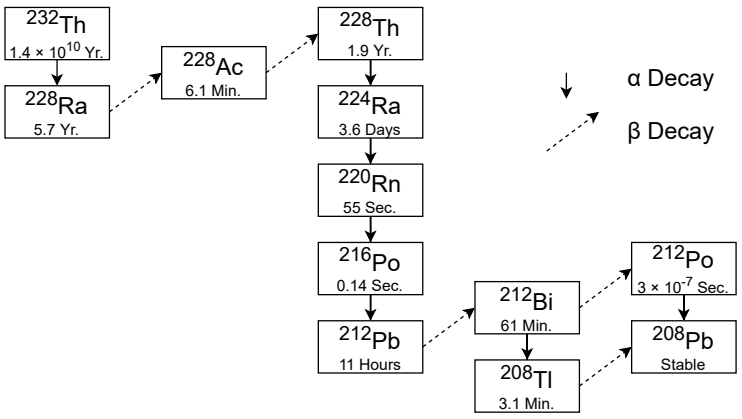

FIGURE B.2. Thorium decay chain.

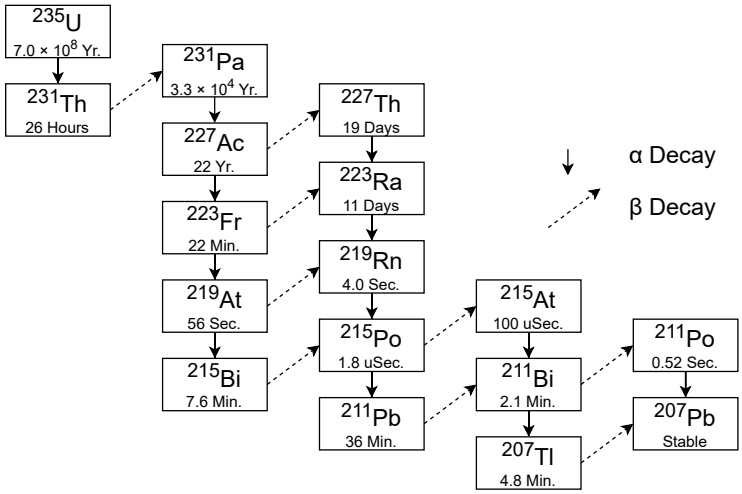

FIGURE B.3. Actinium decay chain.

APPENDIX C

The fitting package on python

In the particle and nuclear physics community, ROOT, developed by CERN, has long been used as a framework for analysis. ROOT is one of a limited number of open-source software that can perform analysis on large data sets (∼PB) such as those obtained in experiments. Users can include ROOT in their C++ source code, or use ROOT's interpreter in a console.

For various reasons, more and more experiment collaborations (e.g., XENONnT, Ice Cube) are using python-based analysis instead of C++. Although the Python analysis environment is fairly well developed, it is still not a complete replacement for ROOT's data store and fitting functions.

The datastore function (called TTree in ROOT) can be replaced to some extent by using the save function of NumPy, the major numerical package of Python. On the other hand, there is no practical package for fitting functions from the following perspectives.

- Easy installation with pip
- Error-aware fitting
- Setting cost function (χ^2 regression, (Un)Binned likelihood, and them with pull-term)
- Visualization, in particular, during setting initial parameters

Only the combination of iminuit and probfit packages satisfies these conditions relatively frequently. Therefore, I add the Binned Fitting interface to the probfit package. By this development, all the conditions are satisfied.

The preparation is shown in the Code C.1.

CODE C.1. Environment preparation

```
1 import numpy as np
2 import matplotlib.pyplot as plt
3 import iminuit, probfit
4
5 # Make dummy data
6 data = np.random.randn(10000) * 4 + 1
7 plt.hist(data, bins=100, range=(-15, 15), histtype='step')
```

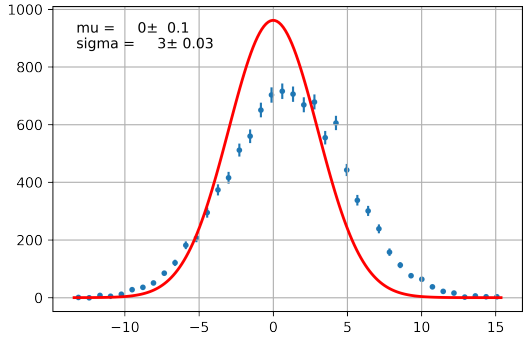

FIGURE C.1. Result of Code A.2. User can repeat to edit initial parameters.

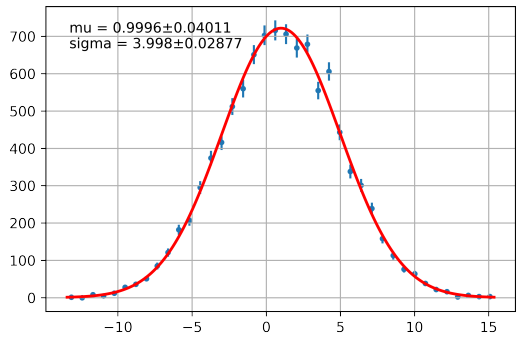

FIGURE C.2. Result of Code A.3.

The fitting packages, iminuit and probfit are installed via pip.

The example usage is shown in the Code C.2.

CODE C.2. Configuring fitting

```
# Define model as a function
def gauss_pdf(x, mu, sigma):
    return 1 / np.sqrt(2 * np.pi) / sigma * np.exp(-(x - mu) ** 2 / 2. / sigma ** 2)

# Define cost function
cost = probfit.BinnedLH(gauss_pdf, data) # Binned likelihood
minuit = iminuit.Minuit(cost, mu=0, sigma=3) # pass initial parameters
cost.draw(minuit)
```

The fitting requires the fitting function, its initial parameters, and cost function. Figure C.1 shows the example of visualizing the data and fitting function with initial parameters. For the fitting, the initial parameters should be approximately similar to avoid the local minimum. It can be tried until better initial parameters are obtained. Then, the fitting is executed with Code C.3

CODE C.3. Fitting and visualization

```
# Fitting
minuit.migrad()

# Visualization
cost.draw(minuit);
```

The fitting parameters are obtained and visualized like Figure C.2.